論文の内容の要旨

論文題目　Optical Mode Cleaner
for the Interferometric Gravitational Wave Detector

「干渉計型重力波検出器のためのモードクリーナーの開発」

氏名　新谷 昌人

一般相対論のひとつの帰結として重力波の存在が予言されているが、未だに直接検出されていない。しかし、重力波の存在自体は Taylor らによる連星中性子星の公転周期の観測から間接的に検証されている。もし直接検出できれば一般相対論を検証できるだけではなく、「重力波天文学」として高密度星で起こる現象を電磁波などの従来の手段では得られない情報を検出できる。例えば、超新星爆発の瞬間のコアの角運動量や連星中性子星の合体の重力波振幅から天体までの距離などを求めることができる。このように重力波検出は物理学的・天文学的観点から興味深いものであるが、物質と重力波の相互作用が非常に小さいためにこれまで検出は困難とされてきた。しかし、最近の測定技術の進歩によって重力波検出が不可能ではないレベルまで研究が進んできており、世界各国でキロメートルクラスの大型干渉計の建設をめざして感度向上への研究が進められている。日本でも平成２年度より重点領域研究の一環としてプロトタイプの検出器の開発を行い大型干渉計への基礎技術の開発を行っている。

干渉計型重力波検出器の原理は、吊るされた２枚の鏡の間の距離を干渉計で高精度に検出し、重力波によって生じる固有距離の変化としてとらえるものである。超新星爆発や連星中性子星の合体などで放出される 100Hz～1kHz 付近のバースト的な重力波に対しては、十分に防振された鏡と安定化されたレーザーを用いて重力波の振幅 h～10^-21 程度の感度を達成すれば年間数イベントの観測ができると考えられている。この程度の感度は原理的には達成可能で、いくらかの技術的な困難を乗り越えれば実現できると思われる。検出感度を決める大きな要因のひとつがレーザー光源に起因するノイズで、特に周波数ノイズに対する要求がきびしい。そこで、本研究ではモードクリーナーと呼ばれる光共振器を基準にレーザーを周波数安定化するシステムを設計し、実際に国立天文台の２０ｍプロトタイプ検出器に組み込み運転をおこなった（図１）。

国立天文台では共振器長２０ｍの Fabry-Perot 干渉計型重力波検出器の開発を行っている。この干渉計の特徴としては将来必須の技術とされるリサイクリングを組み込めるように、信号の読みだしに直接干渉方式を採用していることである。本研究以前の測定でこの干渉計の感度を決めている主なノイズ源はレーザー光の周波数ノイズであることがわかっていた。そこで、レーザーの周波数安定化が必要となるが、これにはいくつかの方法がある。現在採用している直接干渉方式と両立しうる方式として、我々は本体の干渉計とは別の Fabry-Perot 共振器（モードクリーナー）を用意してこれを基準に周波数安定化を行うことにした。この方法ではレーザーのすべての光を無駄なく使って安定化できるのでショットノイズ限界の安定化を達成することができる。また、この方式ではモードクリーナーの透過光を主検出器の光源として使うために、本来のモードクリーナーの特性である、もとのレーザー光の持っている空間的なビームの変形やゆらぎを低減させる効果も期待できる。

また、本研究のもう一つの特徴としては、モードクリーナー共振器の２枚の鏡をそれぞれ独立に吊るしていることが挙げられる。これまで海外の研究を含め、プロトタイプ用のモードクリーナーとしては単一モード光ファイバーやロッド固定式 Fabry-Perot が用いられてきたが、将来の高出力レーザーを用いた長基線長の干渉計にはこのような方式では問題がある。将来のフルスケール干渉計にも応用できる技術開発を考えて、我々は独立懸架のモードクリーナーの開発を行うことにした。

このような目的で、共振器長１ｍのモードクリーナーを使った周波数安定化システ

ムを設計した。共振器として使用した鏡は直径 50mm 長さ 100mm の石英のロッドに鏡をオプティカルコンタクトしたもので、鏡は損失の少ないイオンビームスパッタ法で製作されたものである。将来的にもこの方法が有力視されており、実際の鏡の特性はフィネス 1500 で共振器の透過率が９０％程度に達する高透過率であった。２枚の鏡は独立に二段振り子の防振系で懸架されている。防振系には板バネで作った垂直方向の防振系も組み込まれていて防振効果が高められている。これらの鏡は真空容器中に納められているため、外部から鏡の位置制御を行うためのモータードライブと微調整用のピエゾ素子がとりつけられている。

光源として使用したレーザーは半導体レーザー励起モノリシック Nd:YAG レーザーで、出力が 500mW のものである。このレーザーは波長が 1064nm の赤外であるために扱いがやや面倒であるが、将来の高出力・高安定化の可能性が高いレーザーであるのでこれを採用した。レーザーの発振周波数は共振器にはりつけたアクチュエーターでコントロールできるため周波数安定化にはこれを利用した。レーザーの周波数安定化は吊るした鏡を基準にしているため高周波の周波数揺らぎに対しては良い基準となるが、低周波では共振器の振り子運動のためにむしろ安定度は悪い。そこで、安定化のサーボ系は２系統使い、ひとつは共振器長を低周波で制御して振り子運動を抑えるループ、そしてもうひとつは高周波で共振器を基準にレーザーを安定化するループで高周波の揺らぎのみの安定化を行った。このふたつのループの交差する周波数は振り子運動ともとの周波数ノイズとのかねあいから 30Hz にし、観測帯域である 1kHz 付近で 80dB の安定化利得がとれるようにサーボ系を設計した。

プロトタイプに組み込む前に、モードクリーナー単体での特性（モードクリーニング効果・周波数安定度）をまず評価した。

モードクリーニング効果としては入射光の角度や位置のゆらぎであるビームジッターの除去効果を評価した。理論的計算では使用した共振器に対しては 60dB 程度の除去効果が期待できる。実際にはモードクリーナーのある場合とない場合について 20m 先のビームの位置を検出した。位置検出にはナイフエッジを利用した位置検出器を用いた。モードクリーナーのない場合の入射光ビームジッターは 100Hz 以下ではエアコンによる空気の揺らぎの効果が支配的であったのでその除去効果を測定した。測定した結果、エアコンによるゆらぎの除去効果がはっきりと確認できた。モードクリーナー懸架の共振による低周波のジッターがあることが新たにわかったが、

数百Ｈｚの観測帯域のジッターについては防振がきいているために検出限界以下であった。

次に周波数安定度を評価した。まず、モードクリーナーの周波数安定化サーボの誤差信号から見積もった周波数安定度は、設計通り 1kHz で 80dB の安定度が得られて 1mHz/√Hz 程度が得られた。しかし、実際の周波数安定度は別の共振器を用いて評価する必要があるため２０ｍプロトタイプ検出器で用いる Fabry-Perot 共振器による周波数安定度の評価を行った。２０ｍ共振器の誤差信号から得られた値は1桁悪く 10mHz/√Hz であった。この差を生じさせるノイズ源は２０ｍ共振器付近の外来の振動に応じて変化することがわかったので、安定化光を２０ｍ共振器に導入するときに用いた固定鏡による位相ノイズや光学台の機械共振が主なノイズ源であると推定された。

このように、モードクリーナーの基本的な機能について所期の性能を確認することができた。ノイズについても完全に評価することはできなかったものの設計通りのレベルに近いことがわかったので２０ｍプロトタイプ検出器に実際にモードクリーナーを接続し性能を評価した。まず、干渉計のコントラストの向上がみられ、モードクリーナーを入れる前の９５％から９９％以上に改善された。これにより干渉光をほぼ完全にダーク条件にすることができ、モードクリーナーによりもとのレーザー光に含まれる高次モードが除去されたことが確認された。

これまでは周波数ノイズで感度が制限されていたが、モードクリーナーによる周波数安定化の効果で感度が２桁以上向上し、変位換算で 10^-16m/√Hz、重力波の振幅では h～10^-16 となる（図２）。設計された感度には２桁ほど離れているが、先の固定鏡による位相雑音の他に干渉計の２本の腕による同相雑音除去比があまりとれなかったことが原因の一つである。干渉計のコントラストが向上したにもかかわらず同相雑音除去比がとれないのは両腕の Fabry-Perot のフィネスの差でほぼ説明できるので高性能な鏡を使用して対称性をよくすれば改善される可能性が高い。

現在得られている感度は重力波検出のためには５桁不足しているが、現在のままで固定鏡の防振と高性能鏡を用いて２桁の感度の改善が見込まれる。腕をキロメートルにすればもう２桁、さらにレーザー出力を１００倍すればショットノイズ限界が１桁低下して目標の感度に達成する。実際にはこれほど単純ではないが、少なくとも本研究で採用したモードクリーナーは重力波検出器と組み合わせたシステムとし

て問題なく動作することがわかり、将来の検出器に対しての見通しを得ることができた。

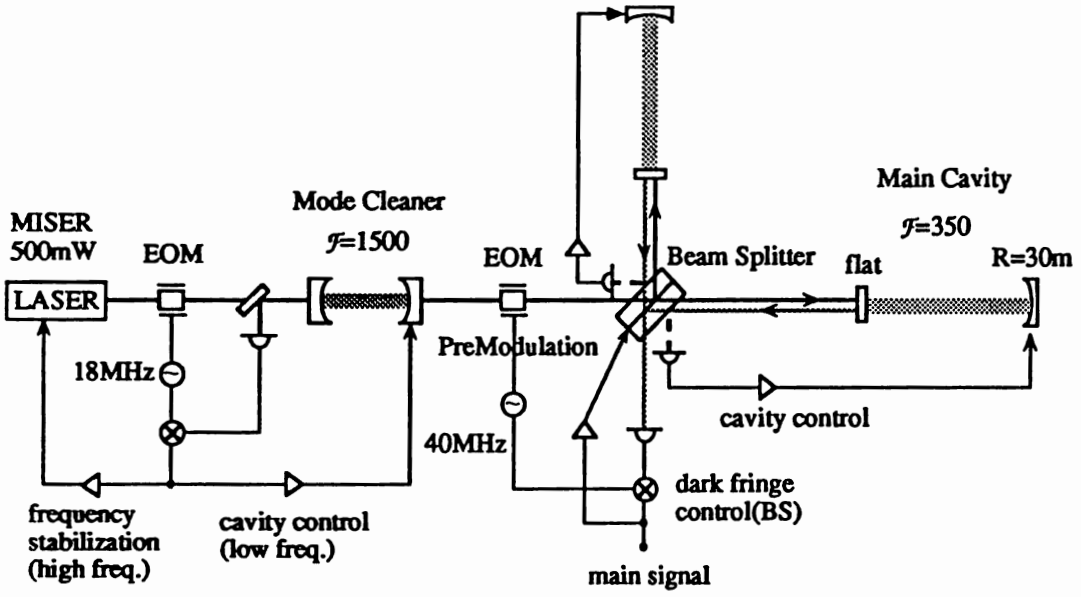

Optical Design of 20m FP Prototype with Mode Cleaner

図１　モードクリーナーと２０ｍプロトタイプの光学系

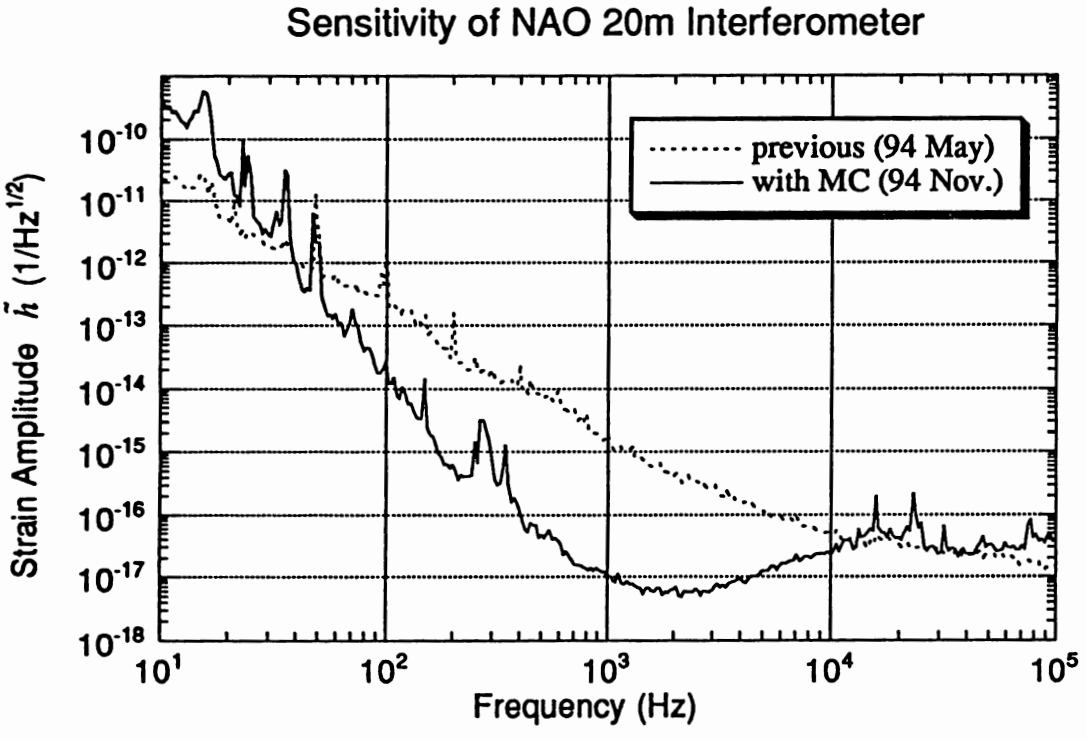

図２　モードクリーナー接続以後の感度の変化

THESIS

Optical Mode Cleaner

for the Interferometric Gravitational Wave Detector

Akito Araya

December 1994

Contents

1. Introduction

§1.1 Detection of Gravitational Waves

As one of the consequences of the general relativity, existence of gravitational waves are deduced, which is similar to the electromagnetic waves from Maxwell equation. Although gravitational waves have never been detected due to very small gravitational constant G, their evidence has been observed from the period of binary neutron stars [1]. Since gravitational waves are radiated from the motion of such massive star, the binary system lose total energy carried away by gravitational waves, resulting in the decrease of revolution period. From the observation of binary pulsar, PSR1913+16, observed periods are in good agreement with the predicted one from general relativity.

Detection of gravitational waves implies two significant meanings; investigation of nature of the waves, and, more importantly, observation of astronomical phenomena with a new channel. The former includes investigation of quadrupole polarization of the waves and confirmation of their propagation speed of c, as well as existence of themselves.

As for the astronomical aspects, detection of gravitational waves brings various information which cannot obtain from other methods, e.g. electromagnetic waves. One possibility is the estimation of angular momentum just before the supernova explosion, and to solve the mechanism of it. Another possibility is to detect gravitational waves from coalescing binary neutron stars. From their waveform and amplitude, parameters of the binary system, verification of general relativity in such highly relativistic field, and distance to the source are estimated [2]. The last one can be utilized to determine such cosmological parameters as Hubble constant. We currently develop the interferometric gravitational wave detector to be constructed on the earth near future, aiming at detection of such burst waves. (Mode Cleaner is one of the components of such detector which reduces the excess noise originating from laser.)

Another type detector for such burst sources is a resonant detector, originated from the experiment by J.Weber [3]. It detects resonant vibration of a lump of, say aluminum, excited by gravitational waves. Several detectors, called second generation detectors, are operating in cryogenic temperature. They are summarized in Table 1.1. As a future plan of resonant detectors, spherical detectors are proposed [4].

Although other sources such as background gravitational wave radiation are also very attractive to physicists and astronomers, frequency of their waves is very low and difficult to detect on the earth (Table 1.2). Detection of such sources is tried by Doppler tracking and pulsar timing observation. Another approach would be realized in the next future by space interferometer [5].

Current status on the interferometric gravitational wave detectors and development of Mode Cleaner are described in the following section.

§1.2 Current Status of Interferometric Detectors and Mode Cleaner

Several groups are currently developing interferometric gravitational wave detector aiming at construction of full scale detector with km cavity length. With such a detector with sensitivity of better than $h \sim 10^{-21}$, several events of super nova explosion or coalescence of binary neutron stars occurred in the Virgo Cluster will be detected in a year. Future plan for full scale detectors are shown in Table 1.3.

Some groups including Japan have prototype detectors to investigate basic performance of the interferometer and noise sources which limits sensitivity. Prototype detectors are summarized in Table 1.4. In Japan, two Fabry-Perot prototypes (20m, 3m) and a 100 Delay-Line prototype detector are in operation. One of them is a 20m Fabry-Perot prototype detector at National Astronomical Observatory. It uniquely applied recombination scheme using pre-modulation (Section

機関	アンテナ	方式	感度
CERN／ローマ	Al5056, 2.3ton, 2.6K	Capacitive + SQUID	$7.\times 10^{-19}$
CERN(NAUTILUS)	Al5056, 2.3ton, 0.1K	Capacitive + SQUID	2×10^{-18}
ルイジアナ州立大	Al5056, 1.1ton, 4.2K	Inductive + SQUID	7×10^{-19}
スタンフォード大	Al6061, 4.8ton, 4.2K	Inductive + SQUID	10^{-18}
西オーストラリア大	Nb, 1.5ton, 5K	RF cavity	9×10^{-19}
宇宙線研／東大	Al5056, 1.7ton, 300K	レーザー TRD	-
KEK	Al5056, 1.2ton, 4.2K	Capacitive + FET	4×10^{-22}(60Hz)

Table 1.1 Current status of resonant-type gravitational wave detector.

重力波源	振動数	振幅 h	頻度	検出法
連星中性子星の合体 (200Mpc)	10~1000Hz	10^{-21}	3/年	レーザー干渉計＋テンプレート
超新星爆発（銀河系内）	~1kHz	10^{-18}	1/数十年	レーザー干渉計、共振型検出器
超新星爆発（乙女座銀河団）	~1kHz	10^{-21}	数イベント/年	kmレーザー干渉計
巨大ブラックホールの形成	~1mHz	10^{-17}	1/年	レーザー干渉計（宇宙空間）
パルサー	数 10Hz	10^{-25}	連続波	レーザー干渉計、共振型検出器
宇宙ひも	10^{-7}Hz	10^{-15}	背景波	パルサータイミング

Table 1.2 Sources of gravitational waves.

7.1) because recombination is considered to be inevitable for the recycling scheme. Fortunately we succeeded in operation of recombined 20m prototype in 1994 [6], and found that the frequency noise of the laser limited its sensitivity.

Mode cleaner is incorporated into most prototypes between laser and main interferometer for the purpose of reduction of beam jitter and spurious higher mode. Some groups adopt single mode optical fiber which introduces laser beam into the vacuum chamber as well as work as mode cleaner. Another type is a rigid cavity whose mirrors are attached to the rod forming Fabry-Perot cavity. This cavity can also be utilized as a reference for frequency stabilization. However considering future high power laser with long cavity length, they will be replaced with suspended mode cleaner whose mirrors are independently suspended as pendulums.

In this point of view, we have developed Mode Cleaner of independently suspended Fabry-Perot cavity which works as both mode cleaner and reference of frequency stabilization, and firstly succeeded in operation of prototype with such Mode Cleaner.

§1.3 Contents

In this thesis, we report on the development of Mode Cleaner to be connected to prototype detector as a light source. Mode Cleaner we designed was inserted between prototype detector and laser in order to reform the original beam geometry (deformation of laser beam or beam fluctuation). Another function of our Mode Cleaner is to stabilize laser in frequency. As for the function of reformation of beam geometry, it is not so serious noise source for the current prototype detector but will be one of noise sources for future large scale detector. On the other hand, frequency noise is significant noise source of current prototype. In order to attain possible sensitivity limited by shot noise, frequency stabilization should be applied.

One characteristics of our system is to apply the Fabry-Perot cavity as Mode Cleaner, whose mirrors are suspended independently. Another one is to stabilize

国	計画名	基線長	方式	観測開始予定時期
米国（カルテク&ＭＩＴ）	LIGO	4km(2台)	FP	1998年
伊・仏	VIRGO	3km	FP	1998年
豪	AIGO	3km	FP	?
独・英	GEO	600m	Dual Recycling	数年以内
日本	TAMA	300m	FP	1998年

Table 1.3 Project for large-scale gravitational wave detector.

機関	基線長	方式	感度
カルテク	40m	Locked FP	10^{-18}
グラスゴー大	10m	Locked FP	10^{-18}
国立天文台	20m	Recombined FP	10^{-15}
東大	3m	Recombined FP	10^{-15}
マックスプランク研究所	30m	DL	10^{-18}
宇宙科学研究所	100m	DL	10^{-16}

Table 1.4 Current status of prototype detectors.

laser frequency referred to the Fabry-Perot using reflected light from the cavity. In this way, ultimate frequency stabilization limited by shot noise of full laser power can be realized because of dark locking of reflected light. We designed such Mode Cleaner with 1-meter cavity length suspended in the vacuum chamber. Laser diode pumped Nd:YAG laser was utilized as light source.

In Chapter 2, gravitational waves as a consequence of general relativity is described, including generation and effect of gravitational waves. Principles and noise sources of interferometric gravitational wave detectors are shown in Chapter 3. Following Chapter 4 and 5 describe the design of Mode Cleaner with 1-meter Fabry-Perot cavity. After measuring performance of our Mode Cleaner in Chapter 6, 20m Fabry-Perot prototype detector was operated with Mode Cleaner resulting in improved contrast and sensitivity compared with previous experiment without Mode Cleaner (Chapter 7). As conclusions, summary and problem of this experiment are discussed for the future large scale detector.

2. Gravitational Waves

§2.1 Gravitational Waves

According to the theory of general relativity, metric tensor of spacetime, $g_{\mu\nu}$, satisfies following Einstein's field equation:

$$R_{\mu\nu} - \frac{1}{2}g_{\mu\nu}R = \frac{8\pi G}{c^4}T_{\mu\nu}, \tag{2.1}$$

where G, c, and $T_{\mu\nu}$ are the gravitational constant, the speed of light, and the energy-momentum tensor, respectively. While, $R_{\mu\nu}$ (Ricci tensor) and R (scalar curvature) are deduced from $g_{\mu\nu}$ using following relations:

$$R = g_{\mu\nu}R_{\mu\nu} \tag{2.2}$$

$$R_{\mu\nu} = R^{\alpha}{}_{\mu\alpha\nu} \tag{2.3}$$

$$R^{\alpha}{}_{\beta\mu\nu} = \Gamma^{\alpha}{}_{\beta\nu,\mu} - \Gamma^{\alpha}{}_{\beta\mu,\nu} + \Gamma^{\alpha}{}_{\sigma\mu}\Gamma^{\sigma}{}_{\beta\nu} - \Gamma^{\alpha}{}_{\sigma\nu}\Gamma^{\sigma}{}_{\beta\mu} \quad \text{(Riemann tensor)}$$

$$\Gamma^{\gamma}{}_{\beta\mu} = \frac{1}{2}g^{\alpha\gamma}(g_{\alpha\beta,\mu} + g_{\alpha\mu,\beta} - g_{\beta\mu,\alpha}) \quad \text{(Chritoffel symbol).}$$

The right side of the Einstein equation describes mass or energy, and they define the structure of the field (left side of the equation). Moreover, as the defined field has gravitational energy, it also defines the field again, and repeatedly. Nonlinearity of Einstein equation comes from this situation.

Although it's very difficult to solve the equation analytically, one can investigate the nature of the field by linearizing the equation. If we think of nearly flat spacetime, namely metric deviates only small amount $h_{\mu\nu} \ll 1$ from flat metric $\eta_{\mu\nu}$, Einstein field equation can be linearized using proper gauge transformation.

$$\Box\phi_{\mu\nu} = -\frac{16\pi G}{c^4}T_{\mu\nu}, \tag{2.4}$$

where

$$g_{\mu\nu} = \eta_{\mu\nu} + h_{\mu\nu}$$

$$\phi_{\mu\nu} = h_{\mu\nu} - \frac{1}{2}h\eta_{\mu\nu}$$

$$h = \eta^{\mu\nu}h_{\mu\nu}$$

In vacuum, equation (2.4) becomes

$$\Box\phi_{\mu\nu} = 0. \tag{2.5}$$

Equation (2.5) indicates the existence of waves propagating in vacuum, which is called gravitational waves.

For simplicity, consider plane waves propagating in the x^3, i.e. z, direction. By TT (transverse traceless) gauge transformation, one can obtain $\phi_{\mu\nu}$ and corresponding $h_{\mu\nu}$,

$$\phi_{\mu\nu} = h_{\mu\nu} = \begin{pmatrix} 0 & 0 & 0 & 0 \\ 0 & h_+ & h_\times & 0 \\ 0 & h_\times & -h_+ & 0 \\ 0 & 0 & 0 & 0 \end{pmatrix} \exp\left[ik(-x^0 + x^3)\right]. \tag{2.6}$$

This result shows gravitational waves are transverse waves and have two polarization:

$$\underbrace{\begin{pmatrix} 0 & 0 & 0 & 0 \\ 0 & h_+ & 0 & 0 \\ 0 & 0 & -h_+ & 0 \\ 0 & 0 & 0 & 0 \end{pmatrix}}_{\langle + \text{ mode}\rangle} \quad \text{and} \quad \underbrace{\begin{pmatrix} 0 & 0 & 0 & 0 \\ 0 & 0 & h_\times & 0 \\ 0 & h_\times & 0 & 0 \\ 0 & 0 & 0 & 0 \end{pmatrix}}_{\langle \times \text{ mode}\rangle}. \tag{2.7}$$

By calculating energy tensor, one can obtain the energy flow of z direction expressed using energy flux, S_3,

$$S_3 = \frac{c^5 k^2}{32\pi G}(|h_+|^2 + |h_\times|^2) \tag{2.8}$$

This result shows independent energy flux for the each polarization, similar to electromagnetic waves. The nature of the two polarization will be shown later in Section 2.3.

§2.2 Radiation of Gravitational Waves

Now turn attention to the radiation of gravitational waves. One solution of equation (2.4) can be expressed as following retarded potential:

$$\phi_{\mu\nu}(t, x, y, z) = \frac{4G}{c^4} \int \frac{T_{\mu\nu}(t - r'/c, x', y', z')}{r'} \mathrm{d}x' \mathrm{d}y' \mathrm{d}z', \tag{2.9}$$

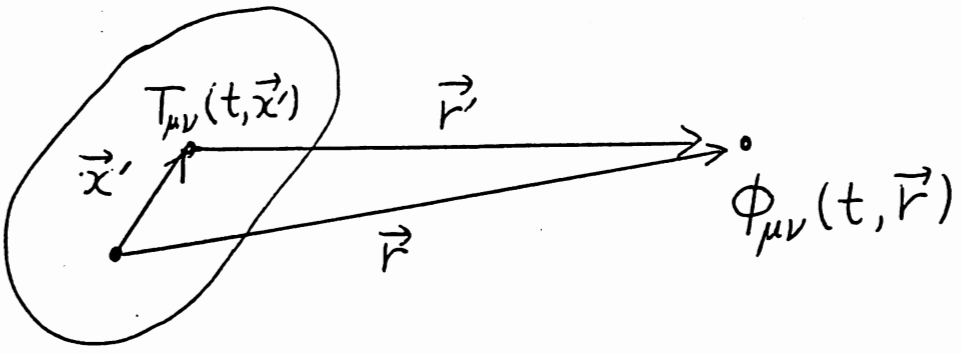

Fig.2.1 Radiation of gravitational waves from small area.

which indicates gravitational waves radiated from an restrict area (x', y', z'). By expanding $T_{\mu\nu}(t-r'/c, x', y', z')$ using approximation of small radiation area (mass density $\rho(x', y', z')$) compared with the wave length of radiated waves, one can obtain

$$\phi_{ij}(t,x,y,z) = \frac{2G}{c^4 r}\frac{\mathrm{d}^2}{\mathrm{d}t^2}\int \rho(t-r/c, x', y', z') x'^i y'^j \mathrm{d}x'\mathrm{d}y'\mathrm{d}z' \tag{2.10}$$

If we consider waves propagating z direction, at sufficiently distant point from the radiation area we have

$$\begin{aligned} h_+(t) &= \frac{2G}{c^4 r}\frac{\mathrm{d}^2}{\mathrm{d}t^2}\frac{D_{11}(t-r/c) - D_{22}(t-r/c)}{2} \\ h_\times(t) &= -\frac{2G}{c^4 r}\frac{\mathrm{d}^2}{\mathrm{d}t^2} D_{12}(t-r/c), \end{aligned} \tag{2.11}$$

where D_{ij} is quadrupole momentum tensor of the area,

$$D_{ij}(t) = \int \rho(t, x', y', z')\left(x'_i x'_j - \frac{1}{3}\delta_{ij}\sum_k x'^2_k\right)\mathrm{d}x'\mathrm{d}y'\mathrm{d}z'. \tag{2.12}$$

In this case, from equation (2.8) energy flux can be given by

$$S_3 = \frac{G}{4\pi c^5 r^2}\left[\overline{\left(\frac{\mathrm{d}^3}{\mathrm{d}t^3}\frac{D_{11}-D_{22}}{2}\right)^2} + \overline{\left(\frac{\mathrm{d}^3}{\mathrm{d}t^3}D_{12}\right)^2}\right] \tag{2.13}$$

By integrating energy flux over the sphere surrounding the radiation area, one can obtain the energy loss rate of the source carried away by gravitational waves.

$$P = \frac{G}{5c^5} \sum_{i,j} \overline{\left(\frac{\mathrm{d}^3}{\mathrm{d}t^3} D_{ij}\right)^2} \tag{2.14}$$

Now let's estimate strength of gravitational waves radiated from a stellar object or a terrestrial source. Equation (2.11) can be written as,

$$h \sim \frac{2G}{c^4} \frac{\ddot{D}}{r} = \frac{r_{\mathrm{g}}}{r} \frac{\Delta M}{M}, \tag{2.15}$$

where

$$\begin{aligned} r_{\mathrm{g}} &= \frac{2GM}{c^2} \qquad \text{(Schwarzschild radius of mass } M\text{)} \\ \Delta M &= \frac{\ddot{D}}{c^2} \qquad \text{(mass corresponding to 2nd time derivative quadrupole moment)} \end{aligned} \tag{2.16}$$

Above formulae indicate that a massive and rapidly rotating dumbbell can radiate gravitational waves. In the case of a dumbbell with two masses M, distance ℓ apart each other, and rotating with angular frequency ω,

$$\begin{aligned} h &\sim \frac{r_{\mathrm{g}}}{2r} \left(\frac{\ell\omega}{c}\right)^2 \\ &\sim 3 \times 10^{-39} \left(\frac{M}{10^3 \mathrm{kg}}\right) \left(\frac{\ell}{1\mathrm{m}}\right)^2 \left(\frac{\omega}{2\pi \times 1\mathrm{kHz}}\right)^2 \left(\frac{r}{300\mathrm{km}}\right)^{-1}. \end{aligned} \tag{2.17}$$

On the other hand, a star with solar mass, $M_\odot$, in our galaxy radiates,

$$h \sim 1 \times 10^{-17} \left(\frac{\Delta M}{M_\odot}\right) \left(\frac{r}{10\mathrm{kpc}}\right)^{-1}. \tag{2.18}$$

These estimation shows we have to expect gravitational waves from astronomical sources. But such a source as described in equation (2.18) is considered to be rare in our galaxy. One of the promising sources is coalescing binary neutron stars and super nova explosion. In our galaxy, super nova explosion occurs a few events in a century, and known three binary pulsar systems will coalesce more than 100 million years future. If we extend our view from our galaxy to Virgo cluster ($r \sim 10\mathrm{Mpc}$) which includes $\sim$ 100 galaxies, the event rate will be several events

par year. In order to detect these events, the sensitivity of the detector should be better than,

$$h \sim 1 \times 10^{-20} \Big(\frac{\Delta M}{M_\odot}\Big) \Big(\frac{r}{10\mathrm{Mpc}}\Big)^{-1}. \tag{2.19}$$

With such detectors, gravitational wave astronomy can be established. Details of sources and astronomical features have been described in Section 1.1.

§2.3 Effect of Gravitational Waves

In this section, we will describe what effect is induced by gravitational waves and how to detect them.

First, let's think of effect on a test mass which is freely moving, namely without any force applied. A free particle obeys following geodesic equation:

$$\frac{\mathrm{d}^2 x^\alpha}{\mathrm{d}\tau^2} + \Gamma^\alpha_{\mu\nu} \frac{\mathrm{d}x^\mu}{\mathrm{d}\tau} \frac{\mathrm{d}x^\nu}{\mathrm{d}\tau} = 0. \tag{2.20}$$

If the particle is initially at rest,

$$\frac{\mathrm{d}^2 x^\alpha}{\mathrm{d}\tau^2} + c^2 \Gamma^\alpha_{00} = 0. \tag{2.21}$$

By applying first order approximation of $h_{\mu\nu}$, $\Gamma^\alpha_{00} \simeq 0$, equation (2.21) becomes,

$$\frac{\mathrm{d}^2 x^\alpha}{\mathrm{d}\tau^2} = 0, \tag{2.22}$$

therefore we have $x^i \equiv 0$, which means gravitational waves do not induce the position change of a mass. Then if we think of the proper distance, $\Delta\ell$, between such free masses, distance ϵ apart each other on the x axis,

$$\begin{aligned} \Delta\ell &\equiv \int |\mathrm{d}s^2|^{\frac{1}{2}} = \int |g_{\alpha\beta} \mathrm{d}x^\alpha \mathrm{d}x^\beta|^{\frac{1}{2}} \\ &= \int_0^\epsilon |g_{xx}|^{\frac{1}{2}} \mathrm{d}x \simeq |g_{xx}(x=0)|^{\frac{1}{2}} \epsilon \\ &\simeq \Big[1 + \frac{1}{2} h_{xx}(x=0)\Big] \epsilon \end{aligned} \tag{2.23}$$

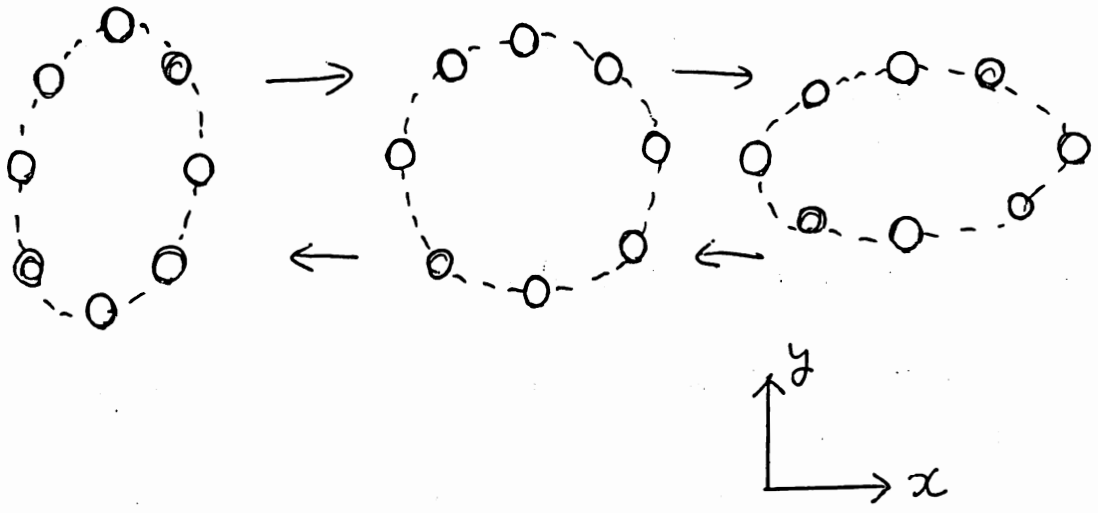

Fig.2.2(a) Displacement of free particles for h_+ polarization.

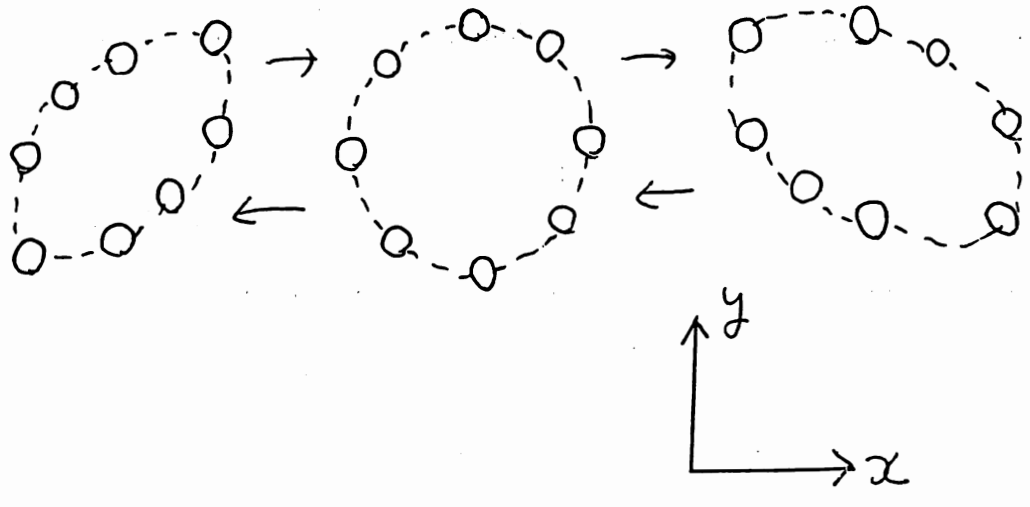

Fig.2.2(b) Displacement of free particles for $h_\times$ polarization.

Equation (2.23) indicates gravitational waves change proper distance between two particles, and by measuring the distance gravitational waves can be detected.

In order to clarify the nature of the waves in detail, assume the two particles are freely rest at the position x^α and $x^\alpha + \xi^\alpha$, respectively: in other words two particles are separated by infinitesimal vector ξ^α. It obey the equation

$$\frac{\mathrm{d}^2}{\mathrm{d}\tau^2}\xi^\alpha = R^\alpha{}_{\mu\nu\beta}\frac{\mathrm{d}x^\mu}{\mathrm{d}\tau}\frac{\mathrm{d}x^\nu}{\mathrm{d}\tau}\xi^\beta. \tag{2.24}$$

First order calculation about $h_{\mu\nu}$ shows the displacement induced by gravitational waves, $\delta\xi^\alpha$, to be,

$$\begin{pmatrix} \delta\xi^x \\ \delta\xi^y \\ \delta\xi^z \end{pmatrix} = \frac{1}{2}\begin{pmatrix} h_+ & h_\times & 0 \\ h_\times & -h_+ & 0 \\ 0 & 0 & 0 \end{pmatrix}\begin{pmatrix} \xi^x \\ \xi^y \\ \xi^z \end{pmatrix}\exp\left[\mathrm{i}k(-ct+z)\right] \tag{2.25}$$

when the waves is expressed as equation (2.6). The meaning of two polarization, +-mode and ×-mode, can be clearly understood by displaying the displacement of free particles placed circularly on the x–y plane (Fig.2.2).

If we place free mirrors and form an interferometer to detect distance between them (Fig.2.3), it corresponds to an interferometric gravitational wave detector. While, if we place a elastic body (bar) on the x–y plane, vibration mode like Fig.2.4 is induced and the bar continues to vibrate after passing gravitational waves away; this is a principle of a resonant type gravitational wave antenna. Current status of detectors of both type has been described in Section 1.2. Hereafter we will deal with only interferometric detectors.

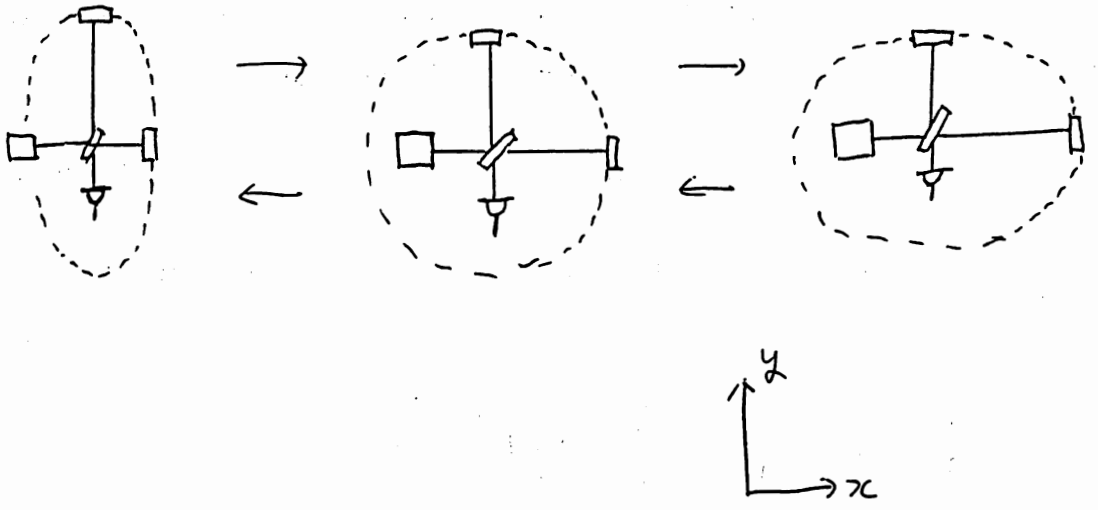

Fig.2.3 Detection of gravitational waves with an interferometer.

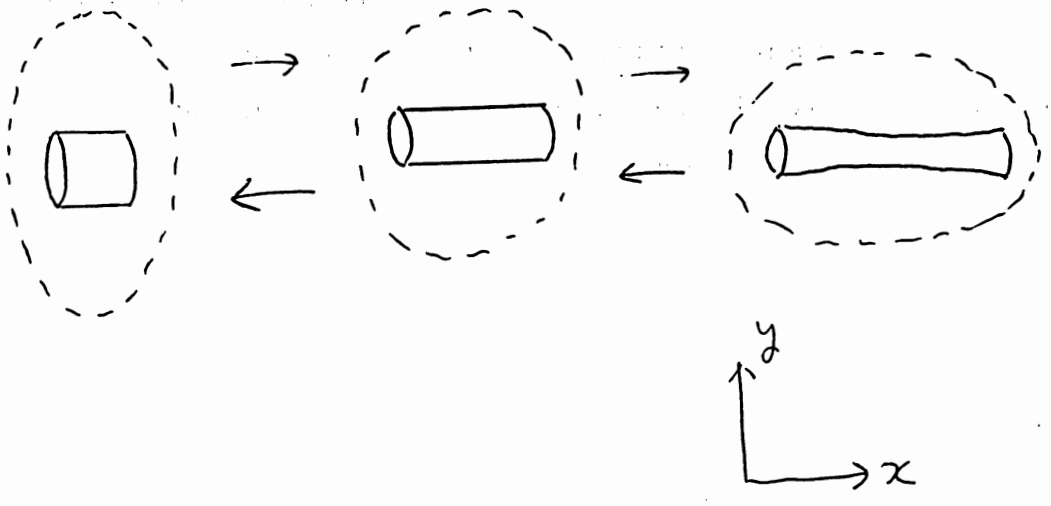

Fig.2.4 Detection of gravitational waves with a bar detector.

3. Detection of Gravitational Waves with an Interferometer

§3.1 Interferometric Gravitational Wave Detector

The principle of the gravitational wave detector using an Michelson interferometer is shown in Fig.3.1. Each mirror and beam splitter is suspended in order to realize 'free-fall' at higher frequencies than their resonant frequency. As described in Fig.2.3, the path length between a mirror and a beam splitter changes oppositely in x direction against y direction. Then, the effect of gravitational waves can be detected from the interfered fringe because Michelson interferometer is sensitive to path difference between two arm lengths, in other words sensitive to the phase difference of each arm.

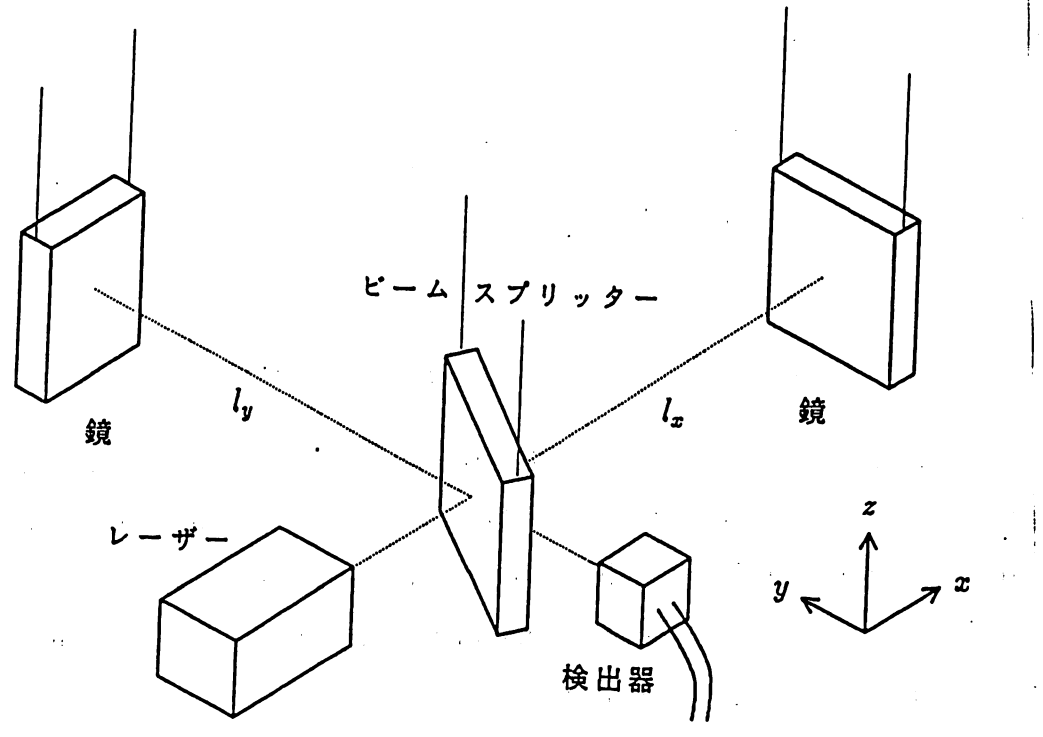

Fig.3.1 Gravitational wave detector using a Michelson interferometer.

In order to calculate the phase difference induced by gravitational waves, the phase of one arm is derived by integrating infinitesimal phase change of equation (2.25). Assume gravitational waves of +-mode, $h(t) = h_+(t)$, comes to the interferometer with arm length of ℓ_1 and ℓ_2. The phase change of the round trip of one arm 1, φ_1, can be calculated as,

$$\begin{aligned}
\varphi_1(t) &= \int_0^{\ell_1} \frac{\omega}{c} \mathrm{d}x + \int_{\ell_1}^{2\ell_1} \frac{\omega}{c} \mathrm{d}x \\
&\simeq \frac{\omega}{c} \int_0^{2\ell_1} \left[1 + \frac{1}{2} h(t')\right] \mathrm{d}\xi \\
&= \frac{2\omega\ell_1}{c} + \frac{\omega}{2c} \int_0^{2\ell_1} h(t') \mathrm{d}\xi \\
&\simeq \frac{2\omega\ell_1}{c} + \frac{\omega}{2c} \int_{t-2\ell_1/c}^{t} h(t') c \mathrm{d}t' \\
&= \frac{2\omega\ell_1}{c} + \frac{\omega}{2} \int_{t-2\ell_1/c}^{t} h(t') \mathrm{d}t',
\end{aligned} \tag{3.1}$$

where ω is a frequency of the laser light. As gravitational waves oppositely change phase of arm 2, φ_2 is,

$$\varphi_2(t) = \frac{2\omega\ell_2}{c} - \frac{\omega}{2} \int_{t-2\ell_2/c}^{t} h(t') \mathrm{d}t'. \tag{3.2}$$

The detected phase difference $\Delta\varphi$ is,

$$\begin{aligned}
\Delta\varphi(t) &= \varphi_1(t) - \varphi_2(t) \\
&\simeq \frac{2\omega}{c}(\ell_1 - \ell_2) + \omega \int_{t-2\ell/c}^{t} h(t') \mathrm{d}t',
\end{aligned} \tag{3.3}$$

when approximating $\ell_1 \simeq \ell_2 \simeq \ell$. The first term of the last expression in Eq.(3.3) is static phase change due to the arm difference of the interferometer, while the second term is a phase change induced by gravitational waves. When $h(t)$ slowly changes compared to the round trip time of the arm, phase change induced by gravitational waves, $\delta\varphi_{\mathrm{gw}}(t)$ is reduced to,

$$\begin{aligned}
\delta\varphi_{\mathrm{gw}}(t) &\simeq \omega \frac{2\ell}{c} h(t) \\
&= 2\frac{2\pi}{\lambda} h(t)\ell,
\end{aligned} \tag{3.4}$$

where λ is the wavelength of the laser light. Equation (3.4) shows that the longer the arm length becomes, the easier to detect. If $h(t)$ varies rapidly and has Fourier spectrum $h(\Omega)$, where Ω is a Fourier angular frequency of gravitational waves, $h(t)$ and $\delta\varphi(\Omega)$ can be expressed as

$$h(t) = \int_{-\infty}^{\infty} h(\Omega) \mathrm{e}^{\mathrm{i}\Omega t} \mathrm{d}\Omega \tag{3.5}$$

$$\begin{aligned}
\delta\varphi(t) &= \omega \int_{t-2\ell/c}^{t} \int_{-\infty}^{\infty} h(\Omega) \mathrm{e}^{\mathrm{i}\Omega t} \mathrm{d}\Omega \mathrm{d}t \\
&= 2\omega \int_{-\infty}^{\infty} \sin\left(\frac{\Omega\ell}{c}\right) \frac{h(\Omega)}{\Omega} \mathrm{e}^{-\mathrm{i}\frac{\Omega\ell}{c}} \mathrm{e}^{\mathrm{i}\Omega t} \mathrm{d}t \\
&\equiv \int_{-\infty}^{\infty} \delta\varphi(\Omega) \mathrm{d}\Omega,
\end{aligned}$$

therefore

$$\delta\varphi(\Omega) = H_{\mathrm{M}}(\Omega) h(\Omega). \tag{3.6}$$

Here we define the response function for Michelson interferometer to gravitational waves with frequency Ω,

$$H_{\mathrm{M}}(\Omega) = 2\frac{\omega}{\Omega} \sin\left(\frac{\Omega\ell}{c}\right) \mathrm{e}^{-\mathrm{i}\frac{\Omega\ell}{c}}. \tag{3.7}$$

Equation (3.7) indicates the effect of gravitational waves vanishes when $\ell = N\lambda_{\mathrm{gw}}$ (m:integer, λ_{gw}:wave length of gravitational waves) satisfies, because the phase change of light going forth is cancelled out when it comes back. The arm length is optimized when $\ell_{\mathrm{opt}} \simeq (2N+1)\lambda_{\mathrm{gw}}/4$ satisfies. Typical frequency of gravitational waves radiated from super novae or coalescing binary neutron stars are near 1kHz, therefore $\ell_{\mathrm{opt}} \simeq$75km.

Since it seems very hard to construct an interferometer with such long arms, several types of folded interferometer are proposed. One is Delay Line type interferometer which has folded arms (Fig.3.2). An N-folded Delay Line with arm length ℓ_{DL} corresponds to Michelson interferometer with arm length $\ell = N\ell_{\mathrm{DL}}$. Hence, the response function for Delay Line interferometer is,

$$H_{\mathrm{DL}}(\Omega) = 2\frac{\omega}{\Omega} \sin\left(\frac{\Omega N\ell}{c}\right) \mathrm{e}^{-\mathrm{i}\frac{\Omega N\ell}{c}}. \tag{3.8}$$

Another type is a Fabry-Perot interferometer which has Fabry-Perot cavity for each arm and light goes back and forth in the cavity (Fig.3.2). By summing up the phase change of each going and coming light, total detected phase can be calculated. Assume $r_{1,2}$ and $t_{1,2}$ are amplitude reflectivity and transmittance of front mirror (1) and end mirror (2), and cavity length is controlled near resonance. Detected light effected by gravitational waves can be calculated as,

$$
\begin{aligned}
& r_1 \exp[\mathrm{i}\phi(t,\ell=0)] - t_1^2 r_2 \exp[\mathrm{i}\phi(t,\ell=\ell_{\mathrm{FP}})] \\
& \qquad - t_1^2 r_1 r_2^2 \exp[\mathrm{i}\delta\varphi(t,\ell=2\ell_{\mathrm{FP}})] \\
& \qquad - t_1^2 r_1^2 r_2^3 \exp[\mathrm{i}\delta\varphi(t,\ell=3\ell_{\mathrm{FP}})] \\
& \qquad - \cdots \\
\simeq\ & r_1 \\
& - t_1^2 r_2 - 2\mathrm{i} t_1^2 r_2 \frac{\omega}{\Omega} \sin\left(\frac{\Omega\ell}{c}\right) \mathrm{e}^{-\mathrm{i}\frac{\Omega\ell}{c}} h(\Omega) \\
& - t_1^2 r_1 r_2^2 - 2\mathrm{i} t_1^2 r_1 r_2^2 \frac{\omega}{\Omega} \sin\left(\frac{2\Omega\ell}{c}\right) \mathrm{e}^{-2\mathrm{i}\frac{\Omega\ell}{c}} h(\Omega) \\
& - t_1^2 r_1^2 r_2^3 - 2\mathrm{i} t_1^2 r_1^2 r_2^3 \frac{\omega}{\Omega} \sin\left(\frac{3\Omega\ell}{c}\right) \mathrm{e}^{-3\mathrm{i}\frac{\Omega\ell}{c}} h(\Omega) \\
& - \cdots \\
=& \frac{r_1 - (t_1^2 + r_1^2) r_2}{1 - r_1 r_2} - 2\mathrm{i} t_1^2 r_2 \frac{\omega}{\Omega} \frac{\sin(\Omega\ell/c)}{(1 - r_1 r_2)(1 - r_1 r_2 \mathrm{e}^{-2\mathrm{i}\frac{\Omega\ell}{c}})} \mathrm{e}^{-\mathrm{i}\frac{\Omega\ell}{c}} h(\Omega) \\
=& \frac{r_1 - (t_1^2 + r_1^2) r_2}{1 - r_1 r_2} \left(1 + 2\mathrm{i}\alpha \frac{\omega}{\Omega} \frac{\sin(\Omega\ell/c)}{(1 - r_1 r_2 \mathrm{e}^{-2\mathrm{i}\frac{\Omega\ell}{c}})} \mathrm{e}^{-\mathrm{i}\frac{\Omega\ell}{c}} h(\Omega)\right) \\
\equiv& \frac{r_1 - (t_1^2 + r_1^2) r_2}{1 - r_1 r_2} \exp[\mathrm{i}\delta\varphi_{\mathrm{FP}}(\Omega)] \\
\simeq& \frac{r_1 - (t_1^2 + r_1^2) r_2}{1 - r_1 r_2} (1 + \mathrm{i}\delta\varphi_{\mathrm{FP}}(\Omega)],
\end{aligned}
$$

where

$$
\alpha = \frac{t_1^2 r_2}{(t_1^2 + r_1^2) r_2 - r_1}. \tag{3.9}
$$

Hence phase change ($\delta\varphi_{\mathrm{FP}}(\Omega)$) and response function ($H_{\mathrm{FP}}(\Omega)$) for Fabry-Perot interferometer can be written by,

$$
\delta\varphi_{\mathrm{FP}}(\Omega) = H_{\mathrm{FP}}(\Omega) h(\Omega) \tag{3.10}
$$

$$H_{\rm FP}(\Omega) = 2\alpha\frac{\omega}{\Omega}\frac{\sin(\Omega\ell/c)}{(1-r_1r_2e^{-2i\frac{\Omega\ell}{c}})}e^{-i\frac{\Omega\ell}{c}}. \tag{3.11}$$

In order to clarify the difference of the response function between Delay Line and Fabry-Perot, it is convenient to plot $|H_{\rm DL}(\Omega)|$ and $|H_{\rm FP}(\Omega)|$ against gravitational wave frequency Ω. They are expressed as,

$$|H_{\rm DL}(\Omega)| = 2\frac{\omega}{\Omega}\sin\left(\frac{\Omega N\ell}{c}\right) \tag{3.12}$$

$$|H_{\rm FP}(\Omega)| = \frac{2\alpha\omega}{\Omega(1-r_1r_2)}\frac{|\sin(\Omega\ell/c)|}{\sqrt{1+F\sin(\Omega\ell/c)}}, \tag{3.13}$$

where

$$F = \frac{4r_1r_2}{(1-r_1r_2)^2} = \left(\frac{2\mathcal{F}}{\pi}\right)^2 \tag{3.14}$$

and $\mathcal{F}$ is called finesse, an important parameter for Fabry-Perot, which expresses the sharpness of the resonance and interpreted as the number of fold. The typical response function for both type are shown in Fig.3.3. In the figure, parameters are optimized for the kHz-region gravitational waves. It shows the curve for Fabry-Perot is more smooth than that for Delay Line, and this is one of differences between them.

§3.2 Operation of the Interferometric Detector

In this section, we describe how to operate interferometer as a detector of the phase difference induced by gravitational waves. Roughly speaking, function of the interferometer can be divided into two parts: one is arm part where light goes back and forth to enhance the phase change induced by gravitational waves, and the other is detection of phase difference between both arms. Their function and operation are described in the following subsections.

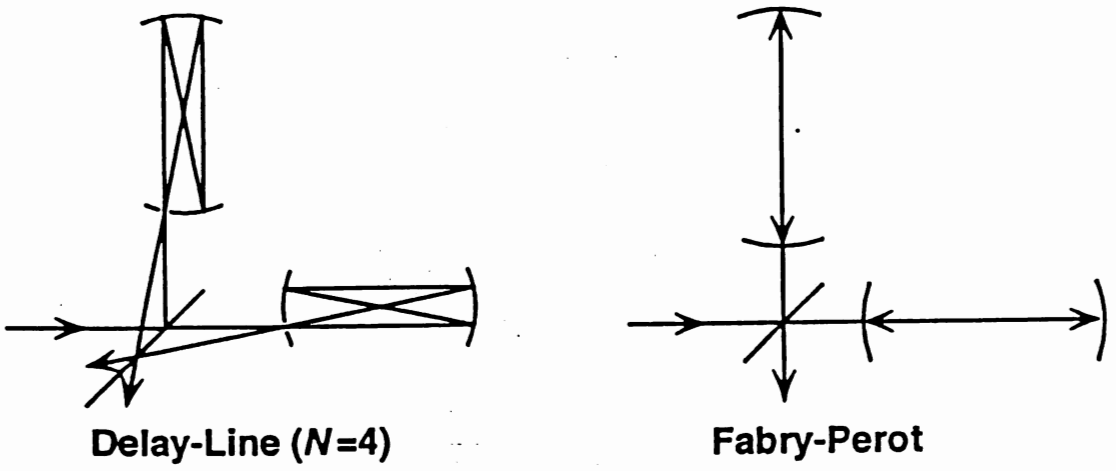

Fig.3.2 Interferometric detector of Delay Line type and Fabry-Perot type.

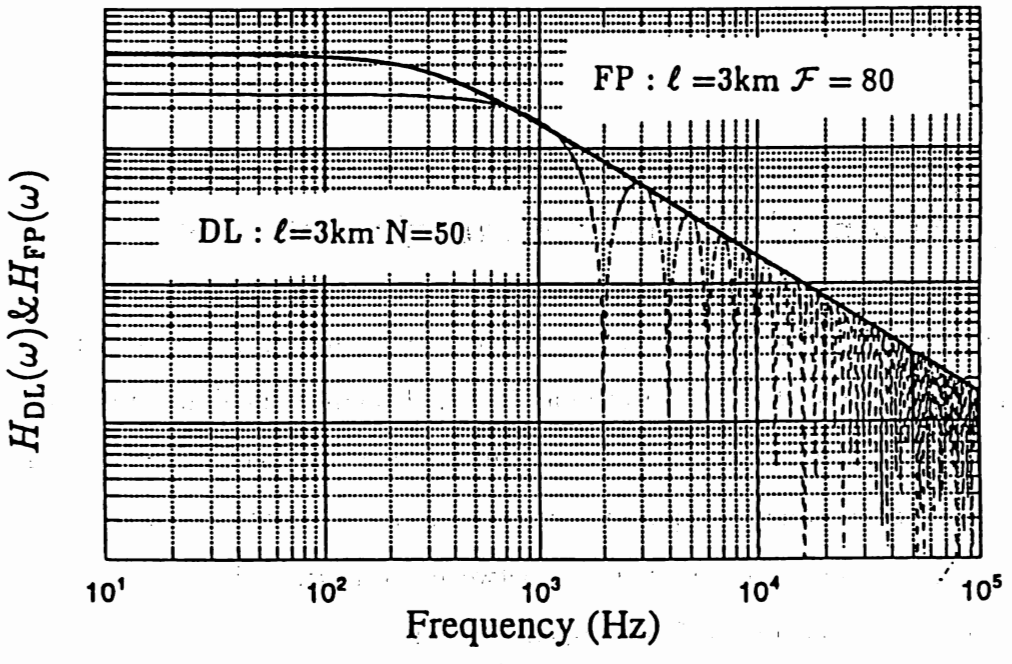

Fig.3.3 Response function of both type against gravitational waves.

3.2.1 Arm Locking

Mirrors of the interferometer are suspended to realize force-free condition as well as to isolate external vibration. That's why control system of the mirror is necessary.

Delay Line interferometer has folded optical path between two mirrors in one arm. Owing to the re-entrant condition that reflected beam goes out from the incident hole, output are less sensitive to the alignment of the mirrors; therefore simple alignment control system and damping system are needed.

As for the Fabry-Perot interferometer, more stable alignment control system and damping system are necessary since Fabry-Perot cavity is very sensitive to the alignment of its mirror. Moreover Fabry-Perot cavities of both arms are kept resonant because the phase change against the cavity length becomes maximum on resonance. In order to lock on resonance, modulation method is applied. If the incident light is phase modulated with modulation index m and modulation frequency ω_{m} (ordinarily, modulation frequency is chosen Radio Frequency for intensity noise reduction), it can be expanded when $m \ll 1$,

$$\begin{aligned} \mathrm{e}^{\mathrm{i}(\omega t + m\sin\omega_{\mathrm{m}} t)} &\simeq \mathrm{e}^{\mathrm{i}\omega t}[J_0(m) + J_1(m)(\mathrm{e}^{\mathrm{i}\omega_{\mathrm{m}} t} - \mathrm{e}^{-\mathrm{i}\omega_{\mathrm{m}} t})] \\ &= J_0(m)\mathrm{e}^{\mathrm{i}\omega t} + J_1(m)\mathrm{e}^{\mathrm{i}(\omega+\omega_{\mathrm{m}})t} - J_1(m)\mathrm{e}^{\mathrm{i}(\omega-\omega_{\mathrm{m}})t}, \end{aligned} \tag{3.15}$$

where $J_0(m)$ and $J_1(m)$ are fundamental and first order Bessel function, respectively. Equation (3.15) shows that phase modulation generates two sidebands on both side of the carrier. The reflected light from the cavity, A, can be expressed as,

$$A = J_0(m)A_{\mathrm{r}}(\omega)\mathrm{e}^{\mathrm{i}\omega t} + J_1(m)A_{\mathrm{r}}(\omega+\omega_{\mathrm{m}})\mathrm{e}^{\mathrm{i}(\omega+\omega_{\mathrm{m}})t} - J_1(m)A_{\mathrm{r}}(\omega-\omega_{\mathrm{m}})\mathrm{e}^{\mathrm{i}(\omega-\omega_{\mathrm{m}})t}, \tag{3.16}$$

where A_{r} is a response function of the lossless Fabry-Perot cavity with cavity length ℓ:

$$A_{\mathrm{r}}(\omega) = \frac{r_1 - r_2\mathrm{e}^{\mathrm{i}\omega\ell/c}}{1 - r_1 r_2 \mathrm{e}^{\mathrm{i}\omega\ell/c}}. \tag{3.17}$$

The demodulated signal for $\sin\omega_{\mathrm{m}} t$ component of quadrature can be expressed as,

$$I_{\sin} = \frac{4r_1 r_2(1-r_1^2)(1-r_2^2)\sqrt{1+\frac{4r_2^2}{(1-r_2^2)^2}\sin^2(\omega_{\rm m}\ell/c)}}{(1-r_1 r_2)^4\left[1+F\sin^2(\omega_{\rm m}\ell/c)\right]}\sin\left(\frac{\omega_{\rm m}}{c}\ell\right)\sin\left(\frac{2\omega}{c}\ell\right). \tag{3.18}$$

As this signal is proportional to $\sin\omega\ell/c$, it can be used to lock the cavity on resonance.

3.2.2 Fringe Locking

As the phase change of the light can not detect directly, we obtain it by interference of the light. When we think the Michelson interferometer, phase-changed light from each arm interfere at beamsplitter and detected signal contains the difference of the each phase, namely gravitational wave signal enhanced twice while common mode noise, such as frequency noise of the laser, cancelled.

For the Fabry-Perot type interferometer, one can extract gravitational wave signal by subtract detected signal of each arms without interfering at beamsplitter (Locked Fabry-Perot scheme). But future plan adopts recycling scheme [7] which requires dark fringe locking so as to recycle light of bright port. Normally, the interferometer is kept dark at the detector port because both of avoiding detector saturation due to high power laser light and of adopting recycling scheme mentioned above. Dark fringe locking can be realized by modulation method. Consider the path length of each arm with difference $\Delta\ell$ is reversely phase modulated, the demodulated detected signal can be expressed as:

$$I_{\sin} = 8\sin\left(\frac{2\omega}{c}\Delta\ell\right) \tag{3.19}$$

In practice, this scheme contains phase modulators between beamsplitter and each arms and they will limit the recycling gain. So, some kind of modulation technique, which has no phase modulator inside the interferometer, has been proposed. One is External Modulation [8], and another type is Pre-modulation

method proposed by Schnupp [9]. We apply pre-modulation method to the 20m Fabry-Perot prototype at National Astronomical Observatory (Mitaka), and detail of this method is described in Section 7.1.

§3.3 Noise Sources of the Interferometer

In this section, noise sources of interferometric gravitational wave detectors are described [10].

3.3.1 Shot Noise

Photon shot noise limits the sensitivity of the interferometer. The detected photocurrent, $I_{\rm D}$, involves white noise in terms of $\mathrm{A}/\sqrt{\mathrm{Hz}}$,

$$i_{\rm shot} = \sqrt{2eI_{\rm D}}, \tag{3.20}$$

where e is a elementary charge. Signal of gravitational waves to shot noise ratio decides the sensitivity of the interferometer.

Now let's calculate the signal, assuming dark fringe locking scheme using modulation method.

$$\begin{aligned} \delta\phi_{\rm shot} &= \frac{\sqrt{1-J_0(m)}}{J_1(m)}\sqrt{\frac{e}{2I_0}} \\ &\simeq \sqrt{\frac{e}{2I_0}} \qquad \text{for } m \ll 1 \end{aligned} \tag{3.21}$$

For the Fabry-Perot detector, sensitivity limited by shot noise is,

$$h_{\rm shot} = \frac{\Omega(1-r_1r_2)}{A_{\rm c}|\sin(\ell\Omega/c)|}\sqrt{\frac{\hbar(1+F\sin^2(\Omega\ell/c))}{2\omega\eta P}\Delta f}. \tag{3.22}$$

3.3.2 Intensity Noise of the Laser

Ideally, intensity noise contributes second order quantity to the signal when complete dark fringe locking and complete phase modulation are realized. Their incompleteness causes the intensity noise. If the laser light is modulated at sufficiently high frequency where intensity noise is smaller than the shot noise level, the effect of incomplete dark fringe locking due to umbalance of the interferometer and so on can be avoided in some degree. Even in this case, incomplete phase modulation, namely contribution of amplitude modulation, causes excess noise. Amplitude modulation with modulation index, m_{AM}, induce the noise into the demodulated signal.

Incomplete locking point also contribute the intensity noise to the signal. If the lock point shift by $\delta\ell$ from cavity length ℓ, sensitivity limited by intensity noise can be expressed as,

$$h_{\mathrm{AMnoise}} = \frac{\Delta\ell}{\ell}\frac{\delta I}{I} \tag{3.23}$$

3.3.3 Frequency Noise of the Laser

Frequency fluctuation of the laser strongly limit the sensitivity of the interferometer. If the arm lenth of the Michelson interferometer differs by $\Delta\ell$, excess noise due to this umbalance of the interferometer limit the sensitivity of,

$$h_{\mathrm{FMarm}} = \frac{\Delta\ell}{\ell}\frac{\delta\nu}{\nu} \tag{3.24}$$

For the Fabry-Perot detector, frequency fluctuation directly affects its signal. When the cavity is locked phase of the light can be expressed using frequency of the light ν and length of the cavity ℓ,

$$\mathrm{phase} = \frac{2\pi\nu}{c}\ell = \mathrm{const.} \tag{3.25}$$

By differentiate Eq.(3.25), we have

$$h_{\mathrm{FM}} = \frac{\delta\ell}{\ell} = \frac{\delta\nu}{\nu}. \tag{3.26}$$

Although we can expect common mode noise rejection by subtraction at beamsplitter, we must make big effort to stabilize laser frequency. This is why we apply mode cleaner cavity as a reference of frequency stabilization.

3.3.4 Beam Jitter of the Laser

Laser beam geometry, such as beam direction and beam shape, fluctuates originating from instability of laser cavity and vibration of the optics etc. Such beam jitter would be cancelled if the interferometer could be built perfectly, but it couples the imperfection and produces noise into the signal.

If beamsplitter tilts the angular α from its symmetric position, it means that wave front at the beamsplitter deviates the angular α. Lateral beam movement δx produces phase fluctuation of,

$$\delta\phi = \frac{2\pi}{\lambda} 2\alpha\delta x \tag{3.27}$$

It corresponds to the noise of,

$$h_{\mathrm{BStilt}} = 2\alpha\frac{\delta x}{\ell} \tag{3.28}$$

Another effect of the beam jitter is to degrade matching factor for Fabry-Perot cavity, which produce intensity fluctuation of the reflected light. This flutuation behaves like amplitude noise with modulation, which is detected and then demodulated, resulting in the excess noise for the signal. This effect also couples initial mismatching δM, which decides the sensitivity.

3.3.5 Thermal Noise of the Mirror

As the mirrors of the interferometer suspended as pendulums, thermal noise of the pendulum motion limits the displacement sensitivity. Internal mode of the

mirror, e.g. vibration of mirror mass itself, also produce themal noise. Thermal noise of a harmonic mode follows the equation [11],

$$m\Big\{-\omega^2+\omega_0^2\Big[1+\mathrm{i}\phi(\omega)\Big]\Big\}x(\omega)=f_{\mathrm{N}}(\omega) \tag{3.30}$$

$$<f_{\mathrm{N}}(\omega)^2>=\frac{4m\omega_0^2\phi(\omega)k_{\mathrm{B}}T}{\omega} \tag{3.31}$$

where x, m, ,Q, ω_0, and T are coordinate (e.g. displacement), reduced mass, quality factor, resonant frequency of the mode, and temperature, respectively. Thermal noise can be derived from Eq.(3.30) and (3.31),

$$<x(\omega)^2>=\frac{4k_{\mathrm{B}}T}{\omega}\frac{\omega_0^2\phi(\omega)}{m\Big|-\omega^2+\omega_0^2[1+\mathrm{i}\phi(\omega)]\Big|^2} \tag{3.32}$$

3.3.6 Seismic Noise

Major noise source below $\sim$ 10Hz is seismic noise. Typical ground vibration is known to obey [12],

$$y(\omega)\sim 10^{-7}\Big(\frac{2\pi\times 1\mathrm{Hz}}{\omega}\Big)^2[\mathrm{m}/\sqrt{\mathrm{Hz}}] \tag{3.33}$$

where $y(\omega)$ and ω are displacement spectrum and angular frequency of vibration in Hz, respectively. For the single pendulum suspension, mirror motion excited by seismic vibration $x(\omega)$ can be expressed as,

$$x(\omega)\sim\frac{\omega_0^2+\mathrm{i}\omega_0\omega/Q}{-\omega^2+\mathrm{i}\omega_0\omega/Q+\omega_0^2}\times 10^{-7}\Big(\frac{2\pi\times 1\mathrm{Hz}}{\omega}\Big)^2 \tag{3.34}$$

3.3.7 Residual Gas

Refractive index fluctuation due to residual gas causes fluctuation of optical path length and it cannot be distinguished from gravitational wave signal. For the prototype detector, ordinary high vacuum $p\sim 10^{-4}$Pa does not affect signal, but future detector which has long arm $\ell\sim$ 3km may be affected by residual gas noise.

Although it is very difficult to estimate this type of noise precisely, several formulae have been calculated which is something like [13],

$$h_{\mathrm{gas}} \sim \left[\frac{1}{4\pi}\frac{16\sqrt{2}}{\ell\sqrt{\pi}}\frac{(n_0-1)^2}{(A_0/V_0)u_0\sqrt{\ell\lambda}}\left(\frac{p}{p_0}\right)\left(\frac{T_0}{T}\right)^{\frac{3}{2}}\right]^{\frac{1}{2}}, \tag{3.35}$$

where n_0, V_0, T_0, and p_0 are refractive index, volume, temperature, and pressure of a normal state, respectively; A_0 is Avogadro number.

4. Mode Cleaner

§4.1 Mode Cleaner

The name "Mode Cleaner" originally comes from its function, mode selector which excludes spurious beam geometry [14]. This function can be realized by forming Fabry-Perot interferometer. The higer mode of the incident beam can not transmit owing to its mode selectivity, which can be translated as frequency distinction between higher mode and TEM_{00} mode of the cavity. Hence, mode of the incident beam except TEM_{00} mode cannot transmit through the Fabry-Perot resonant at frequency corresponding to TEM_{00} mode.

As such cavity is resonant at a certain frequency, this cavity can also be utilized as a frequency reference. In this thesis, we call Mode Cleaner as frequency stabilization system referred to suspended Fabry-Perot cavity, as well as mode selector.

4.1.1 Fabry-Perot cavity

Here, let's consider basic property of Fabry-Perot cavity (see reference [15] in detail).

Assuming incident light is expressed by $A_0 e^{i\omega t}$, reflected and transmitted light can be evaluated as,

$$\begin{aligned} A_r &= \frac{r_1 - (r_1^2 + t_1^2) r_2 e^{-2i\omega\ell/c}}{1 - r_1 r_2 e^{-2i\omega\ell/c}} A_0 e^{i\omega t} \\ A_t &= \frac{t_1 t_2 e^{-i\omega\ell/c}}{1 - r_1 r_2 e^{-2i\omega\ell/c}} A_0 e^{i\omega t}. \end{aligned} \tag{4.1}$$

Therefore intensity of transmitted light is

$$\begin{aligned} I_t &= |A_t|^2 \\ &= \left(\frac{t_1 t_2}{1 - r_1 r_2}\right)^2 \frac{1}{1 + F \sin^2(\omega\ell/c)} I_0, \end{aligned} \tag{4.2}$$

where

$$F = \frac{4r_1 r_2}{(1 - r_1 r_2)^2}. \tag{4.3}$$

Frequency interval for satisfying resonant condition, $\sin(\omega\ell/c) = 0$, is called Free Spectral Range, which can be expressed

$$\nu_{\mathrm{FSR}} = \frac{c}{2\ell} \tag{4.4}$$

The important parameter, Finesse ($\mathcal{F}$), is defined as ratio between Full Width of Half Maximum (FWHM) frequency and free spectral range.

$$\begin{aligned} \mathcal{F} &= \frac{\nu_{\mathrm{FSR}}}{\nu_{\mathrm{FWHM}}} \\ &= \frac{\pi\sqrt{r_1 r_2}}{1 - r_1 r_2} \end{aligned} \tag{4.5}$$

4.1.2 Gaussian Mode

In previous subsection, we treat laser beam in geometical optics. Precisely speaking, laser beam propagetes divergently due to its diffraction. Hence mirrors of the cavity must be formed by such mirrors that match the wavefront of the laser. If sphere mirrors form Fabry-Perot cavity, mode in the cavity can be expressed as,

$$\psi_{l,m} = \frac{w_0}{w(z)} H_l\left(\frac{\sqrt{2}x}{w(z)}\right) H_m\left(\frac{\sqrt{2}y}{w(z)}\right) \exp\left[-\frac{x^2 + y^2}{w^2(z)} - \mathrm{i}k\frac{x^2 + y^2}{2R(z)} - \mathrm{i}kz + \mathrm{i}(l + m + 1)\eta\right], \tag{4.6}$$

where

$$w(z) = w_0\left[1 + \left(\frac{\lambda z}{\pi w_0^2 n}\right)^2\right]$$

$$R(z) = z\left[1 + \left(\frac{\pi w_0^2 n}{\lambda z}\right)^2\right]$$

$$\eta = \tan^{-1}\left(\frac{\lambda z}{\pi w_0^2 n}\right)$$

$$n = l + m + 1,$$

and z denotes coordinates in the direction of beam propagation axis.

Since Gaussian mode forms complete system, incident beam can be expanded by cavity mode as

$$\psi_{\text{incident}} = \sum_{l,m} c_{l,m}\psi_{l,m}. \tag{4.7}$$

For the cavity whose mirrors have curvature of R_1 and R_2, mode of the cavity is stable when

$$0 \leq g_1 g_2 \leq 1 \tag{4.8}$$

satisfies, where

$$g_{1,2} = 1 - \frac{\ell}{R_{1,2}} \tag{4.9}$$

For fundamental (TEM_{00}) mode, the resonant frequency of the cavity is given by previous subsection. As for other higher mode, resonant frequency can be given by

$$\begin{aligned} \nu_{l,m} &= \frac{c}{2\ell}[n + (l + m + 1)\gamma] \\ \gamma &= \frac{1}{\pi}\cos^{-1}\sqrt{g_1 g_2} \end{aligned} \tag{4.10}$$

§4.2 Mode Cleaner as a mode selector

As mentioned in Section 4.1.2, incident beam can be expanded by cavity eigen modes. Moreover, resonant frequencies of cavity modes are generally different from the other higer modes when the resonant frequencies are not degenerated. Considering the transmitted light from such cavity that has resonant frequency for fundamental mode, the light contains only fundamental mode and the other higher modes are reflected away, therefore reformation of incident beam can be realized by this cavity. If we utilize such reformed beam for main detector, high contrast will be expected.

Another effect by using transmitted light is reduction of beam jitter noise , because fluctuation of beam direction can be expressed as fluctuation of higher mode contribution. Most significant contribution for such jitter is first and second order transverse mode. If incident beam tilts angle α and shifts optical axis a from

cavity axis, incident beam (U'_{00}) can be expressed using fundamental (U_{00}) and first order cavity mode (U_{10}) as [16],

$$U'_{00} \simeq U_{00} + (\frac{a}{w_0} + \mathrm{i}\frac{kw_0\alpha}{2})U_{10} \tag{4.11}$$

Variation of beam size (δw) and waist position (δb) causes second order modes,

$$U'_{00} \simeq U_{00} + (\mathrm{i}\frac{\delta b}{kw_0^2} + \frac{\delta w}{w_0})\frac{\sqrt{2}}{2}(U_{20} + U_{02}) \tag{4.12}$$

Suppression ratio for such higer modes is dependent on difference of resonant frequency between fundamental mode and higer mode as well as reflectivity of mirrors. Suppression ratio for TEM_{lm} mode to fundamental mode can be evaluated as

$$S_{lm} = \frac{1}{\sqrt{1 + F\sin^2\left[(l+m)\cos^{-1}\sqrt{g_1 g_2}\right]}} \tag{4.13}$$

§4.3 Mode Cleaner as a Frequency Reference

Mode cleaner cavity is a Fabry-Perot cavity which can be regarded as frequency discriminator, and it can be utilized as a frequency reference. Now, let's consider frequency stablization system using Pound-Drever method [17]; in this method reflected light for phase modulated incident beam is utilized to obtain difference between resonant frequency of the cavity and laser frequency.

Signal for frequency noise of incident laser (intensity I_0) can be expressed as

$$I_{\mathrm{sig}} = 8I_0 J_0(m)J_1(m)\frac{F\ell}{\pi c}\frac{2\pi\delta\nu_{\mathrm{FM}}}{\sqrt{1+(\Omega/\omega_{\mathrm{c}})^2}}, \tag{4.14}$$

where

$$\omega_{\mathrm{c}} = \frac{\pi c}{2F\ell}. \tag{4.15}$$

On the other hand, shot noise at the detector is,

$$I_{\mathrm{shot}} = \sqrt{2}\sqrt{2h\nu\eta I_0\left(1 - J_0^2(m)\right)}, \tag{4.16}$$

where h and η are Planck constant and quantum efficiency of the detector, respectively.

Hence, attainable frequency stability limited by shot noise can be expressed as

$$\delta\nu_{\mathrm{shot}} = \frac{c}{4\mathcal{F}\ell}\sqrt{\frac{h\nu\eta}{2I_0}}\sqrt{1+(\Omega/\omega_c)^2} \tag{4.17}$$

for infinitesimal modulation index m.

§4.4 Design of Mode Cleaner

Each parameter, such as reflectivity, finesse, etc., should be defined by considering function of Mode Cleaner as mode selector and frequency reference.

Firstly, utilizing transmitted light demands high transmittance of the cavity, which can be realized by $r_1 = r_2$ if loss of the mirros is small. Secondly, cavity length and curvature of the mirrors define the frequency interval of transverse mode, and lower order mode, especially first and second order, should be sufficiently isolated from fundamental mode. Thirdly, F should be large in order to realize high suppression for higher mode. Large F, which means large finesse is consistent with high performance of frequency stabilization. Therefore finesse $\mathcal{F}$ should be as large as possible within the limit of high transmissivity of the cavity.

In practice we follow these lines. Detail parameters we applied are described in the following Chapter 5.

5. Mode Cleaner with 1-meter Fabry-Perot

§ 5.1 Setup

We have developed a Mode Cleaner both as mode selector and as frequency stabilization system to be incorporated into 20m Fabry-Perot prototype detector at National Astronomical Observatory.

Figure 5.1 shows the schematic diagram of the Mode Cleaner system. A 500mW Laser-Diode pumped Nd:YAG laser (LIGHTWAVE, MISER model 122, λ=1064nm) [18] is stabilized in frequency referred to a Fabry-Perot, whose mirrors are suspended independently as double pendulums housed in the vacuum chamber. One characteristics of this sytem is its independently suspended mirrors in order to reduce mechanical vibration and its length will be extended in future. The reflected light is detected as a signal, and it is fed back to MISER to stabilize at higher frequencies [19], while it is used to lock the cavity at lower frequencies.

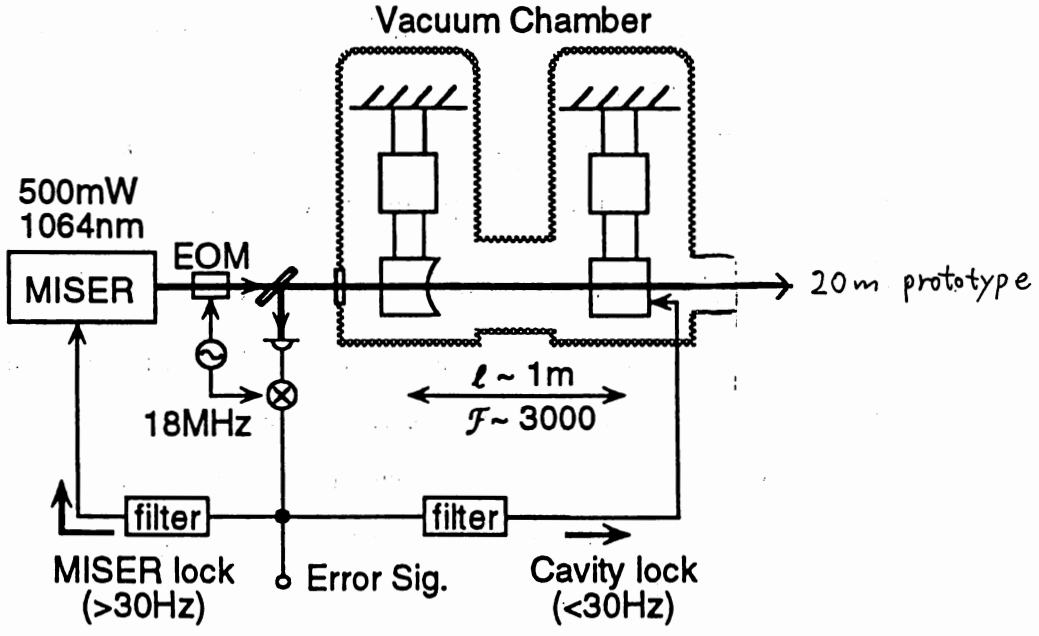

Fig.5.1 Schematic diagram of Mode Cleaner with 1-meter Fabry-Perot.

We designed the cross over frequency of about 30Hz, and the stabilization gain of 80dB at 1kHz. Transmitted light from the cavity, which is mode-selected as well as frequency-stabilized, is utilized as a light source of 20m prototype detector. The property of devices comprising Mode Cleaner is shown in the following subsections.

5.1.1 Fabry-Perot Cavity

Fabry-Perot cavity was designed to have cavity length of $\ell = 0.993$m and a combination of concave mirror with curvature radius of 1.5m and flat mirror. Front mirror (near to the laser) is concave and end mirror is flat. For the purpose of using transmitted light, both mirrors should have the same reflectivity (Section 4.4) and power loss of the mirrors must be extremely small. To satisfy these condition we use dielectric multilayer coating mirrors made by Ion Beam Spattering method. Both mirrors are made in the same manner except of their curvature (Fig.5.2). These mirrors, diameter of 20mm, are attached on the rod made of fused silica with optical contact; this method eliminates mechanical noise of the mirror mount and reduces bonding noise originating from bonding material.

In order to estimate quality of the mirrors, we made some experiments both on the measurement of finesse of the cavity and on the loss of the mirrors. Measurement of finesse was performed by two methods; sideband method and frequency response method. These experiments were performed at the same situation where the mirrors are used in operation; suspended in vacuum.

· ***Measurement of Finesse by Sideband Method***

Although finesse is originally defined as ratio of FWHM of resonant curve to free spectral range of the cavity (Section 4.1.1), resonant width is hard to measure especially for high finesse cavity. If the incident beam is modulated and contains sideband outside resonance of the cavity, resonant width can be derived from ratio of resonant width to sideband.

The setup of the measurement is shown in Fig.5.3. Incident beam is modulated in phase by EOM with 1MHz. When the cavity length accidentally comes

仕 様

型 名	L392−0000
ミラー	
基板材料	合成石英、$\Delta n < 8\times10^{-6}$
大きさ	ϕ20×6mmt
中心波長	1064nm
入射角度	0°
反射率	99.9%
透過率	0.1%
吸収・散乱損失	<50ppm
裏面ARコーティング	反射率<0.5%
ロッドへの接合	オプティカルコンタクトによる
ロッド	
材料	合成石英
大きさ	ϕ50×100mmL
内径	ϕ10mm
保持用溝	深さ0.5mmのV溝有り（2本）

寸 法

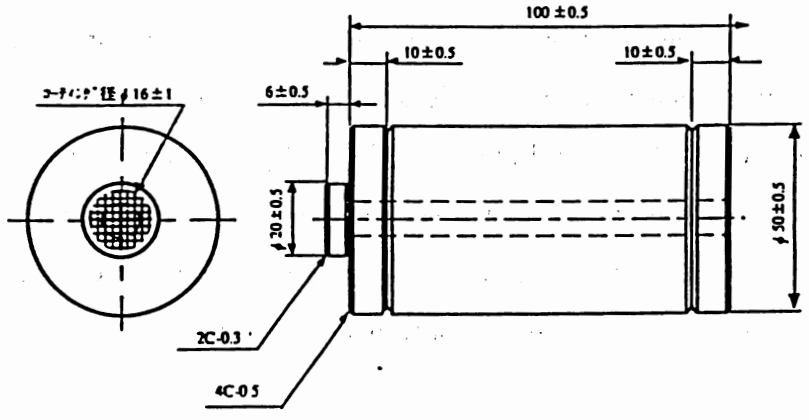

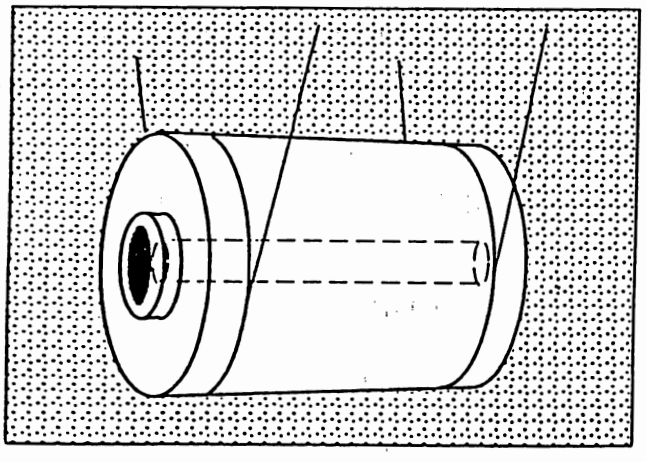

Fig.5.2 Mirror mass used as 1-meter Fabry-Perot cavity.

around on resonance, transmitted light varies as Fig.5.4. From the fitting curve of resonant peak and distance of both sideband peaks (which corresponds to 1MHz), we evaluated resonant width of 1.0×10^5Hz. Using cavity length of 0.993m, we obtained finesse of 1.5×10^3. Several other measurements including with other modulation frequencies were in good agreement with this value.

· ***Measurement of Finesse by Frequency Response***

Fabry-Perot cavity with finess of $\mathcal{F}$ works as a low-pass filter for the modulated light. The cut-off frequency of reflected light from the cavity depends on its finesse,

$$R(\omega_{\rm m}) \propto \frac{1}{1 + {\rm i}(2\mathcal{F}\ell\omega_{\rm m}/\pi c)}, \tag{5.1}$$

where $\omega_{\rm m}$ is an angular modulation frequency. Hence we could obtain finesse of the cavity from such a measurement as Fig.5.5. Fabry-Perot cavity is locked to the laser, and the laser is phase-modulated by EOM. By measuring transfer function between modulation signal and detected one, we could obtain the frequency response curve of the cavity (Fig.5.6). It agrees well with the curve for finesse of 1500, which is consistent with the results obtained by sideband method.

· ***Measurement of Loss of the Cavity***

Although loss of the mirror can be calculated from reflectivity and transmittance of the mirror, precise measurements are needed especially for high quality mirrors. In our measurement, reflectivity obtained from finesse of the cavity and transmittance of each mirror obtained from power ratio before and after mirror (Fig.5.7) are,

$$\left.\begin{aligned} r^2 &= 0.9979 \\ t^2 &= 0.0023 \end{aligned}\right\},$$

which lead to $r^2 + t^2 > 1$. Here, we cannot calculate loss of the mirror due to lack of precision of measurement; it may originate from nonlinearity of the photo detector used in measurement of transmittance.

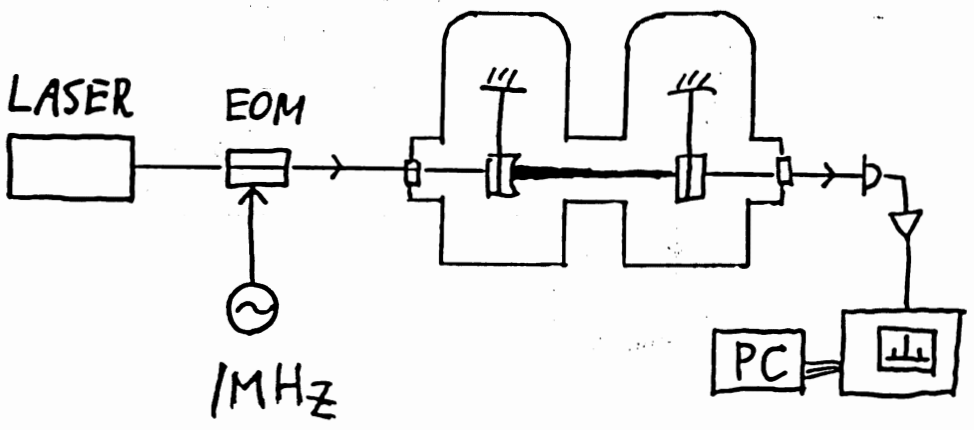

Fig.5.3 Measurement of finesse by sideband method.

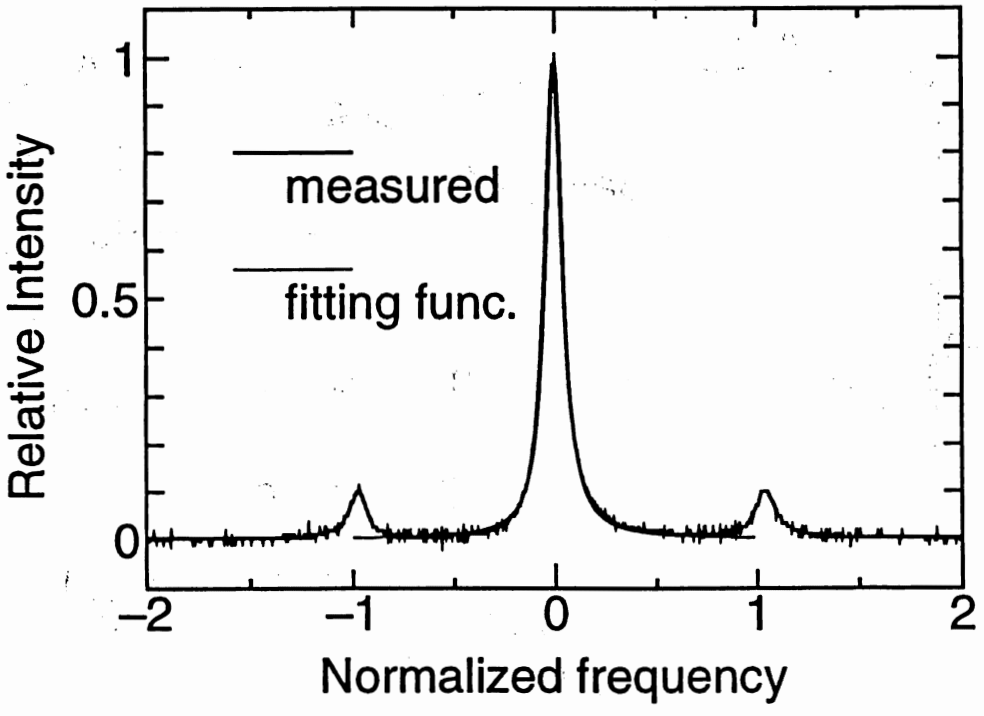

Fig.5.4 Resonant curve of transmitted light.

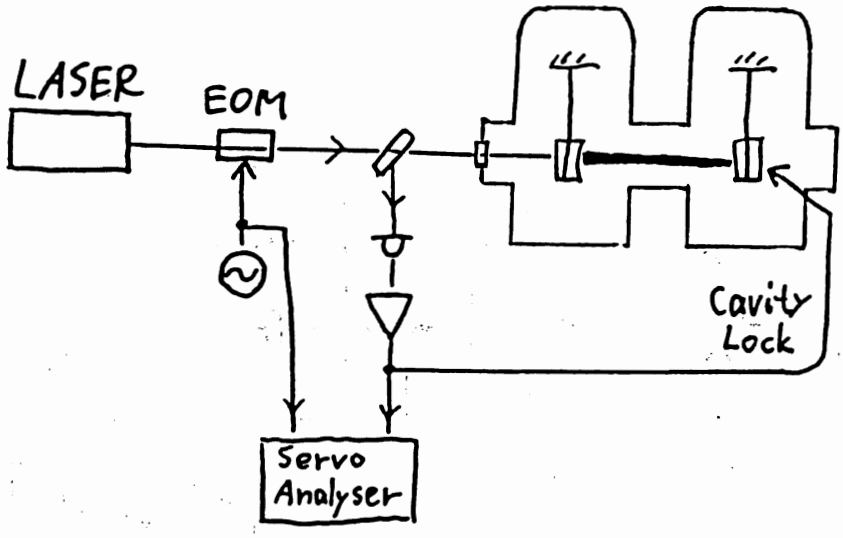

Fig.5.5 Measurement of finesse by frequency response.

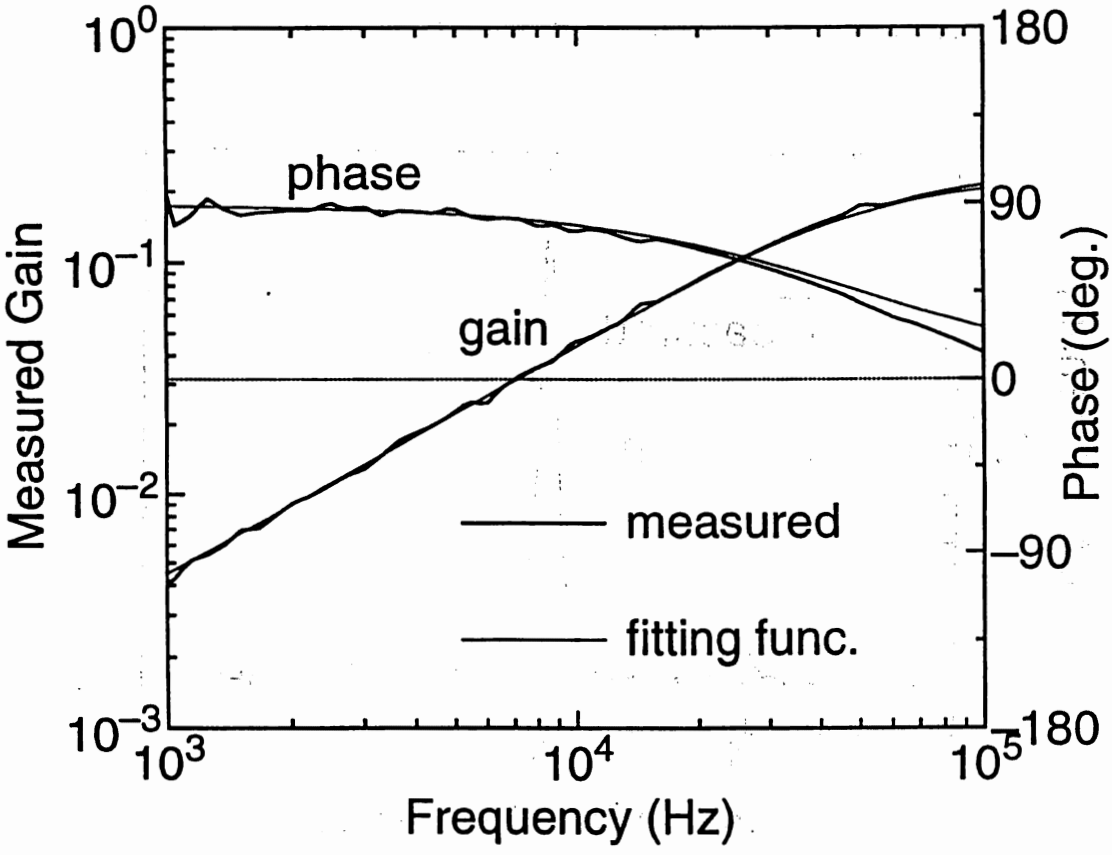

Fig.5.6 Frequency response curve of the cavity.

So we made another measurement to obtain loss of the mirror, which is relatively insensitive to precision of measurement: transmittance of the cavity. Apart from thermal problem due to loss of the mirror, we are finally interested not in low loss of the mirror but in high transmittance of the cavity of Mode Cleaner. Assuming quality (reflectivity, transmittance, and loss) of each mirror which comprise cavity is the same, transmittance of the cavity can be expressed using loss of the mirror a^2 $(=1-r^2-t^2)$,

$$T_{\rm cav} = \left(1 - \frac{a^2}{1-r^2}\right)^2 \simeq \left(1 - \frac{\mathcal{F}}{\pi}a^2\right)^2, \tag{5.2}$$

where $T_{\rm cav}$ is the transmittance of the cavity for the matched light, and high reflectivity, $r^2 \simeq 1$, is assumed.

Figure 5.8 shows our measurement. Incident power and transmitted power outside the vacuum chamber were 10.4mW and 8.7mW, respectively. While, contrast of reflected light indicates matching ratio (ratio of matched mode ($\rm TEM_{00}$) to total power) of 94.7%, and transmittance of windows of vacuum chamber was 97%. From these value we obtained transmittance of the cavity and loss of the mirror as,

$$\begin{aligned} T_{\rm cav} &= 0.91 \\ a^2 &= 9.6 \times 10^{-5} \\ &\simeq 100\text{ppm} \end{aligned} \tag{5.3}$$

Although obtained loss was lower than that of one made by Electron Beam Deposit method ($\sim$ 300ppm), it was rather worse than typical one made by Ion Beam Spattering method ($\lesssim$ 50ppm). It is, however, good enough for our experiment considering lower transmittance of other optical components.

As obtained loss corresponds to contrast of 99.8% for matched mode, obtained rather worse contrast may be due to mismathed light or difference of quality of each mirror.

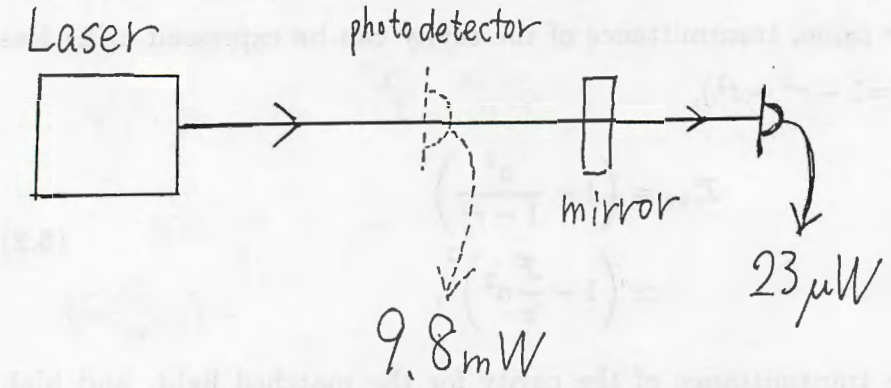

Fig.5.7 Measurement of transmittance of a mirror

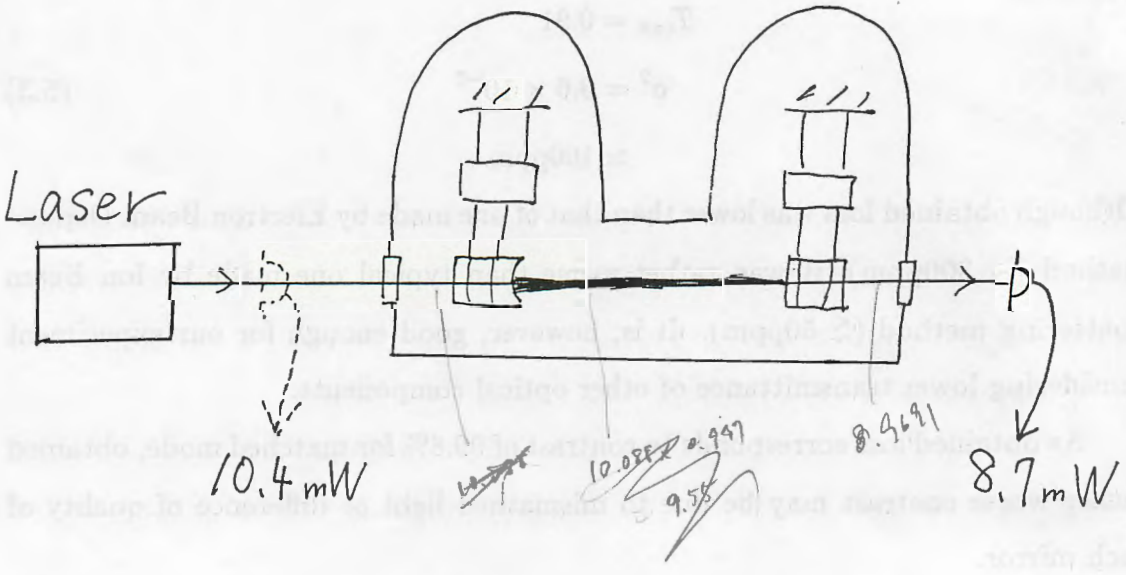

Fig.5.8 Measurement of transmittance of the cavity

5.1.2 Suspension of the Mirror

One of the most significant factors for the interferometric gravitational wave detectors is how to suspend mirrors. To suspend mirrors keeps them free for the gravitational waves at higher frequencies than the resonance of the suspension. Moreover it works as a vibration isolation system for the external seismic or acoustic noise. In practice, mechanical resonance of the suspension system produces excess noise to the mirror, and thermal noise of the suspension system and that of mirror mass itself degrade sensitivity of the interferometer.

Considering these conditions, we designed a suspension sytem (Fig.5.9) as follows.

· ***Double Pendulum Suspension***

Vibration isolation ratio for n-stage suspension sytem without damping, above its resonant frequencies, can be roughly expressed as,

$$\frac{x_{\text{lowest mass}}}{x_{\text{supension point}}} \propto \left(\frac{f_0}{f}\right)^{2n} \tag{5.4}$$

where x's denote displacement, and f_0 and f are typical resonant frequency of suspension and a frequency of vibration, respectively. From (5.4), multi-stage system is necessary in order to realize high isolation ratio [20, 21]. We applied 2-stage suspension: upper mass is made of aluminum and lower mass is fused silica rod with a mirror (Fig.5.2). For controlling mirror by coil and magnet actuators, two magnets, diameter of 2mm and length of 10mm, are attached on the surface of the rod opposite to the mirror.

· ***Eddy Current Damping***

In order to suppress large pendulum motion at resonant frequencies, we adopted eddy current damping system [22] applied on the upper mass. As the damping force produced between 8 strong Nd magnets and aluminum mass is large enough, we needed not use any active damping system using position sensors

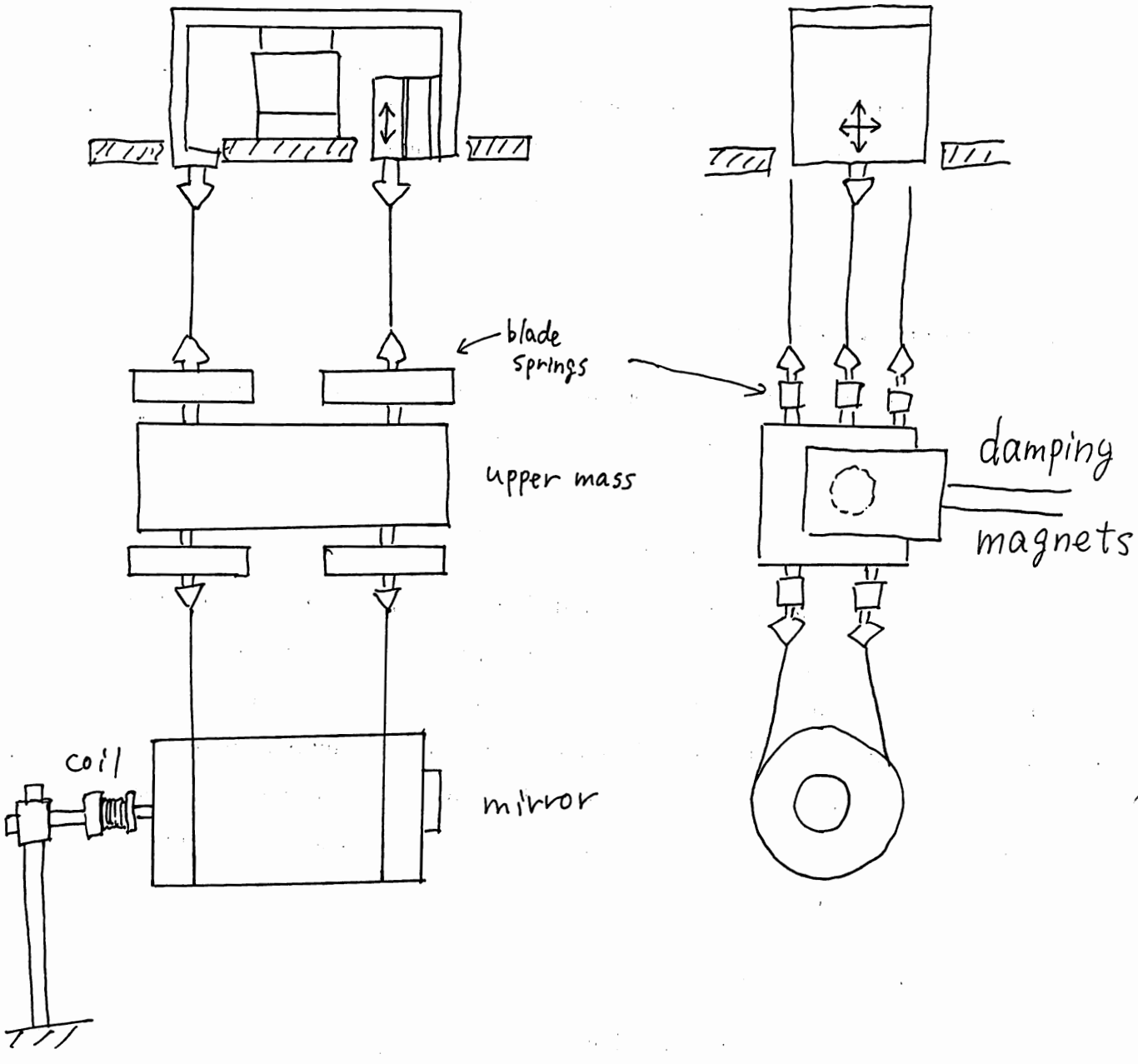

Fig.5.9 Suspension system used for Mode Cleaner.

etc. Using eddy current damping simplified our 2-stage suspension system. Since two fundamental pendulum modes couple the both mass, damping force was applied only the uppper mass, which also simplified the system and reduces thermal noise of lower mass.

· ***Vertical Vibration Isolation System***

Vertical vibration ordinary couples horizontal motion which causes excess noise [21]. In order to isolate vertical vibration, rectangular blade springs were inserted at suspension point of the upper mass (Fig.5.10), resulting in 2-stage vertical isolation. Spring is made of phosphorus bronze which has no magnetism and can be used in vacuum. Figure 5.11 shows the noise spectrum with or without vertical isolation obtained from the error singal of Mode Cleaner (see Fig.5.1). Below 100Hz, vertical vibration apparantly couples to horizontal motion and is reduced about 50dB by blade springs. Noise floor in Fig.5.11 is limited by frequency noise of the laser.

· ***Alignment Control using Motor Drive and PZT***

Since suspension system is housed in the vacuum chamber, alignment should be controlled from outside the chamber. For simplicity, alignment control was realized by controlling position of suspension point of the pendulum. Upper mass is suspended by three wires; two are fixed on suspension frame, and one is fixed on the x-z stage. By controlling suspension point of 'one wire' x or y direction, yaw or pitch of the mirror can be controlled (Fig.5.12). Motorized drives were used for coarse control ($\gtrsim 1\mu$m), while PZT (piezo-electric transducer) acturators were used for fine control ($\lesssim 10\mu$m). We used PZTs with coefficient of 10μm/100V which corresponds to tilt of 1μrad/V for our mirror with 10cm long.

In addition, coil support, mirror stopper in case of break of suspension wire and wiring etc.are included as suspension system. All the components are made of materials durable in vacuum and with low outgas (aluminum, stainless steel, Teflon etc.).

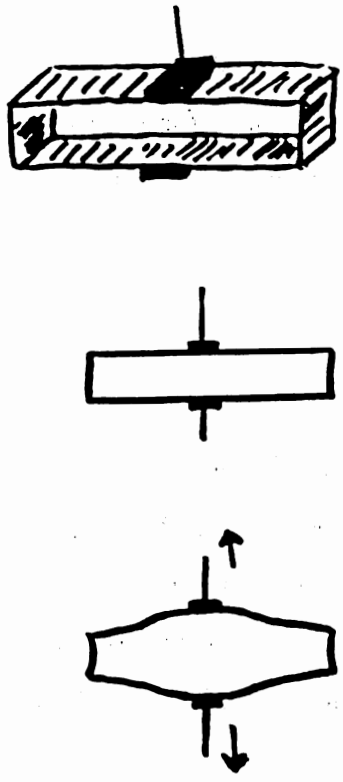

Fig.5.10 Blade spring for vertical vibration isolation.

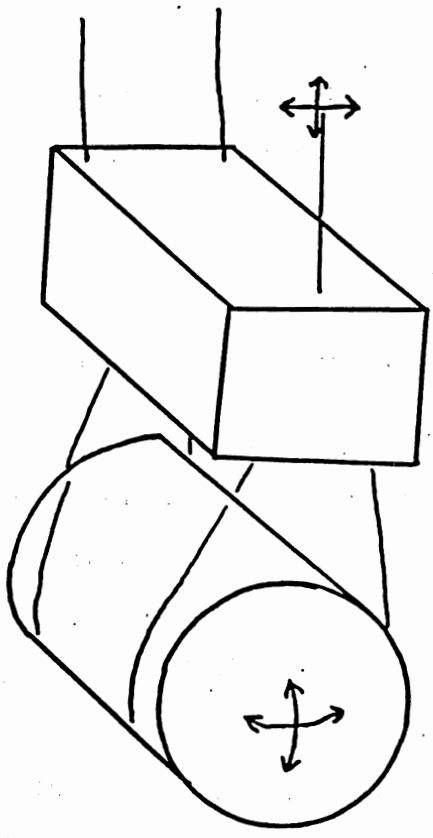

Fig.5.12 Alignment control by suspension point.

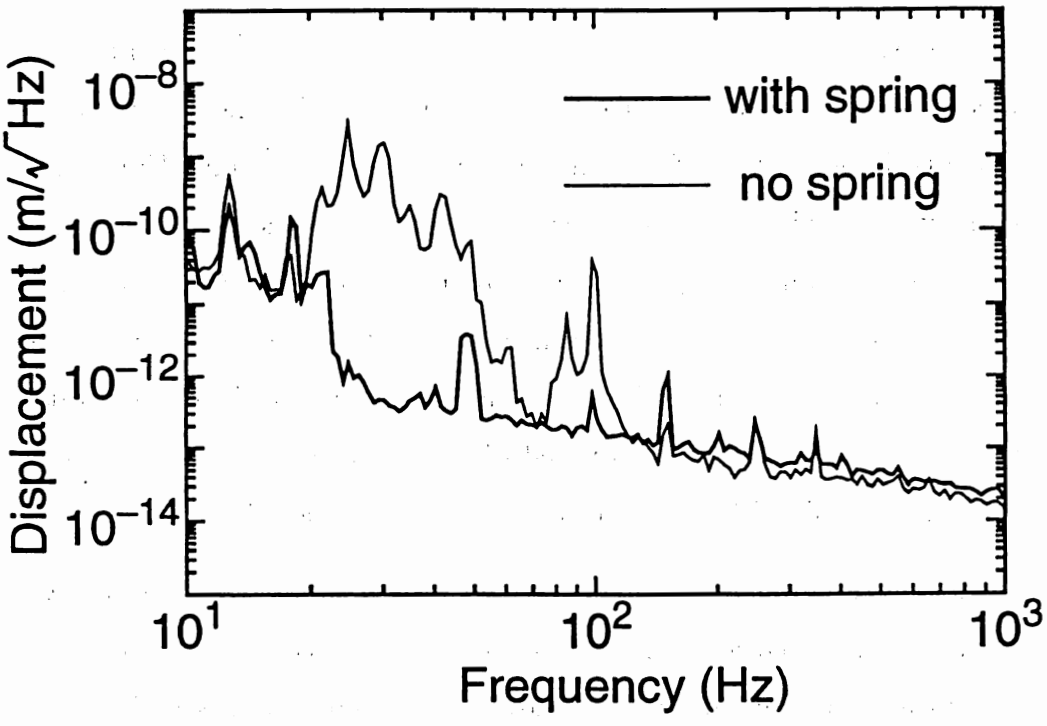

Fig.5.11 Error signal of Mode Cleaner with or without blade springs.

In order to estimate suspension performance, we measured transfer function of the pendulum using photosensor as position sensor (Fig.5.13). The obtained transfer fuction (Fig.5.14) shows quality factor of upper mass damping of $Q = 0.5$. Using this quality factor, vibration isolation ratio can be calculated as,

$$\frac{x_{\text{mirror}}}{x_{\text{suspension point}}} =$$

$$\frac{\omega_2^2\left[(1+\alpha)\omega_1 + \mathrm{i}(\omega_1/Q)\omega\right]}{\omega^4 - \mathrm{i}(\omega_1/Q)\omega^3 - (1+\alpha)(\omega_1^2+\omega_2^2)\omega^2 + \mathrm{i}(\omega_1\omega_2^2/Q)\omega + (1+\alpha)\omega_1^2\omega_2^2}, \quad (5.5)$$

where

$$\alpha = \frac{m_2}{m_1}, \quad \omega_{1,\,2} = \sqrt{\frac{g}{\ell_{1,\,2}}}$$

Subscript 1 and 2 denotes upper and lower mass; m, g, and ℓ mean mass, gravity acceleration, and length of wire, respectively. Calculated isolation ratio is shown in Fig.5.15.

5.1.3 Vacuum Chamber

Mode cleaner cavity is housed in the vacuum chamber in order to avoid acoustic noise and fluctuation of refractive index of air. Figure 5.16 shows the shape of the chamber: each mirror with suspension system is located in each chamber of 500mm-diameter and 600mm-tall separated by 1m. Each chamber is made of stainless steel and is connencted with 6-inch pipe. Incident beam illuminates cavity through the anti-reflection optical window. Transmitted light from the cavity is led into main 20m vacuum chamber through the quick-coupling vacuum pipe; mode cleaner can be evacuated isolately when transmitted port is closed.

When the chamber was empty and isolately evacuated with turbo molecular pump (300ℓ/s), pressure of 1×10^{-4}Pa was attained. In operation including suspension system, vacuum was degraded to 4×10^{-4}Pa. It is, however, enough for our experiment.

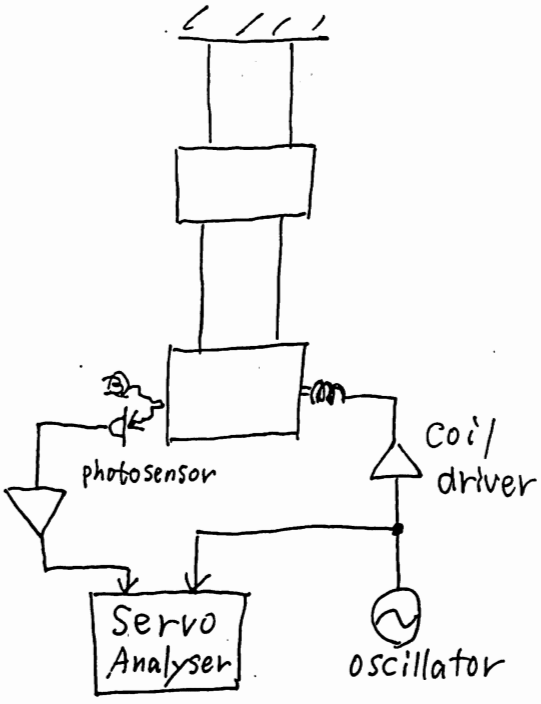

Fig.5.13 Measurement of transfer function of the pendulum.

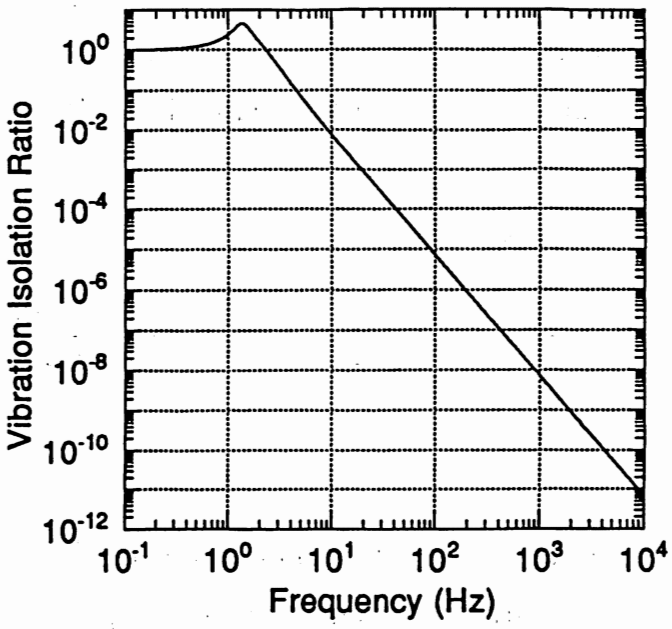

Fig.5.15 Calculated vibration isolation ratio of the pendulum.

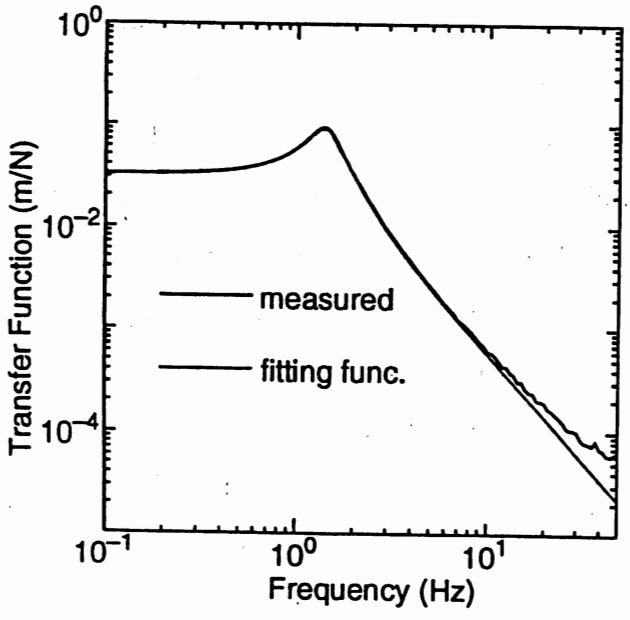

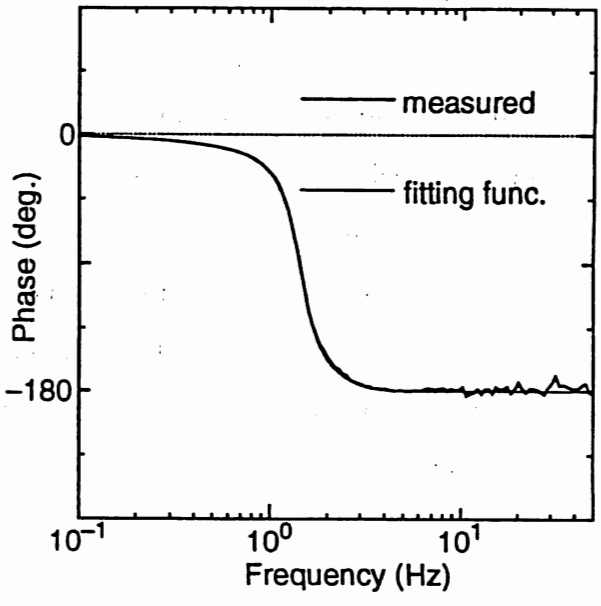

Fig.5.14 Transfer function of the 2-stage pendulum.

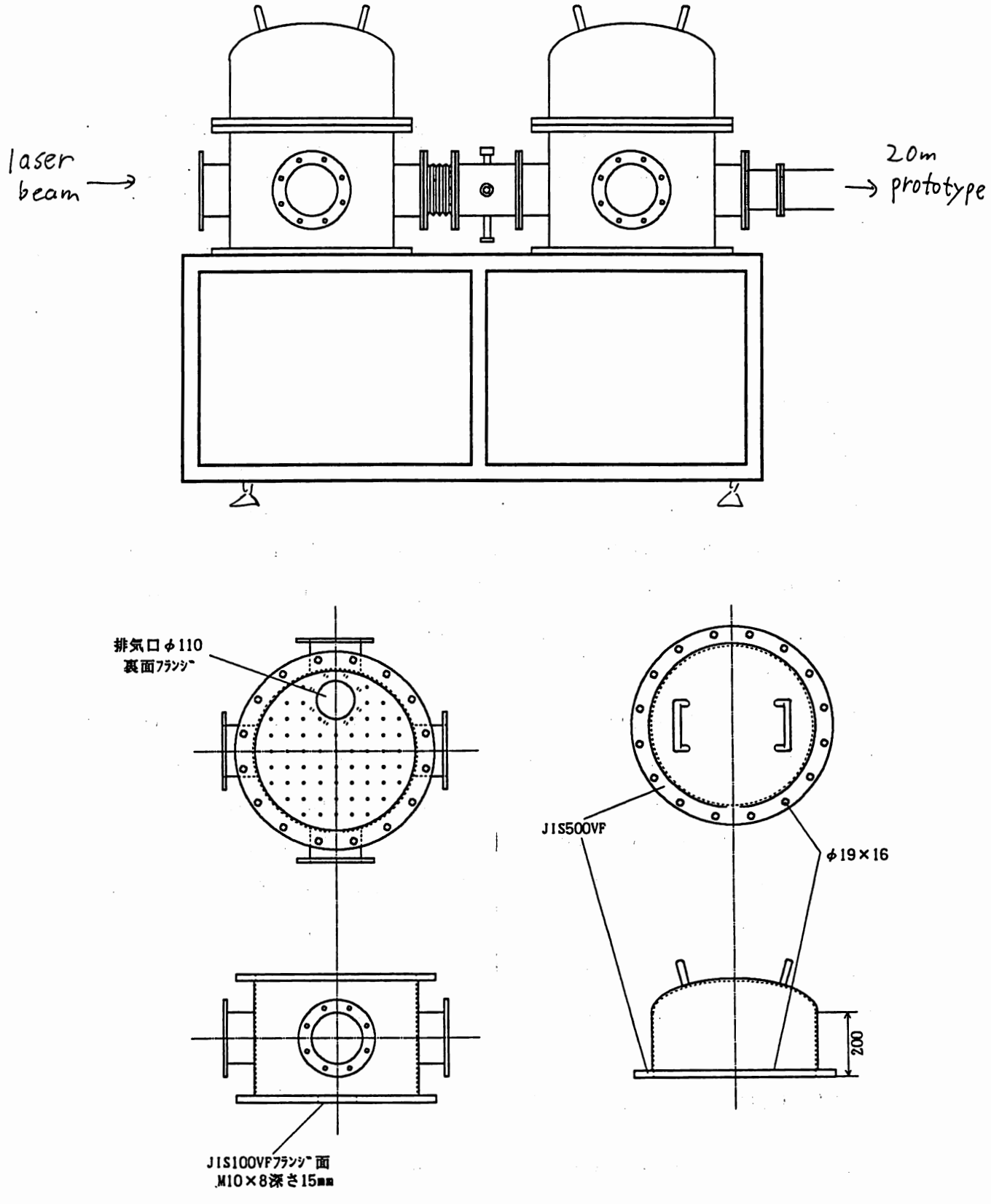

Fig.5.16 Vacuum chamber for Mode Cleaner

	波長	パワー	偏光	ビーム拡がり角	PZT 感度
nominal	1.064μm	560mW	垂直	5.5mrad(垂直)、7.5mrad (水平)	≳2MHz/V
measured		530 ~500 mW		4.6mrad 6.0mrad	6.5MHz/V

Table 5.1 Specifications of MISER

5.1.4 Laser

We used a Laser Diode pumped Nd:YAG laser as a light source because of its low noise performance and feasibility of high power laser in future. Moreover, commercially available one we used (MISER, Model:122-1064-500-F, λ=1064nm, 500mW, LIGHTWAVE Co.,Ltd.) has relatively stable configuration, monolithic non-planar ring resonator which is thermally controlled, and is tunable in frequency by PZT attached on the resonator.

We measured several performance of the laser: output power, beam geometry, and the index between input on PZT and frequency shift.

Output power was measured by a power meter (SCIENTECH Co.,Ltd.). Initially it was 0.53W but it gradually decreased over several months down to 0.50W. Beam geometry (see Section 5.1.7 in detail) and PZT index (frequency response was measured as Fig.5.17 and 5.18) as well as measured power are shown in Table 5.1, accompanied with nominal specification. Other performance, intensity noise, frequency noise, and beam jitter are described in Chapter 6.

5.1.5 EOM (Phase Modulator)

In order to lock the Fabry-Perot on resonance, incident light is modulated in phase, and reflected light is detected and demodulated to obtain signal. Modulation frequency should be chosen at the frequency where intensity noise is below

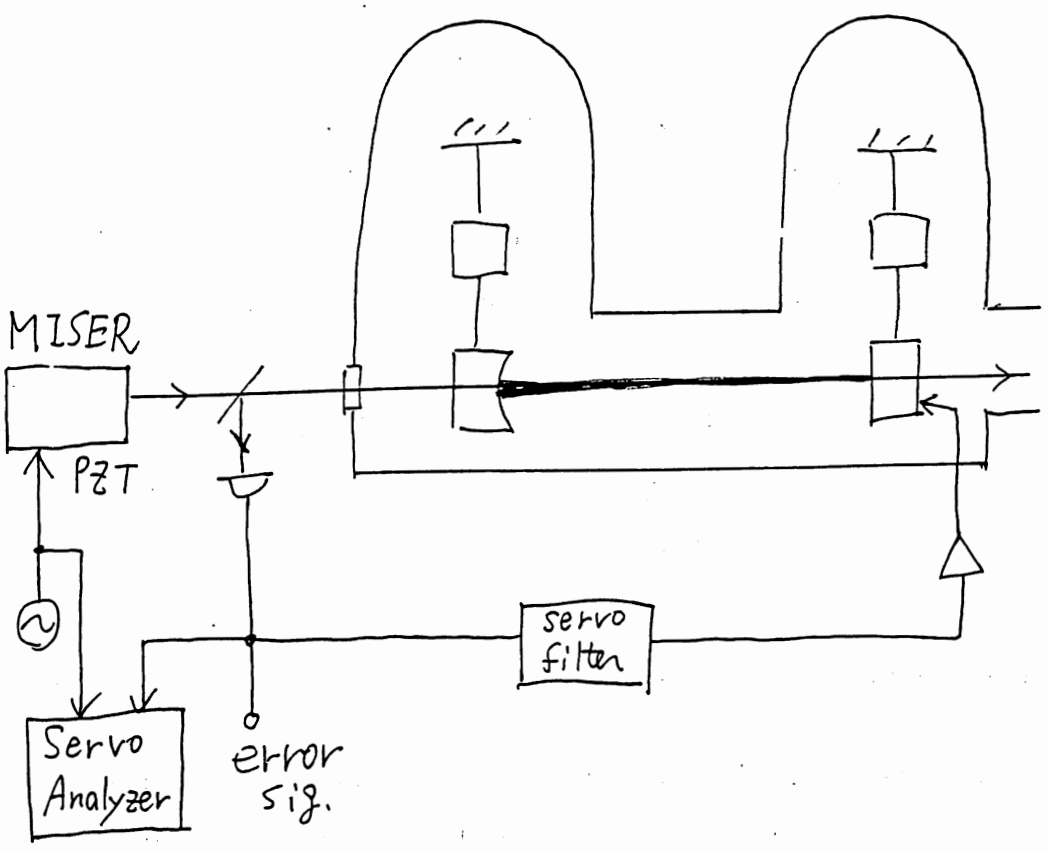

Fig.5.17 Measurement of frequency response of PZT

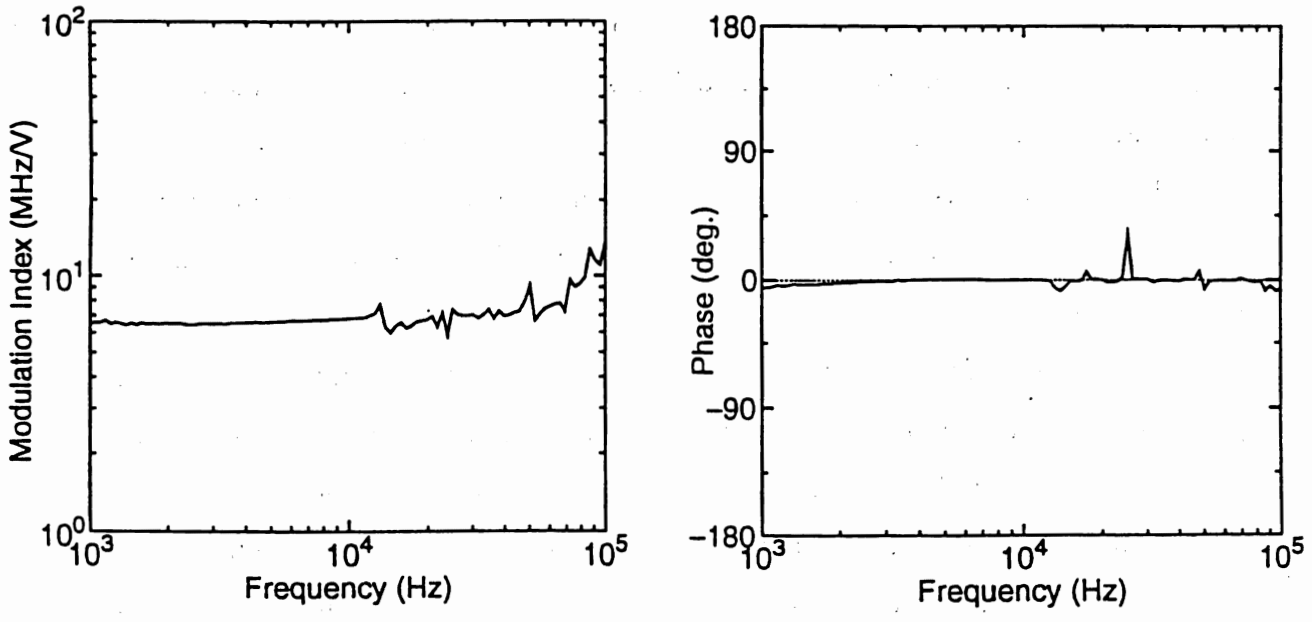

Fig.5.18 Frequency response of PZT

shot noise level of the light, which is higher than 10MHz considering intensity noise performance of MISER [23]. Phase modulation at such RF band is realized by Electo Optic Modulator (EOM). We decided modulation frequency of 18MHz and used a resonant type EOM (Model 4003, NewFocus Co.,Ltd.) which applies both a crystal with a lage electo-optic index and a resonant circuit to reduce input voltage.

By measuring ratio of sideband peak (V_s) to carrier peak (V_c), we obtained modulation index by measurement similar to Fig.5.3 as shown in Fig.5.19. Other specifications are shown in Table 5.2.

5.1.6 Detector and Demodulator

Reflected light from the cavity is modulated in amplitude which is detected and demodulated to obtain signal (Fig.5.1). Output of the detector is demodulated with a passive Double Balanced Mixer (DBM) by mixing with properly phase shifted reference oscillator. Mixed output of DBM is obtained as a signal after removing second harmonics of modulation frequency.

The detector should have low noise performance because it directly limits the frequency stabilization. By applying LC tank circuit resonant at the modulation frequency (Fig.5.20, 5.21), we could make a low noise detector [24]. By measuring demodulated noise as a fuction of photocurrent, equivalent noise photocurrent, I_{det}=0.1mA (Fig 5.22) which is well below the residual detected light ($I_{dc} \simeq$ 2mA), was obtained.

One problem of the detector is its saturation power. Although we used InGaAs photodiode (diameter of 1mm) to increase quantum efficiency, it has saturation power of about 10mW. Ideally reflected light falls down completely dark, but due to mismatching or low quality of cavity mirrors some light is reflected; in our case several milli-watts was reflected. We avoided saturation of detector by attenuating the detected light when cavity was off-resonant and increasing the light after resonance. However, considering the future high power laser, development of

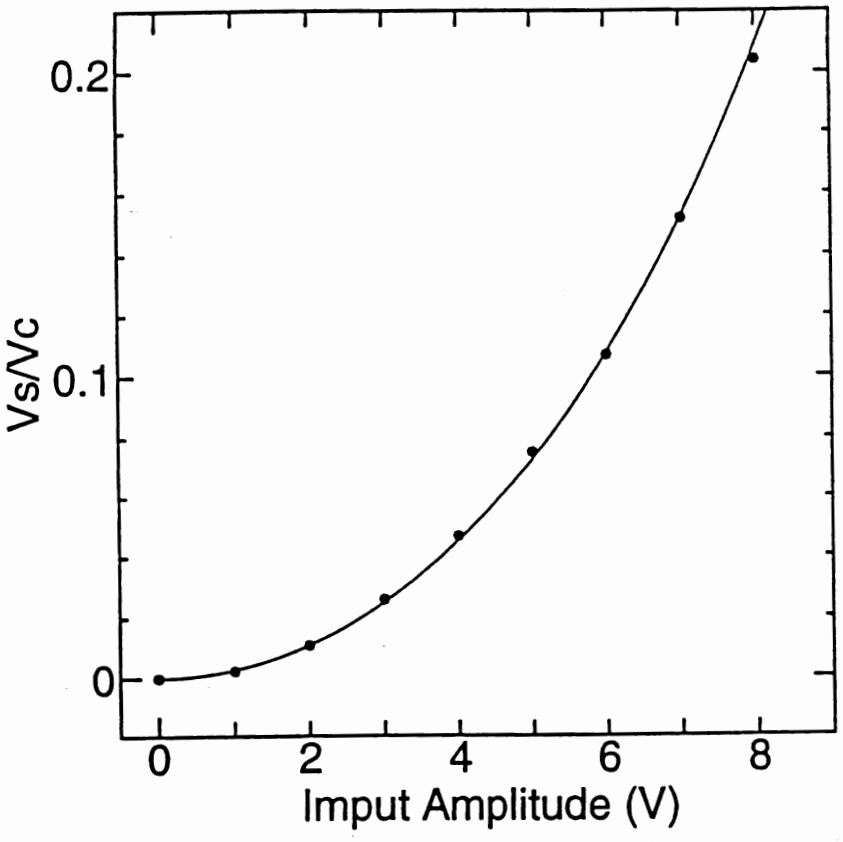

Fig.5.19 Modulation performance of EOM

	波長域	バンド幅	材料	アパーチャー	変調感度	最大入力
nominal	1.0-1.06μm	1-2%freq.	$LiTaO_3$	2mm	0.2rad/V 以上	16V
meas.					0.21rad/V	

Table 5.2 Specifications of EOM

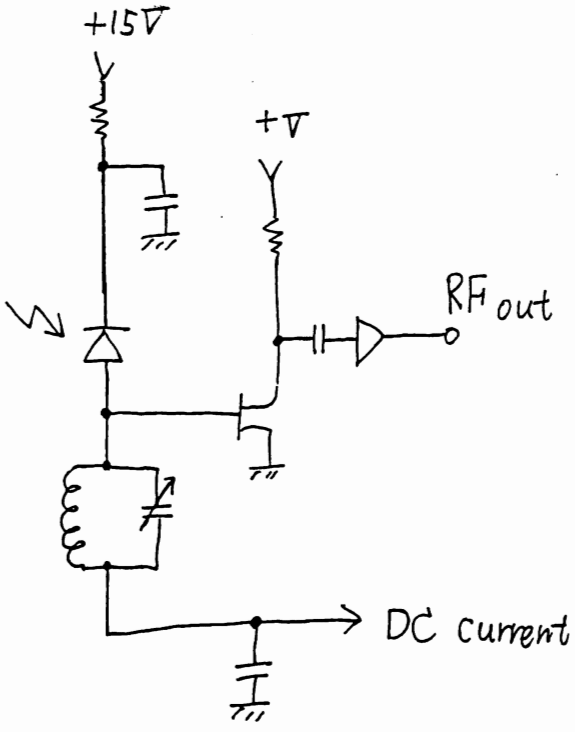

Fig.5.20 LC tank circuit of photodetector.

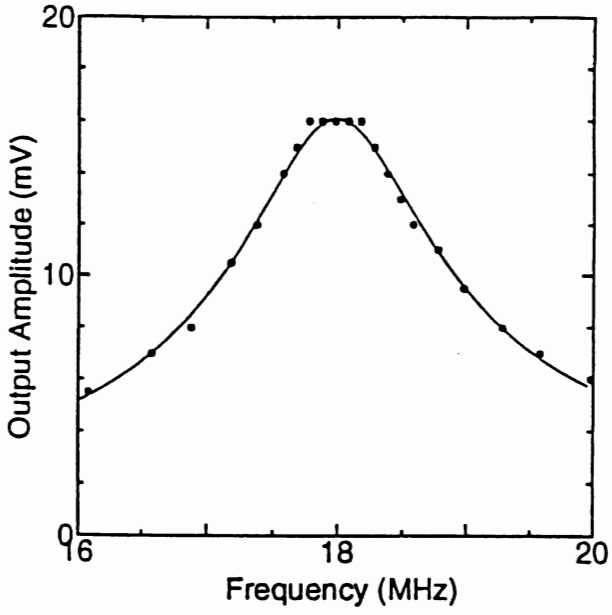

Fig.5.21 Resonance curve of the detector.

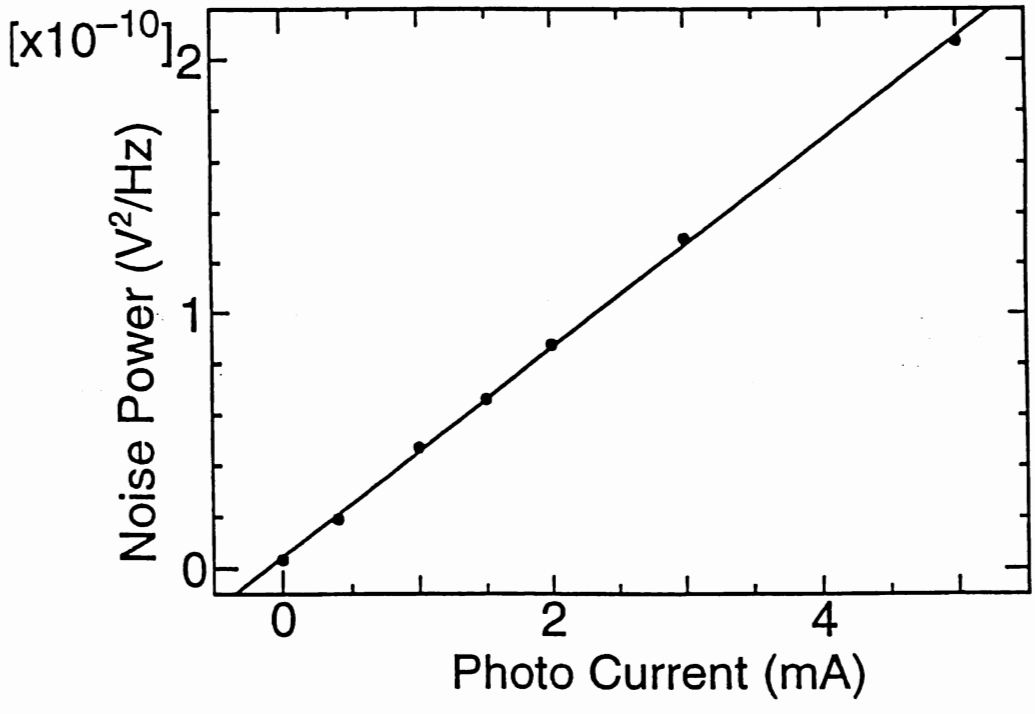

Fig.5.22 Noise performance of the detector.

a multi-devided detector [25] or a large surface photodiode would be necessary as well as efforts of reducing mismatching and a high quality cavity.

§5.2 Optical Design

Optical configuration was designed so as to match the laser beam to the Fabry-Perot cavity, because high matching ratio leads to low reflected light and high transmittance of the cavity.

First, we measured the beam geometry of the MISER. Since laser cavity of the MISER is a ring cavity, output beam shape is elliptical; its principal axes are directed to horizontal and vertical. Hence we measured both vertical and horizontal beam diameter using a knife edge beam profiler as a fuction of distance of the laser (Fig.5.23 'raw beam'). The measured beam waist radius and position (subscript x and y denote horizontal and vertical, respectively),

$$\begin{aligned} w_{x0} &= 111\mu\text{m}, \quad z_{x0} = -52\text{mm} \\ w_{y0} &= 145\mu\text{m}, \quad z_{y0} = -54\text{mm}, \end{aligned}$$

which corresponds to divergence angle of

$$\theta_{x0} = 6.0\text{mrad}, \quad \theta_{y0} = 4.6\text{mrad}.$$

They agree with nominal value (Section 5.1.4). In order to realize high matching ratio, beam geometry should be converted from elliptical shape to round shape. Two cylindrical lenses positioned as Fig.5.24 made it possible to convert shapes. Measured and fitted beam profile are shown in Fig.5.23.

Next, in designing mode matching lenses, demands for beam diameter to insert optical devices with small aperture and compatibility of their position with an optical table and a vacuum chamber were considered. Reasonable optical path length in the laboratory was another factor to be considered.

We designed optical configuration as Fig.5.25 using two lenses except for cylindrical ones. Due to limitation of laboratory space, incident beam was forced to

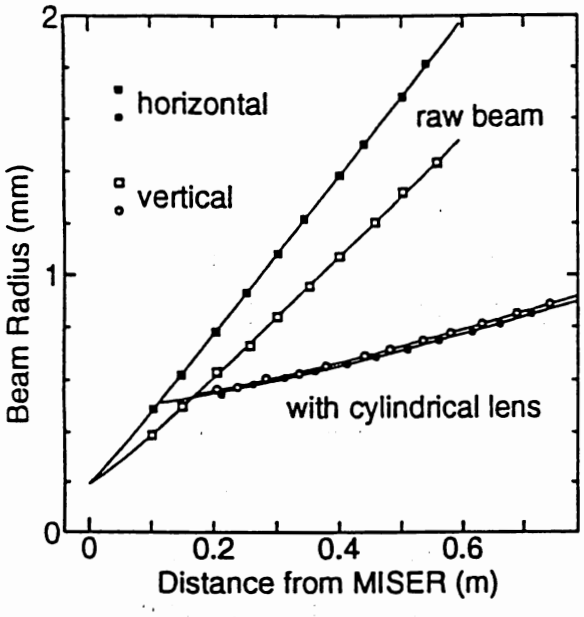

Fig.5.23 Beam profile with or without cylindrical lenses.

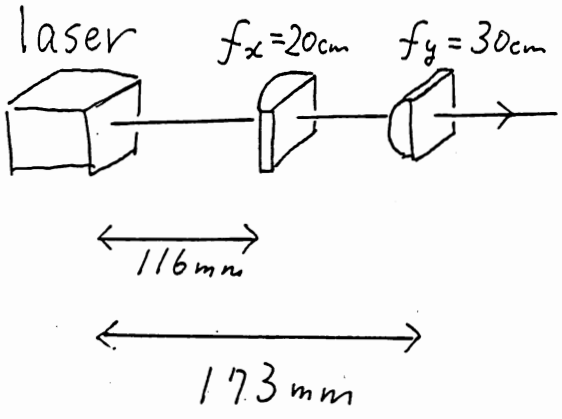

Fig.5.24 Position of two cylindrical lenses.

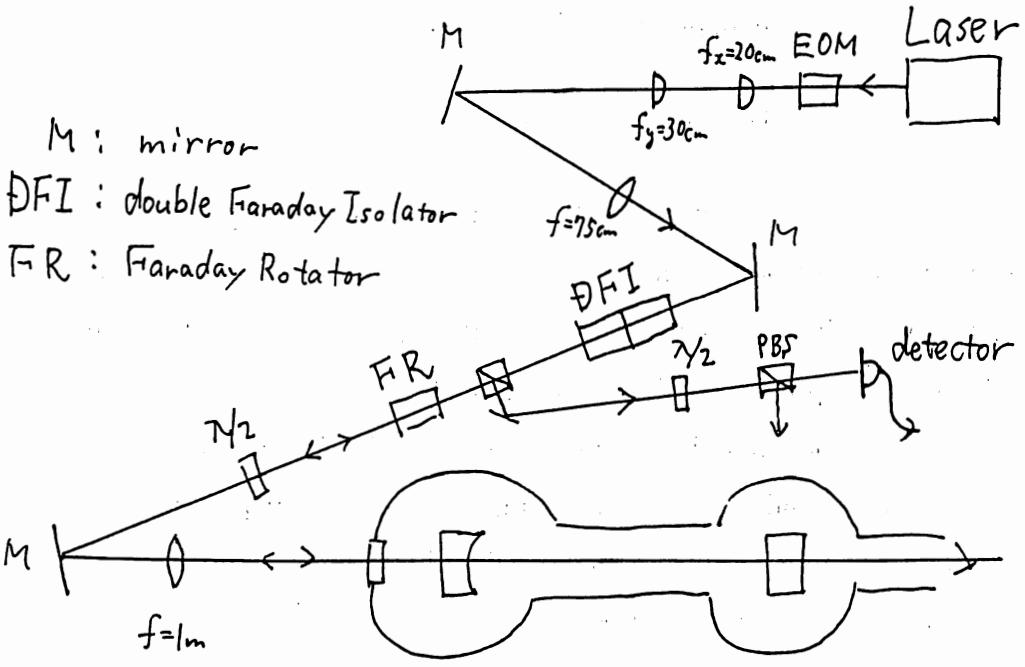

Fig.5.25 Optical design for Mode Cleaner.

steer by the mirror mounted on an unstable table and optical path length had to be made large to lead beam. Optical isolator and EOM, which have aperture diameter of 2mm, was inserted near beam waist whose beam diameter is about 1mm. All optical components are treated with anti-reflection coat. Polarization of the beam was designed vertical and optics were arranged at the same level to avoid polarization change in the reflection by the steering mirrors. Reflected light from the cavity was extracted by the combination of Polarizing Beam Splitter (PBS) and Faraday Rotator (FR). Detecting power was controlled by rotating Half Wavelength Plate (HWP), to avoid saturation of the detector (Section 5.1.6).

Due to power loss of the optical components, power of incident beam to the cavity diminished from 500mW at laser down to 240mW. Major loss was a 2-stage optical isolator (transmittance of 70%). Resulting transmitted power from the cavity was about 200mW.

§5.3 Servo Design

We designed two servo systems. One is Cavity Lock Servo to lock the Fabry-Perot cavity referred to the laser, which is used either to measure performance of the components or to compare free running noise level with frequency-stabilized one. The other is Frequency Stabilizing Servo which stabilizes laser referred to Fabry-Perot cavity, especially stabilizes near 1kHz. The block diagram of both servo is shown in Fig.5.26.

The theoretical Bode diagram of Cavity Lock Servo is shown as thin line in Fig.5.27. In order to keep stable locking at low frequencies, time constant is changed after locking from dashed line to solid line (conditionally stable servo), which has unity gain frequency of 1kHz and phase margin of 15degree. It was in good agreement with the measured transfer function. By using this servo we measured response function of the Fabry-Perot cavity (Section 5.1.1) and PZT of MISER (Section 5.1.4).

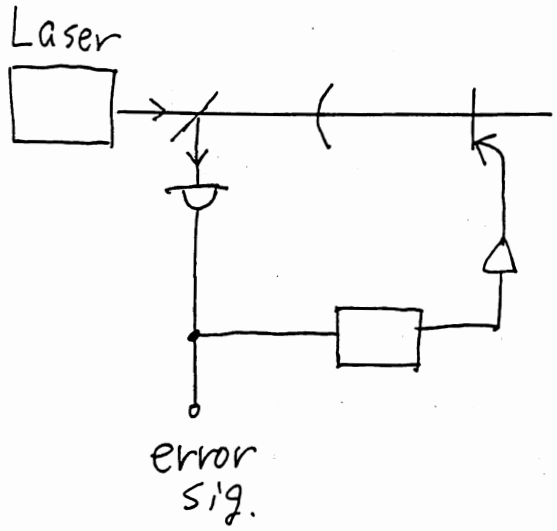

Fig.5.26(a) Cavity Lock Servo.

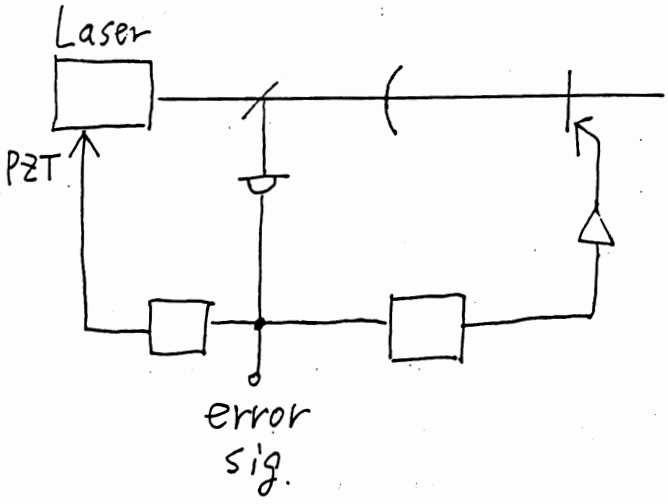

Fig.5.26(b) Frequency Stabilizing Servo.

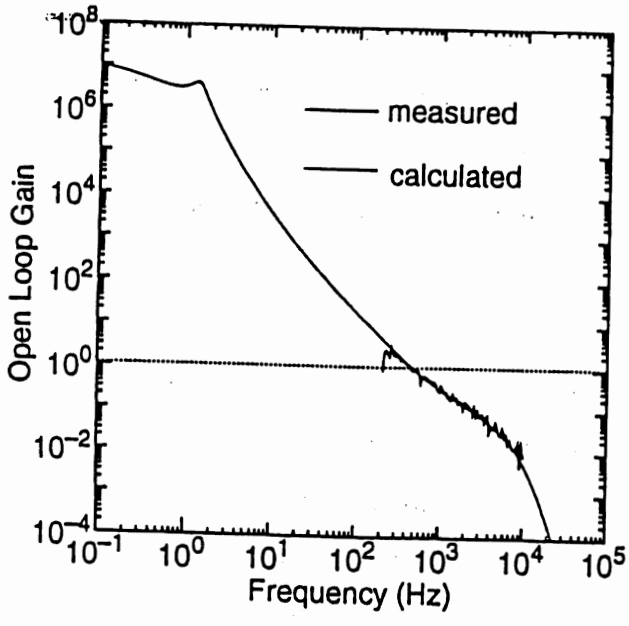

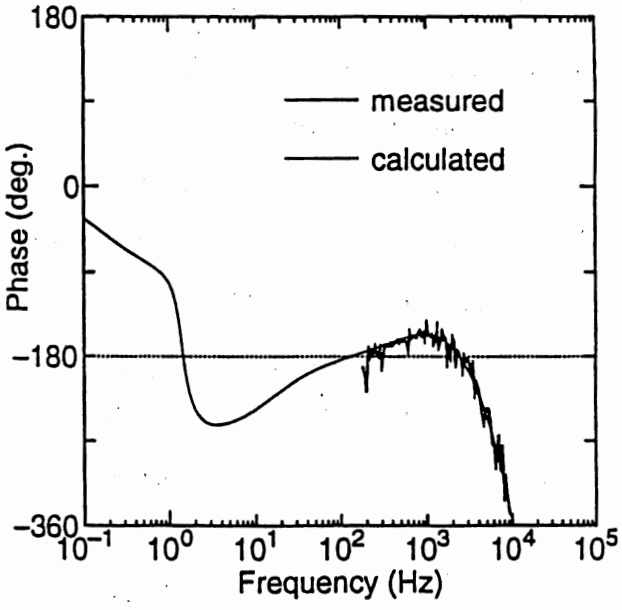

Fig.5.27 Bode diagram of Cavity Lock Servo.

Frequecy Stabilizing Servo contains two loops; signal at low frequencies is fed back to the cavity, while at higher frequencies laser frequency is locked to the cavity. Because of the unstability of the cavity length due to pendulum motion excited by seismic noise, such cavity lock loop at low frequencies is necessary.

Cross over frequency of these loops was decided to be about 30Hz considering the cavity stability obtained from the spectrum with Cavity Lock Servo, which indicated that cavity vibration was dominant below 30Hz while frequency noise dominated above 30Hz (Fig.6 in Section 6). Low cross over frequency causes frequency stabilization referred to unstable reference, whereas higher cross over frequency limits the frequency stabilization gain; we decided 30Hz as trade-off.

Figure 5.28 shows calculated transfer function of the two loops: Pendulum Loop to lock Fabry-Perot and PZT Loop for frequency stabilization. Phase margin was about 25deg at a unity gain frequency of about 20kHz which was limited by PZT resonance about 100kHz. From the calculation using servo diagram in Fig.5.29, stabilized frequency noise is expressed as

$$n_{\text{FM stabilized}} = \frac{1+F}{1+F+G} n_{\text{FM}}, \tag{5.6}$$

therefore about 80dB frequency stabilization would be realized at 1kHz. As Frequency Stabilization Servo was also designed conditionally stable to realize high loop gain near 1kHz, time constant was set initially as dashed line in Fig.5.28 and after locking it was changed to solid line with increasing loop gain by increasing detected light power using HWP (Section 5.1.6, 5.1.7).

Since two loops couple tightly, we cannot measure each transfer function independently. So we measured each loop transfer function when it was locked. Calculated and measured transfer functions are shown in Fig.5.30. In these measurements, the PZT loop transfer function expresses net stabilization gain peaking near 1kHz.

Long term stability of both servo systems seemed to have no problem. Without external vibration, the system kept locking longer than 3 hours as far as confirmed. On the long term stability, see Section 7.3.

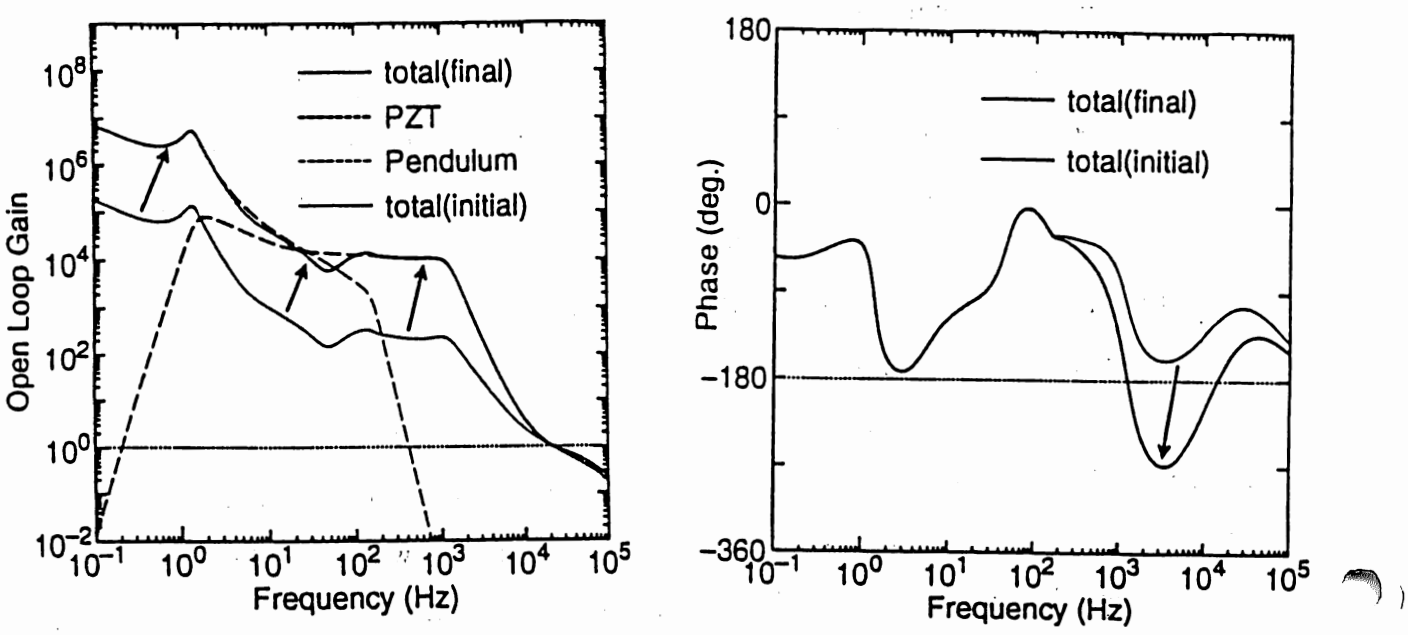

Fig.5.28 Calculated Bode diagram of Frequency Stabilizing Servo.

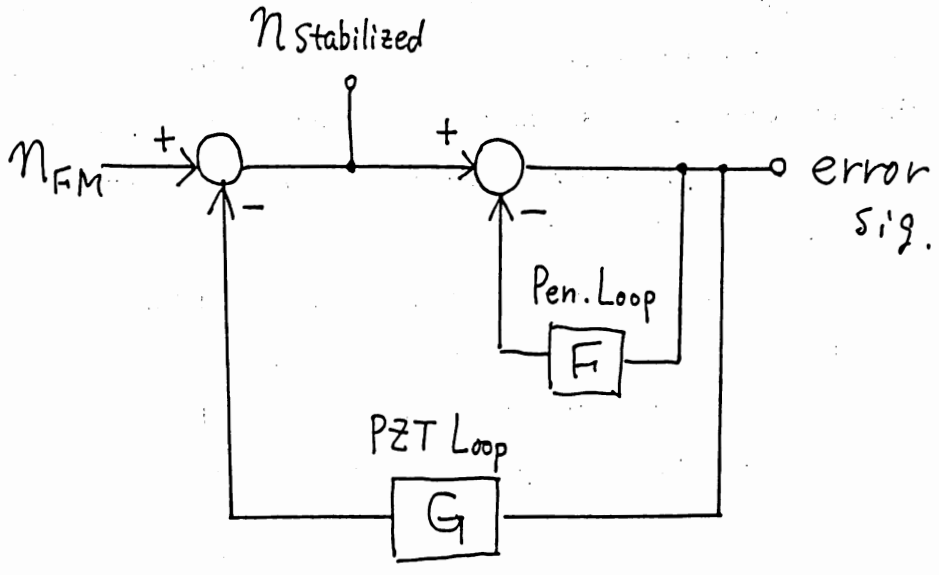

Fig.5.29 Block diagram of Frequecy Stabilizing Servo.

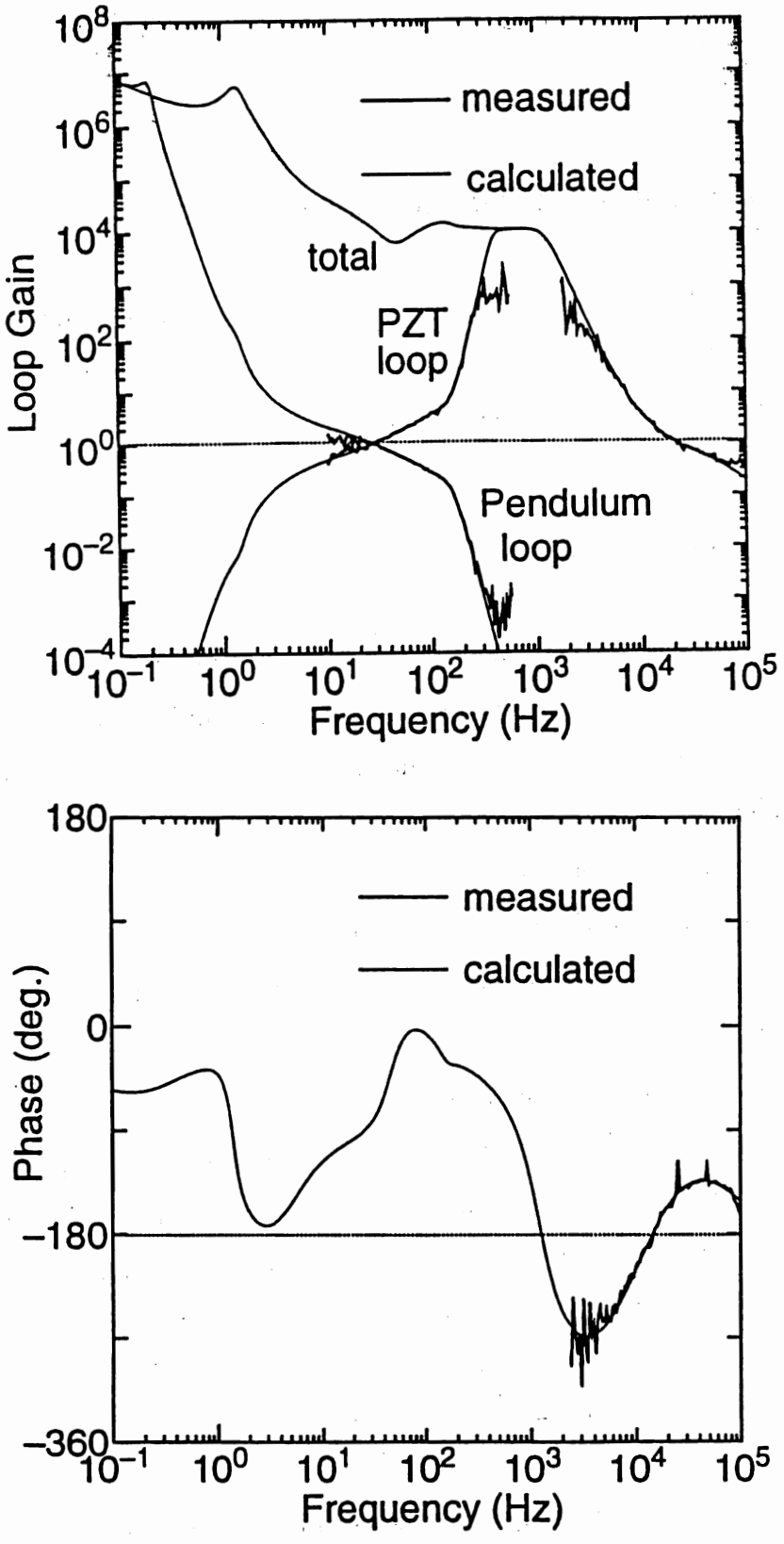

Fig.5.30 Loop transfer function of Frequency Stabilizing Servo

6. Performance of 1-meter Mode Cleaner

§ 6.1 Measurement of Beam Jitter

In order to estimate performance of Mode Cleaner as a mode selector, we measured beam jitter with or without Mode Cleaner. Other feature, improvement of contrast of prototype is described in Chapter 7.

6.1.1 Beam Jitter of Incident Beam

We measured beam jitter of the incident beam making use of one arm of 20m prototype as Fig.6.1. Optical component in the 20m chamber was the same condition as operation of prototype, except that Fabry-Perot cavity and beamsplitter were not installed. Angular fluctuation is enhanced by its arm length. Transmitted light from the end chamber was detected in position using a knife edge position sensor which blocks half of the light horizontally or vertically. Effect of intensity noise was cancelled out by subtracting output of position sensor with the intensity of sampled light.

Before measurement of beam jitter, beam diameter at the position sensor was measured. Figure 6.2 is the output of position sensor; knife edge was moved horizontally or vertically. Assuming elliptical gaussian distribution of intensity and its principal axes were directed to horizontal and vertical direction, the output of the sensor can be expressed as a function of displacement of the knife edge,

$$I(a) = \sqrt{\frac{2}{\pi w_0^2}} \int_{-\infty}^{a} \mathrm{e}^{-\frac{2a^2}{w_0^2}} \mathrm{d}a \tag{6.1}$$

where w_0 is beam radius and origin of a is assumed to be center of the beam. Solid curves in Fig.6.2 is fitted intensity variation assuming $w_x = 3.9 \times 10^3 \mu$m for horizontal and $w_y = 3.2 \times 10^3 \mu$m for vertical. Then, the position fluctation of the

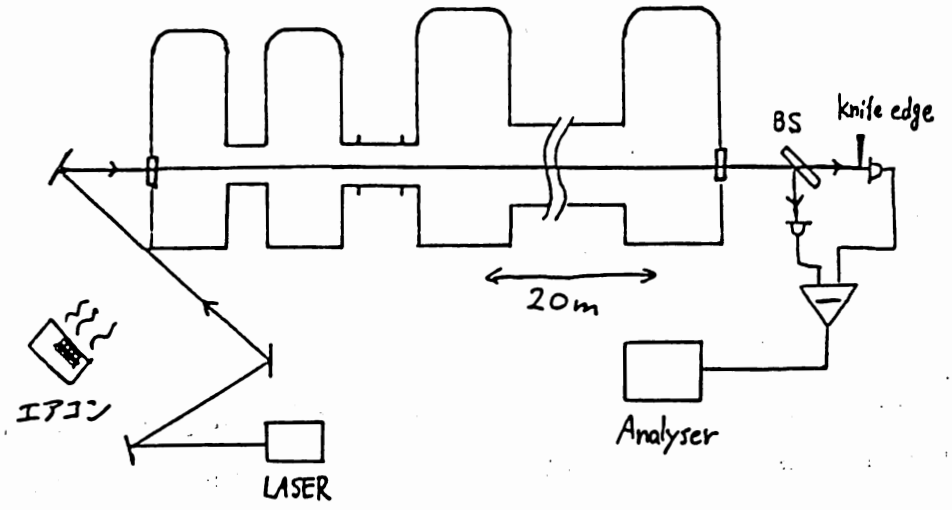

Fig.6.1 Measurement of beam jitter using one arm of 20m vacuum chamber.

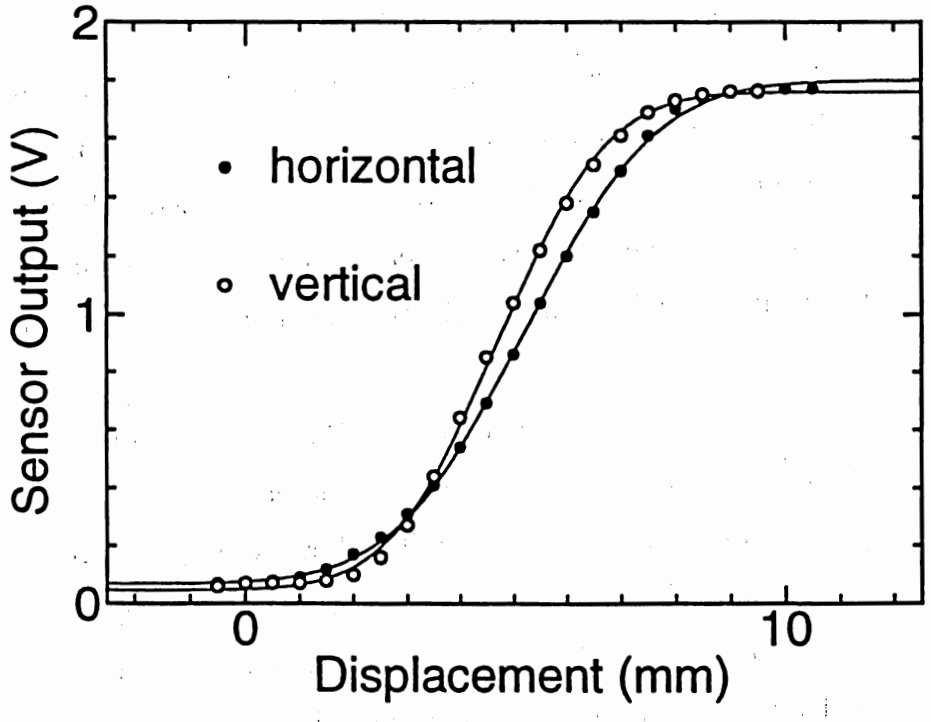

Fig.6.2 Beam radius measured by a knife edge position sensor.

beam can be expressed when the knife edge is located at the center of the beam,

$$\begin{aligned} \delta I &= \frac{\mathrm{d}}{\mathrm{d}a} I(a=0)\delta a \\ &= \sqrt{\frac{2}{\pi w_0^2}}\delta a \end{aligned} \tag{6.2}$$

Therefore corresponding beam jitter in angle is,

$$\delta\alpha = \frac{\delta a}{\ell}, \tag{6.3}$$

where ℓ=20m in our measurement.

Bold line and dashed line in Fig.6.3 are the horizontal beam jitter and noise level of the detection, respectively. Noise level was derived from the output without knife edge. Unfortunately, due to large path length between laser and the chamber, almost beam jitter originated from fluctuation of the air. When the air conditioner near the path was turned on, beam jitter at low frequencies incresed to thin line in Fig.6.3. Other noise sources in detecting beam jitter was mechanical vibration of the position sensor; it was hard to estimate the vibration level.

Although we are interested in beam jitter of MISER itself in the kHz frequency region, it seems very hard to estimate it quantitatively considering various noise mentioned above. In fact, such beam jitter was not detected in Fig.6.3. So we estimated total beam jitter including air fluctuation and confirmed reduction of such beam jitter by Mode Cleaner. Anyway, difference between thick curve and thin one is real beam jitter coming from air fluctuation, it must be reduced by Mode Cleaner.

Another beam jitter of our interest is a effect of PZT attached on the laser crystal. Control of resonant frequency by deforming the laser crystal may produce spurious beam jitter. By applying signal to the PZT as Fig.6.4, frequency response of beam jitter was measured (Fig.6.5). At low frequencies, effect of beam jitter could not be measured due to external noise, e.g.air fluctuation. Applying voltage on PZT also caused intensity change, but comparing dashed line which is the output without knife edge such effect was negligible in this measurement. Figure

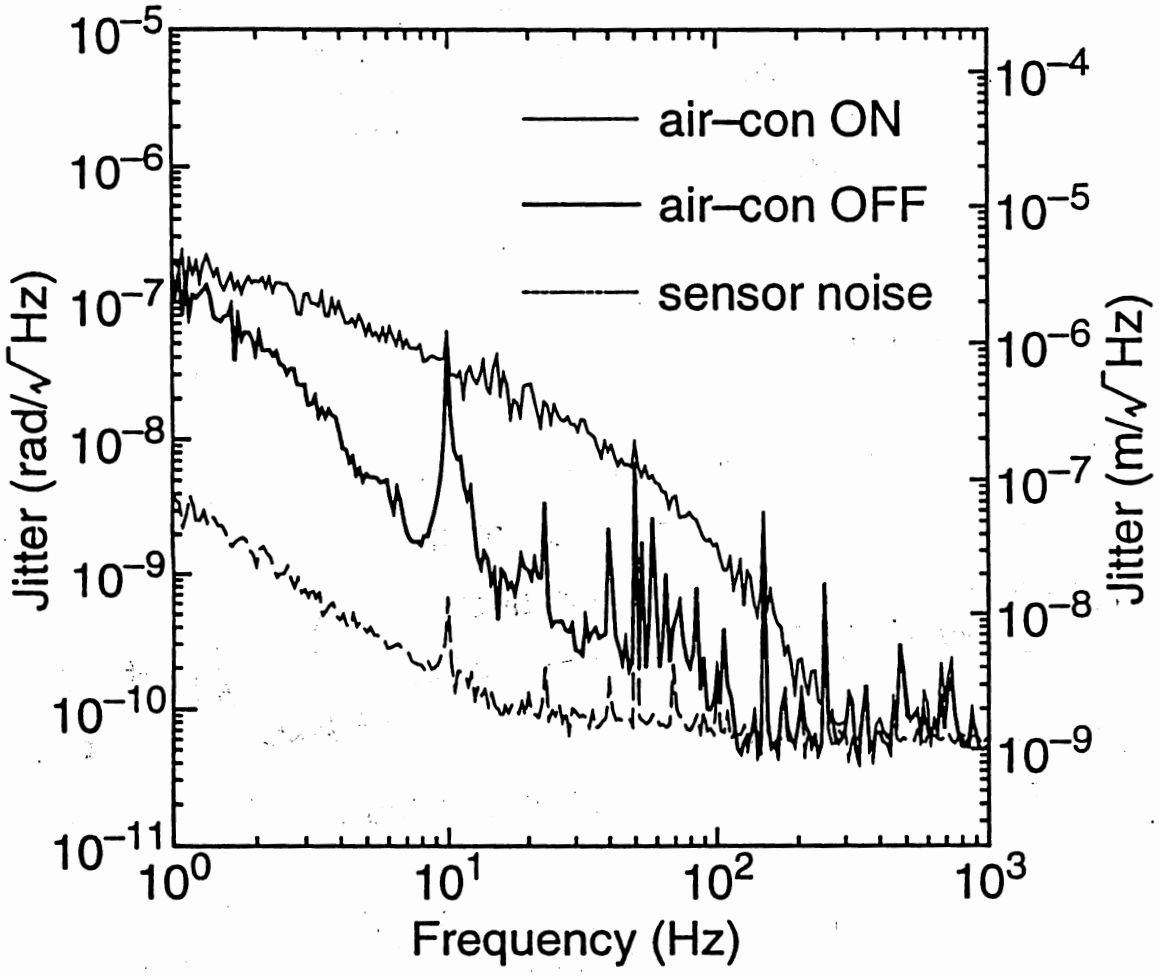

Fig.6.3 Beam jitter of incident beam.

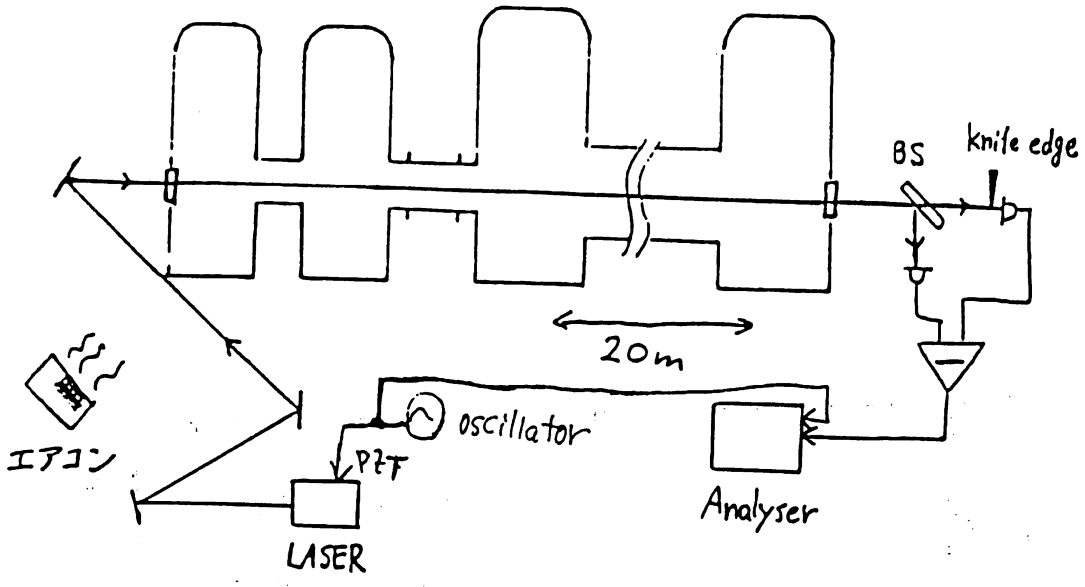

Fig.6.4 Measurement of beam jitter caused by PZT of MISER.

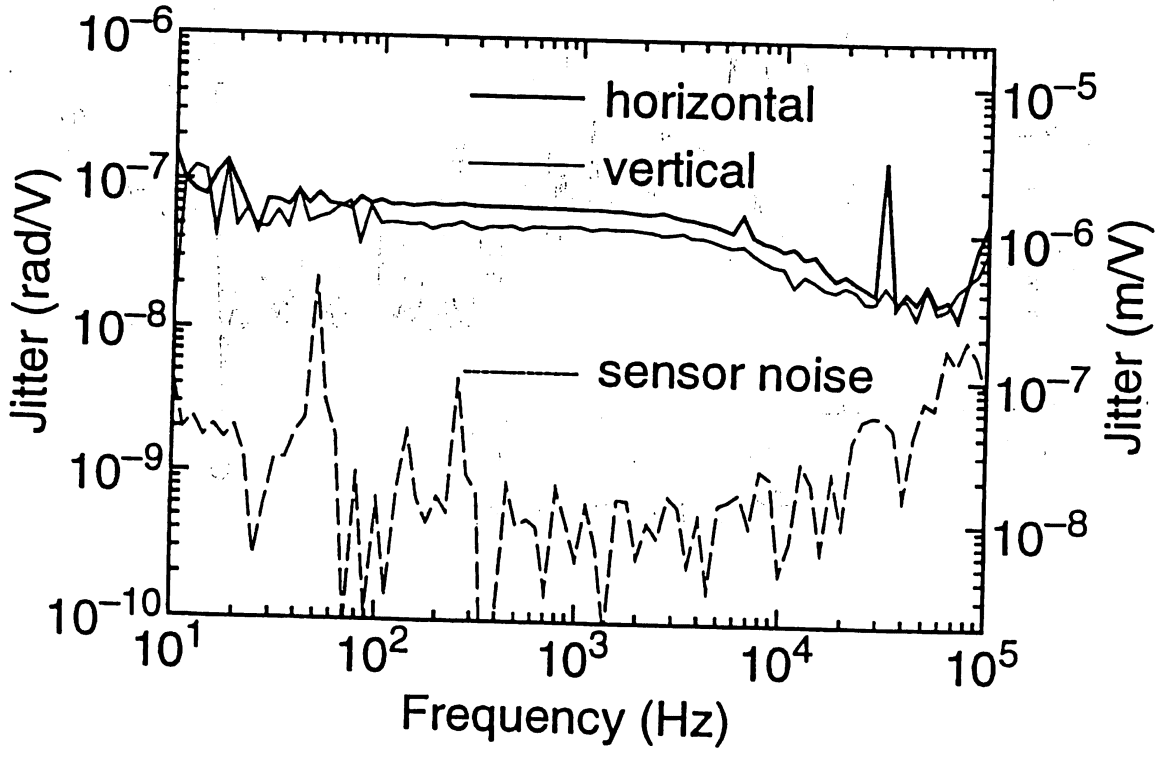

Fig.6.5 Measured jitter caused by PZT.

6.5 indicates that spurious beam jitter by controlling frequency do exist and it is the same level horizontally and vertically. Such jitter can be also reduced by Mode Cleaner.

6.1.2 Beam Jitter with Mode Cleaner

Next, we measured beam jitter in the same way when the Mode Cleaner was installed (Fig.6.6). Measurement was performed in the condition that Mode Clener cavity was locked by Frequecy Stabilization Servo. Measured beam size at the position sensor was shown in Fig.6.7.

Figure 6.8 is the horizontal beam jitter with or without Mode Cleaner along with air conditioner turned on or off. It is seen that beam jitter with Mode Cleaner unchanged irrespective of status of air condtioner. Bean jitter with displacement fluctuation δa and angle fluctuation $\delta\alpha$ induce contribution of mainly first order of the cavity mode (Eq.(4.11)),

$$U_{\text{jitter}} \simeq U_{00} + \left(\frac{\delta a}{w_0} + \mathrm{i}\frac{kw_0\delta\alpha}{2}\right)U_{10}, \tag{6.4}$$

where k and w_0 are wavelength and beam waist radius, and U_{00}, U_{10} denote TEM_{00}, TEM_{10} mode, respectively.

Transmitted mode can be expressed using Eq.(4.13) as,

$$U_{\text{transmitted}} = U_{00} + \left(\frac{\delta a}{w_0} + \mathrm{i}\frac{kw_0\delta\alpha}{2}\right)S_{10}U_{10}, \tag{6.5}$$

which corresonds to fluctuation of

$$\begin{aligned} \delta a_{\text{transmitted}} &= S_{10}\delta a \\ \delta\alpha_{\text{transmitted}} &= S_{10}\delta\alpha \end{aligned} \tag{6.6}$$

From above equation, about 60dB reduction of beam jitter is expected, using $\mathcal{F} = 1500$, ℓ=1m, R_1=1.5m, and R_2=∞. Unchange of beam jitter with Mode Cleaner is consistent with this result. On the other hand, transmitted power should fluctuate in exchange of reduction of higher mode. Figure 6.9 is the intensity

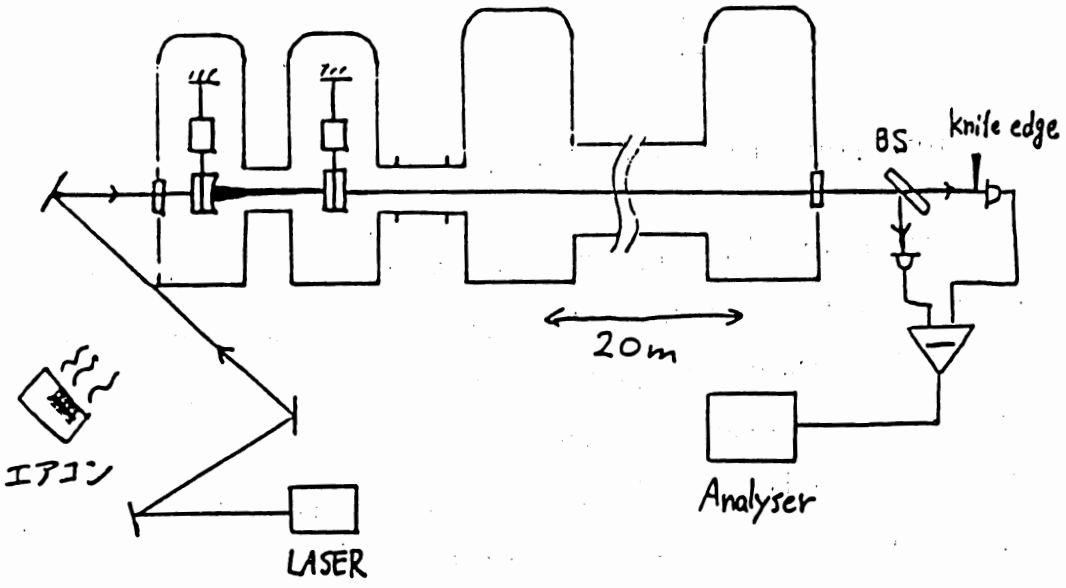

Fig.6.6 Measurement of beam jitter with Mode Cleaner.

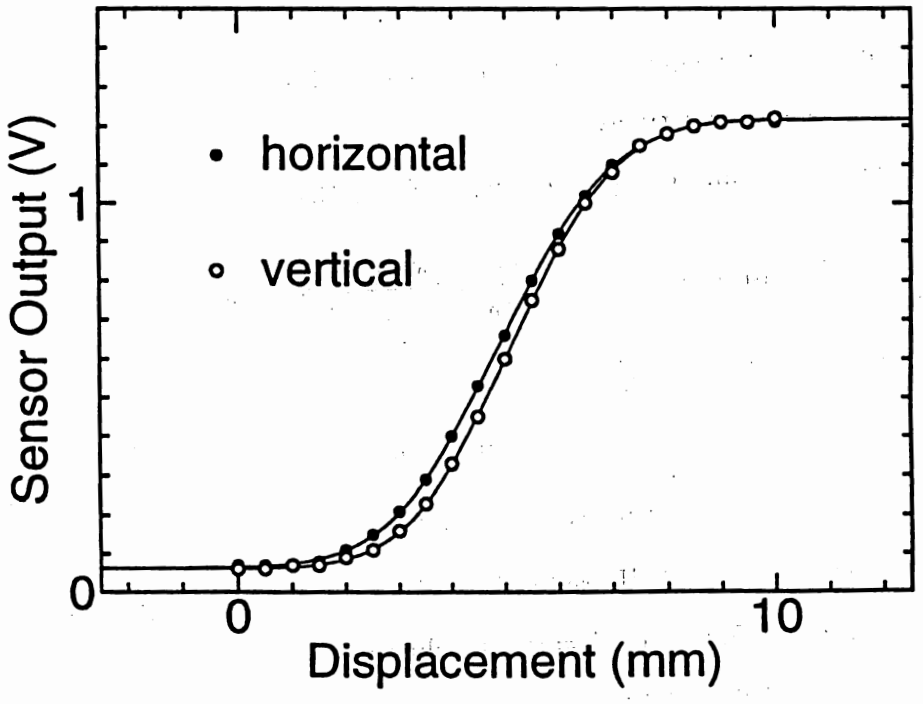

Fig.6.7 Beam radius with Mode Cleaner.

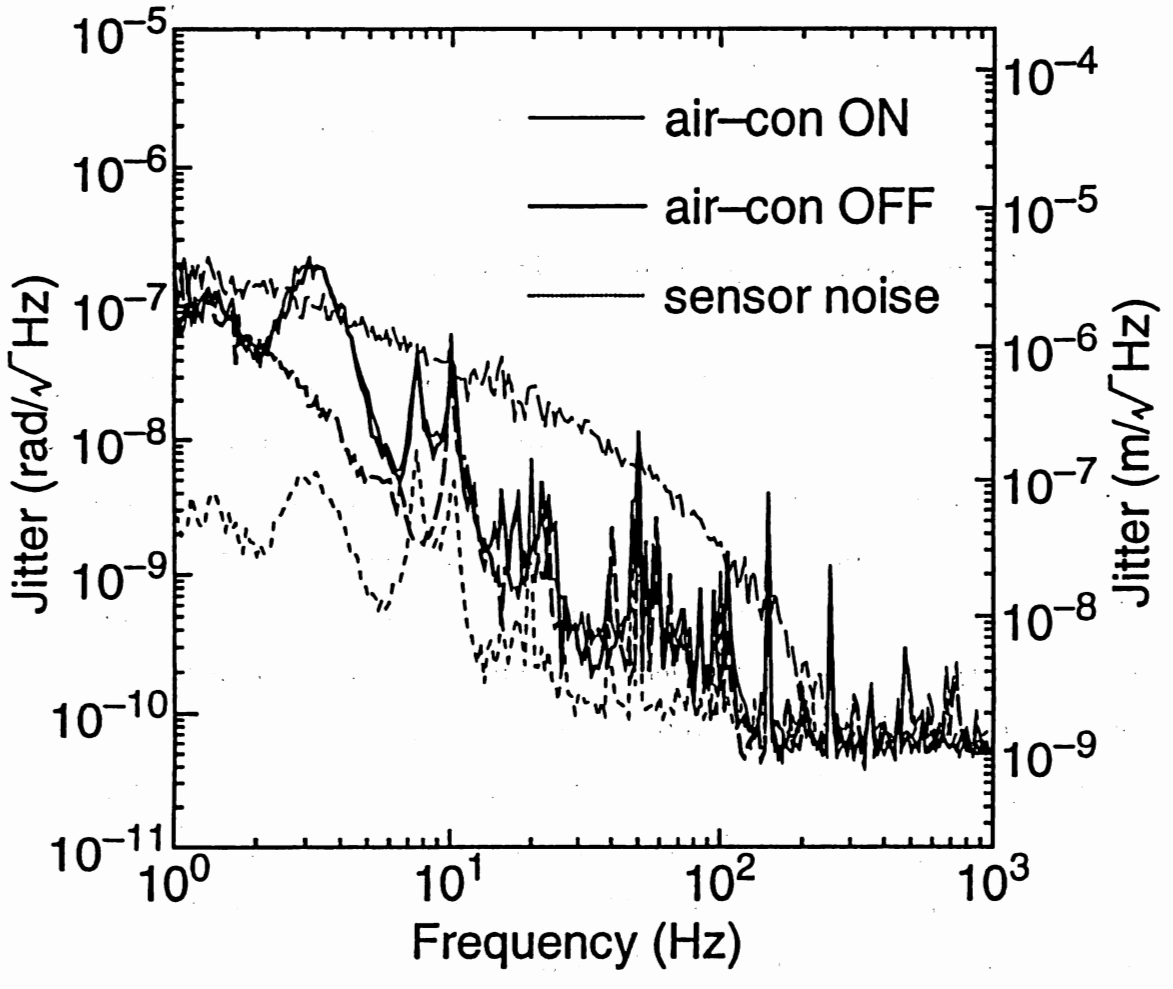

Fig.6.8 Beam jitter with Mode Cleaner.

spectrum of transmitted beam, with air conditioner on or off. Reduction of jitter was certainly converted to intensity noise.

Increase of jitter of transmitted beam when air conditioner turned off can be interpreted as instability of Mode Cleaner cavity; this can be clearly understood by comparing horizontal and vertical beam jitter (Fig.6.10). Some peaks seem resonant peak of vibration isolation system. Hence beam jitter at low frequencies depends mainly on vibration isolation of the cavity. However, long cavity may relax this situation; amount of jitter seems reversely proportional to its cavity length if parallel translation of the cavity mirrors decide jitter.

§ 6.2 Estimation of Frequency Stability

Next, we estimated frequency stability of using another Fabry-Perot cavity. Although frequency stability can be estimated from the error signal of servo system to some degree, instability due to reference Mode Cleaner cavity or detector noise cannot be estimated from the error signal. Another reference cavity with same stability or more is needed. We utilized the estimation cavity as the independently suspended Fabry-Perot with cavity length of 20m and finesse of about 350; it is the one arm of 20m Fabry-Perot prototype detector [26].

The response of the Fabry-Perot cavity with length ℓ and finesse $\mathcal{F}$ for frequency noise is proportional to $\mathcal{F}\ell$ (Eq.(4.14)), while for fluctuation of cavity lenth it is proportional to $\mathcal{F}$ (cf. Eq.(3.26)), Therefore reference Fabry-Perot with long cavity length and low finesse is regarded as good frequency reference. On the other hand, as the sensitivity of frequency noise limited by shot noise is proportional to $\mathcal{F}\ell$ (Eq.(4.16)), 20m estimation system has higher sensitivity than Mode Cleaner. Moreover, since we applied the same pendulum suspension for 20m Fabry-Perot as the one for Mode Cleaner, frequency instability due to vibration of reference Mode Cleaner cavity can be estimated.

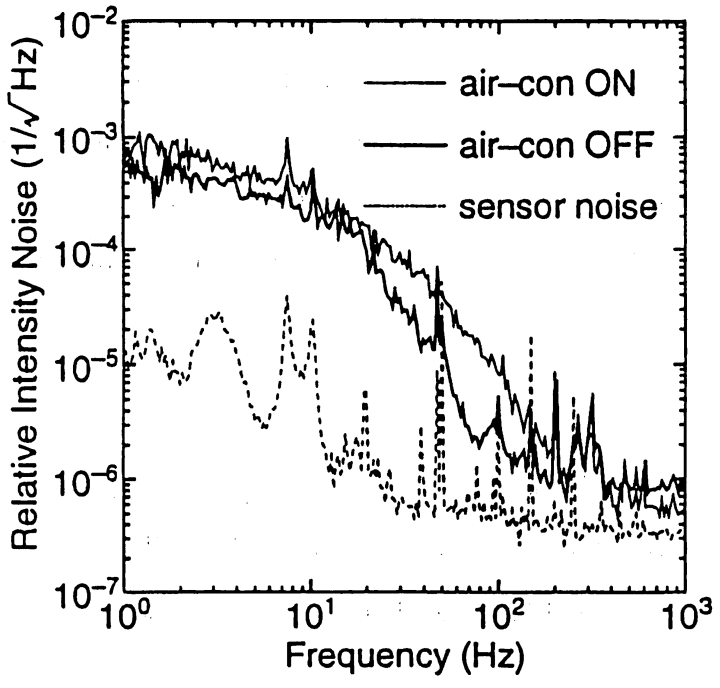

Fig.6.9 Intensity noise of transmitted light.

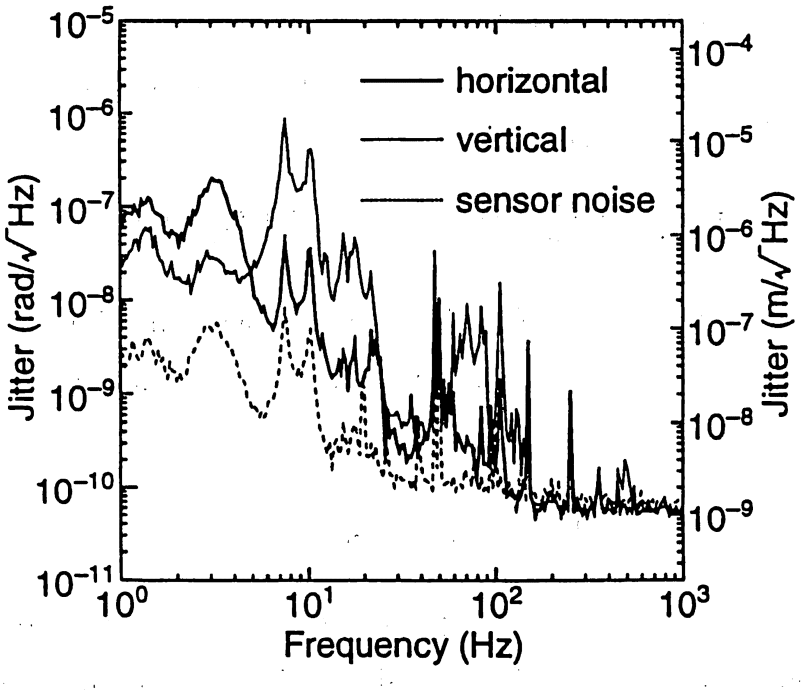

Fig.6.10 Horizontal and vertical beam jitter with Mode Cleaner.

6.2.1 Expected Frequency Noise from Mode Cleaner

Before the estimation using a 20m Fabry-Perot, expected frequency noise level which is decided both original frequency noise of the laser and servo gain was evaluated from the error signal of Mode Cleaner. First we calibrated to convert obtained error signal to frequency noise, and then estimated the stabilized frequency noise level.

· *Calibration*

The output error signal was converted to corresponding frequency noise using the index obtained from calibration shown in Fig.6.11. Vibration of front mirror produces change of resonant frequency of the cavity expressed as (Eq.(3.26)),

$$\delta\nu = \frac{\nu}{\ell}\delta x \tag{6.7}$$

where ν, ℓ, and δx are resonant frequency of the cavity, cavity length, and vibration amplitude of the front mirror, respectively. Hence relation between δx and error signal gives the index which converts error signal to frequency. Vibration amplitude δx can be obtained from the Michelson interferometer formed as dashed lines in Fig.6.11. Output of the detector V_{M} can be expressed using maximum and minimum intensity (V_{max}, V_{min}) as,

$$V_{\mathrm{M}} = \frac{V_{\mathrm{max}} - V_{\mathrm{min}}}{2}\sin(2kx) + \frac{V_{\mathrm{max}} + V_{\mathrm{min}}}{2} \tag{6.8}$$

where k and x are a wavelength of the light and displacement of the front mirror. If the average position of front mirror is controlled so as to $\sin(2kx) = 0$ satisfies, small vibration from average position is detected as,

$$\delta V_{\mathrm{M}} = (V_{\mathrm{max}} - V_{\mathrm{min}})k\delta x \tag{6.9}$$

Figure 6.12 shows the frequency response between signal 1 and 2 for Michelson and between signal 1 and 3 for MC error signal. Both curves are inversely proportional to the square of vibration frequency, which reflects frequency response

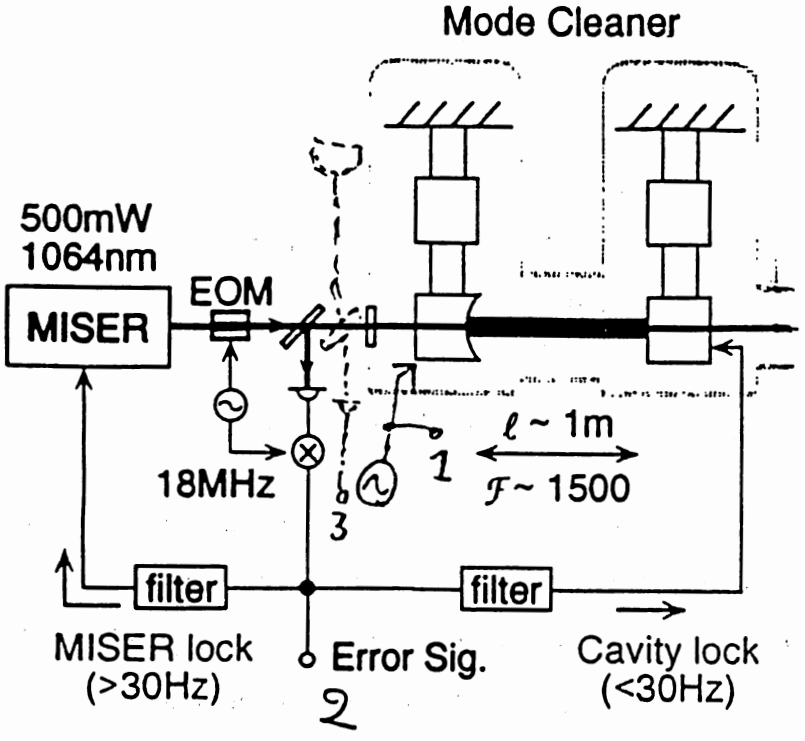

Fig.6.11 Calibration of Mode Cleaner.

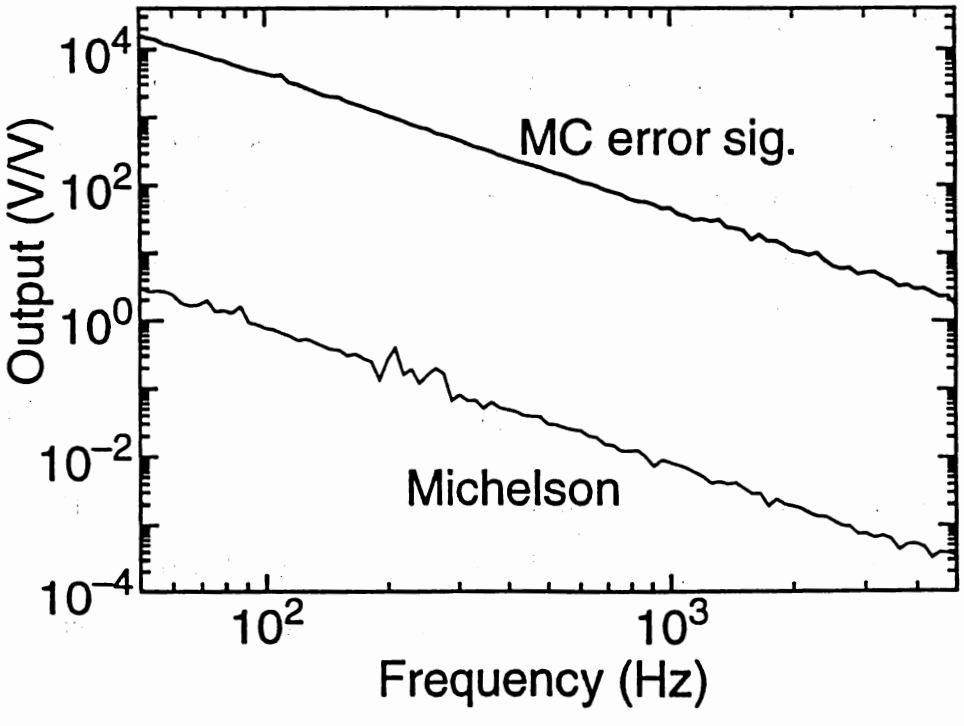

Fig.6.12 Calibration curve for Mode Cleaner.

between applied force and displacement of the front mirror. From the figure we obtained the relation $V_{\mathrm{MCerror}} = 5.5 \times 10^3 V_{\mathrm{M}}$. Using V_{max}=4.9V and V_{min}=0.5V we had the index

$$\begin{aligned} V_{\mathrm{MCerror}} &= 5.5 \times 10^3 k(V_{\mathrm{max}} - V_{\mathrm{min}}) \frac{\ell}{\nu} \delta\nu \\ &= 5.0 \times 10^{-4} \delta\nu \end{aligned} \tag{6.10}$$

· ***Estimation of Frequency Noise from Error Signal***

Figure 6.13 is the frequency noise level obtained from the error signal of Mode Cleaner. Thin line was obtained when Cavity Lock Loop (Section 5.1.8) worked. Above 30Hz the spectrum shows typical tendency of frequency noise of MISER, inversely propotional to Fourier frequency, while vibration of pendulum motion can be read below 30Hz. When stabilized, error signal reduced down to the dashed curve. This level well agrees with the theoretical level calculated from thin line and servo gain (Fig.5.28). Taking into account the feedback loop to the pendulum at low frequencies, expected frequency noise was calculated from stabilized error signal as shown 'stabilized level'.

In order to estimate such noise contribution to the frequency noise that does not appear in the error signal, we measured or estimated the possible noise sources and calculated noise contribution using Fig.6.14. Figure 6.15 is electrical and seismic noise contribution to the frequency noise, where seismic noise of the ground is assumed to be (x:displacement in m/$\sqrt{\mathrm{Hz}}$, f:vibration frequency in Hz),

$$x(f) = \frac{10^{-7}}{f^2} \tag{6.11}$$

Near the bottom of stabilized level, several electric noise sources match the stabilized level. If we want to stabilize with larger servo gain, this result suggests we have to reduce such electric noise. Anyway, in our current system such noise contribution can be regarded negligible.

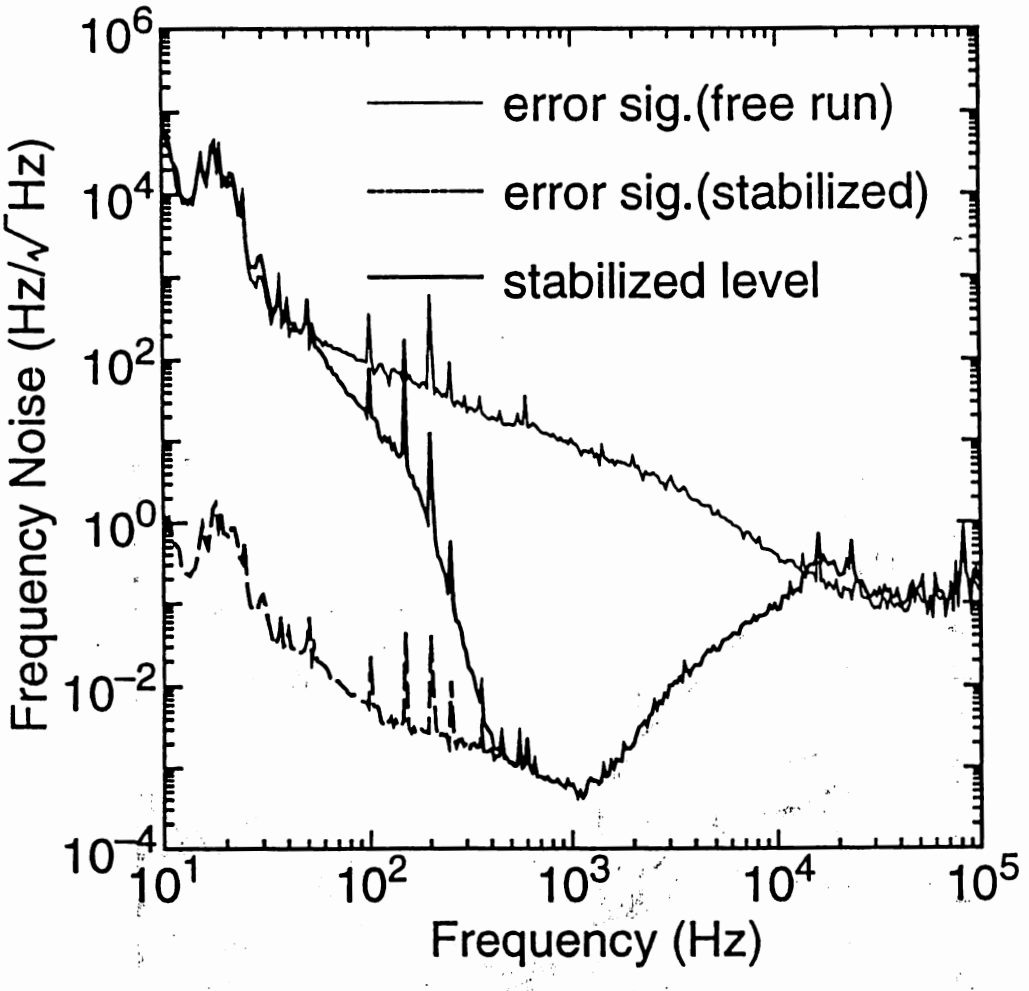

Fig.6.13 Frequency noise obtained from error signal.

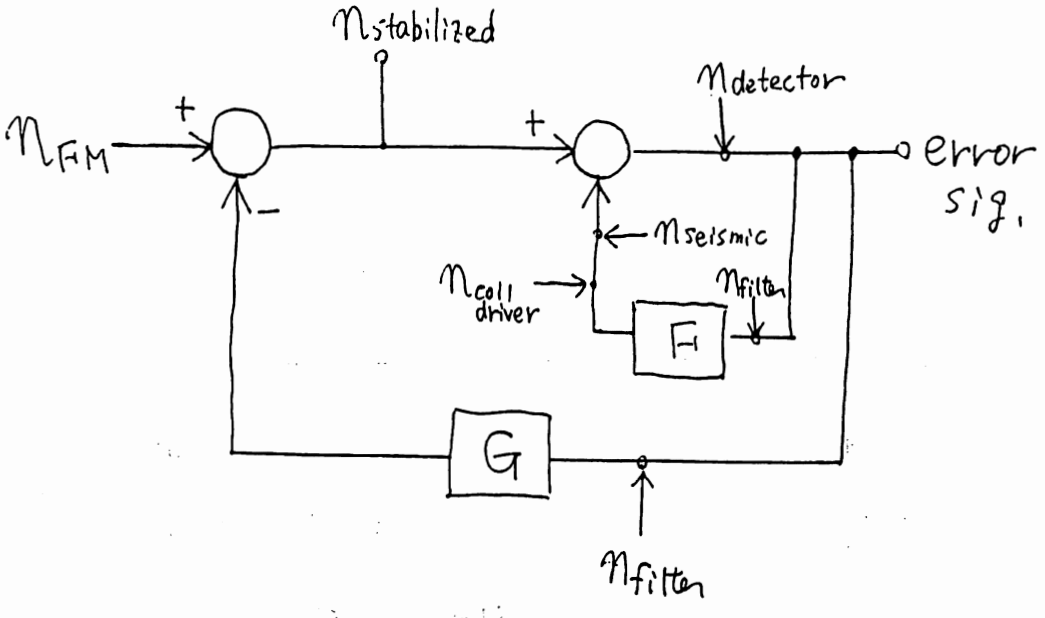

Fig.6.14 Block diagram for noise estimation.

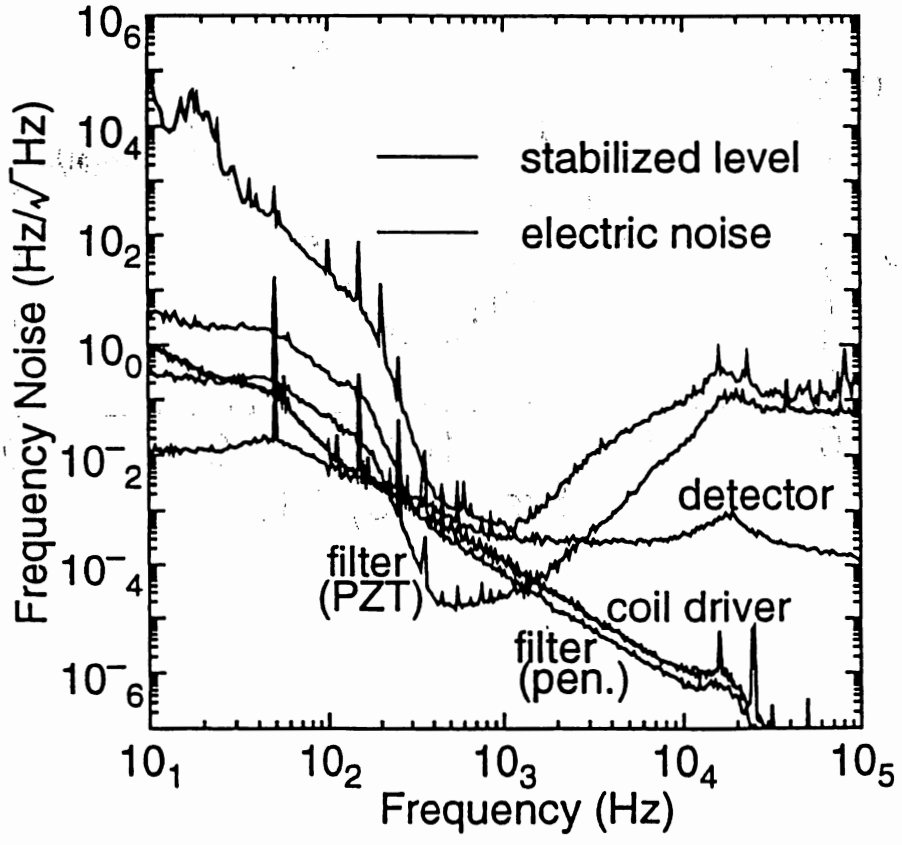

Fig.6.15 Noise estimation for Mode Cleaner.

6.2.2 Frequency Noise Estimated from 20m Fabry-Perot Cavity

Figure 6.16 shows the setup for estimation of frequency noise of Mode Cleaner using a 20m Fabry-Perot. Vacuum chamber of Mode Cleaner was connected to the Center Tank of the 20m Fabry-Perot prototype, and the transmitted beam from the Mode Cleaner illuminated the 20m estimation cavity housed in one arm of the chamber. Mirrors of the 20m cavity was the one used for the 20m prototype, which has diameter of 50mm and 100mm long and is monolithic mass made of fused silica: front mirror is flat, and end mirror has concave curvature radius of 30m. Other components of 20m cavity, e.g.vacuum system, are described in detail in the following Chapter 7.

In order to obtain signal, transmitted beam from the Mode Cleaner was phase-modulated with 40MHz and reflected beam from the 20m Fabry-Perot was extracted by optical circulator and then detected. Signal was obtaind in the same way as Mode Cleaner and fed back to the end mass to keep the cavity on resonance; unity gain frequency of the servo was about 1.2kHz.

Before measurement of noise, we calibrated the signal in the similar way as previous calibration.

· *Calibration*

Setup for calibration of 20m Fabry-Perot is also shown in Fig.6.16. The Mode Cleaner cavity as a frequency reference was vibrated in the same way as calibration of Mode Cleaner, resulting in the frequency modulation of stabilized beam. Since modulation index was already known from previous calibration of Mode Cleaner, from the output of 20m Fabry-Perot we could calibrate the signal. Thin line in Fig.6.17 is the modulation in terms of error signal of Mode Cleaner, which is evaluated from the response function between signal 1 and 2. The curve shows almost the same shape as the one in Fig.6.12 except for the tendency at low frequencies ($\lesssim$100Hz) effected by the Pendulum Loop. On the other hand, thick line is the response function between signal 1 and 4 in terms of error signal of 20m

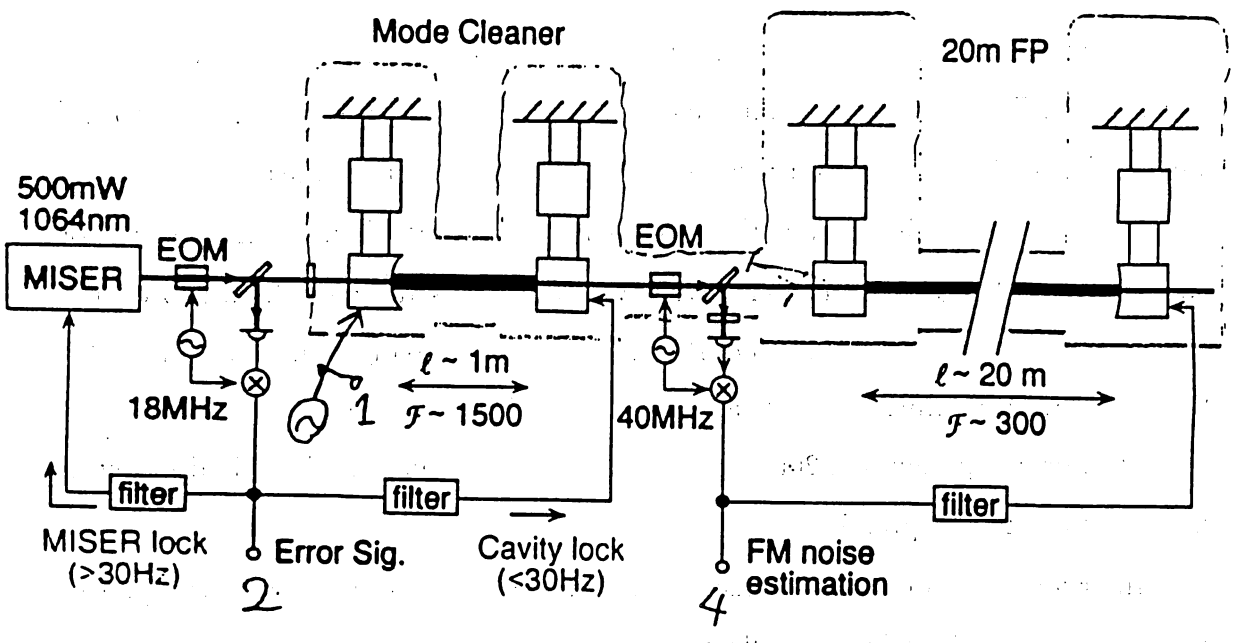

Fig.6.16 Setup for frequency noise estimation using 20m Fabry-Perot.

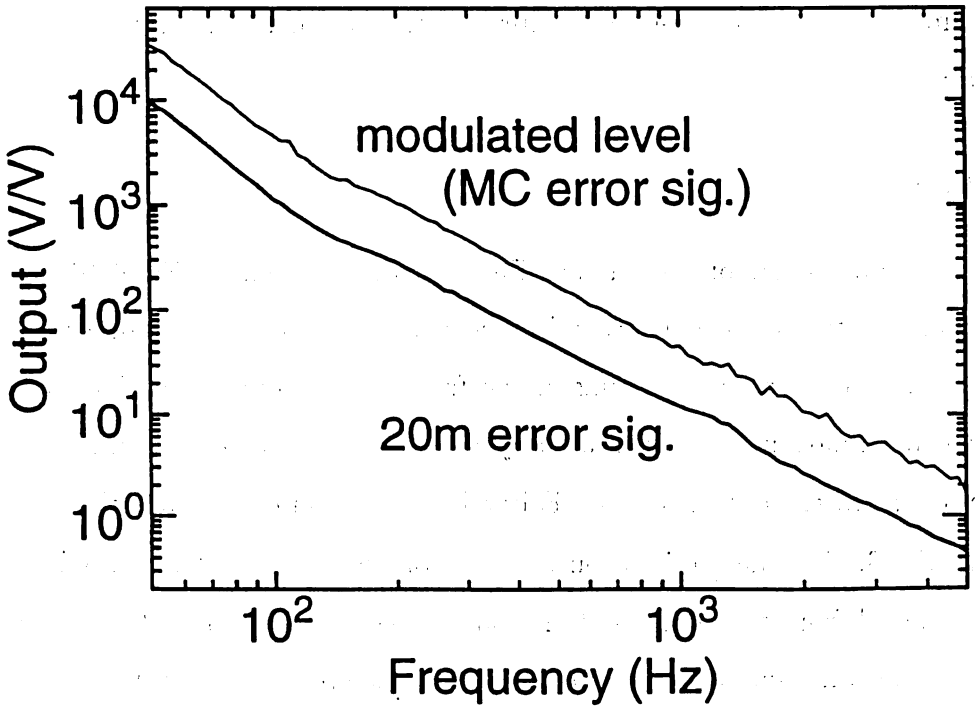

Fig.6.17 Calibration for 20m Fabry-Perot.

Fabry-Perot. From the relation between two signals, $V_{20\mathrm{mFP}} = 0.25 V_{\mathrm{MCerror}}$, we have

$$\begin{aligned} V_{20\mathrm{mFP}} &= 0.25 \times 5.0 \times 10^{-4} \delta\nu \\ &= 1.3 \times 10^{-4} \delta\nu \end{aligned} \tag{6.12}$$

· ***Estimation of Frequency Noise from 20m Fabry-Perot***

Figure 6.18 shows the calibrated spectra from 20m Fabry-Perot, as well as the one from Mode Cleaner. Both dashed curves, which means without stabilization, well agree with each other except below 30Hz. The difference comes from cavity length; for a Fabry-Perot cavity with a certain finesse, response against the frequency noise is proportional to the cavity length while response for the vibration of mirrors is unchanged to the cavity length within the cut-off frequency of the cavity. Therefore long cavity is insensitive to the seismic noise relatively to the frequency noise. The difference by a factor of $\sim$ 10 below 30Hz is explained as the difference of cavity length by a factor of 20. When stabilized, due to above instability of Mode Cleaner for seismic noise relative to 20m Fabry-Perot, stabilized noise level of 20m Fabry-Perot is enhanced up to the noise level of Mode Cleaner below 30Hz.

Another remarkable feature is discrepancy between expected level obtained from Section 6.2.1 and 20m error signal when stabilized. Excess noise seems to come from Mode Cleaner and/or 20m Fabry-Perot. As the possible noise sources were estimated for the Mode Cleaner, we evaluated the possible excess noise for 20m system (Fig.6.19) using Fig.6.20. Detector noise was above the expected level, but it was below the obtained noise. Other electric noise was well below the expected level.

From the complex structure of the excess noise region, we assumed that it cames from mechanical vibration excited by seismic noise, and we observed the change of the spectrum against the external vibration applied purposely. Figure 6.21 is the change of the spectra when the vibration of rotary vacuum pump was activated near the vacuum chamber.

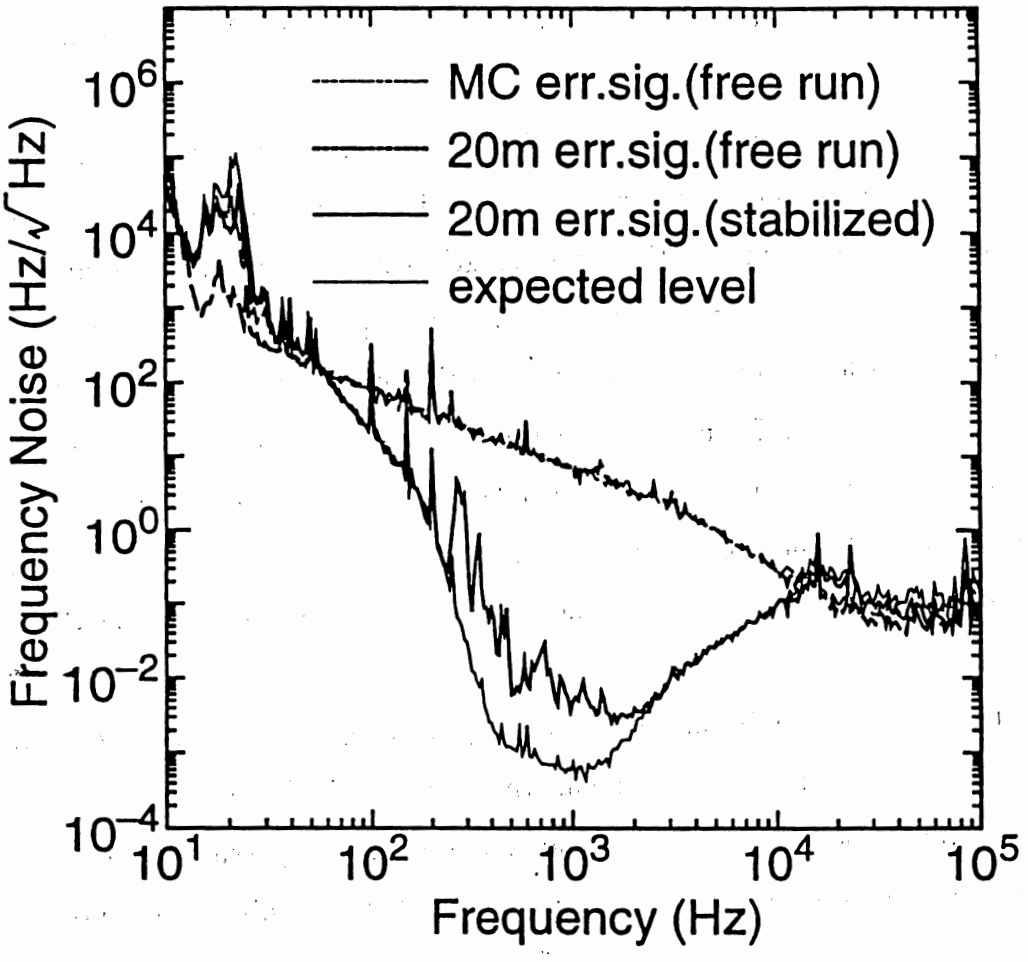

Fig.6.18 Frequency noise estimated by 20m Fabry-Perot.

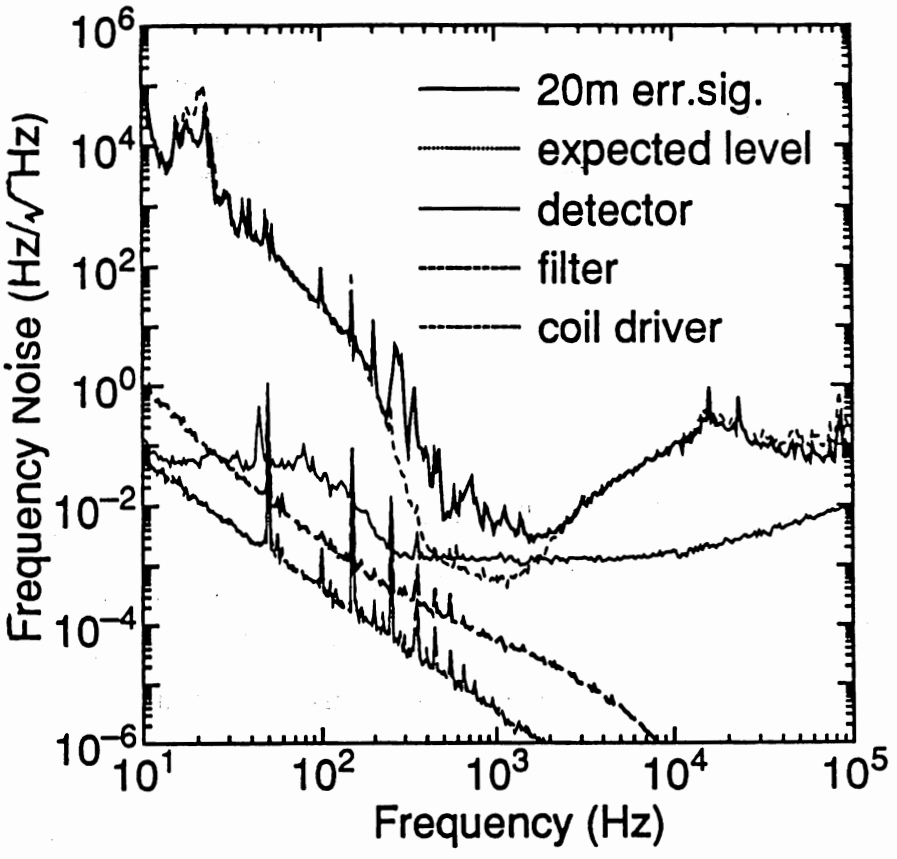

Fig.6.19 Estimated noise for 20m Fabry-Perot.

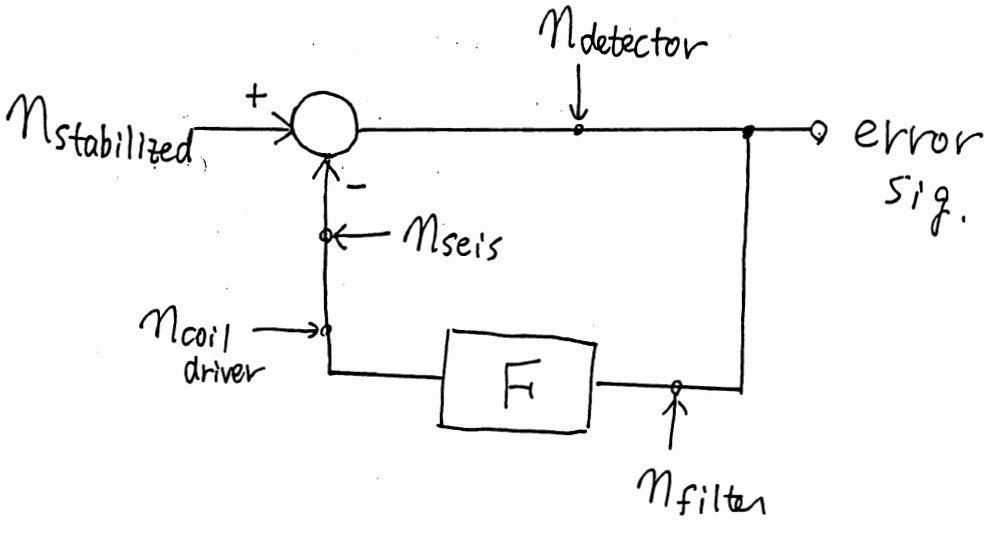

Fig.6.20 Block diagram for noise estimation.

Result of significant effect for center tank seems to suggest the effect of steering mirrors (M's in Fig.6.16) fixed to the table. If the optical path length is changed due to the vibration of the mirrors, resulting phase change is

$$\delta\phi = k\delta x \tag{6.13}$$

which corresponds to frequency noise of

$$\delta\nu(f) = 2\pi f k \delta x(f) \tag{6.14}$$

where f is a frequency of vibration. This phase noise due to steering mirrors is also shown in Fig.6.21 assuming seismic spectrum as (6.11). As the vibration of the mirrors is not the same as ground motion, the noise level may be larger than the drawn level. The effect of phase noise can be confirmed by isolating the steering mirrors.

Another noise sources is vibration of cavity mirrors. Effect of vibration for end tank indicates insufficient vibration isolation of the pendulum. Theoretical vibration level assuming (5.5) is shown as seismic in Fig.6.21. Although it is well below the obtained frequency noise level, excess vibration noise due to resonance of suspension wires or blade springs, or excitation of seismic noise from damping magnets may near obtained level. Vibration level of the table is also unknown.

In both cases (phase noise due to steering mirrors or vibration of cavity mirrors), vibration isolation should be reinforced especially above 100Hz. One possible way for such isolation is using stacks which is, say, layers of lead and rubber. However, for the future detector (see Chapter 8) which can detect low frequency gravitational waves, such stacks will have insufficient isolation ratio and are not good for ultra-high vacuum. Improvement or another type of isolation system should be investigated.

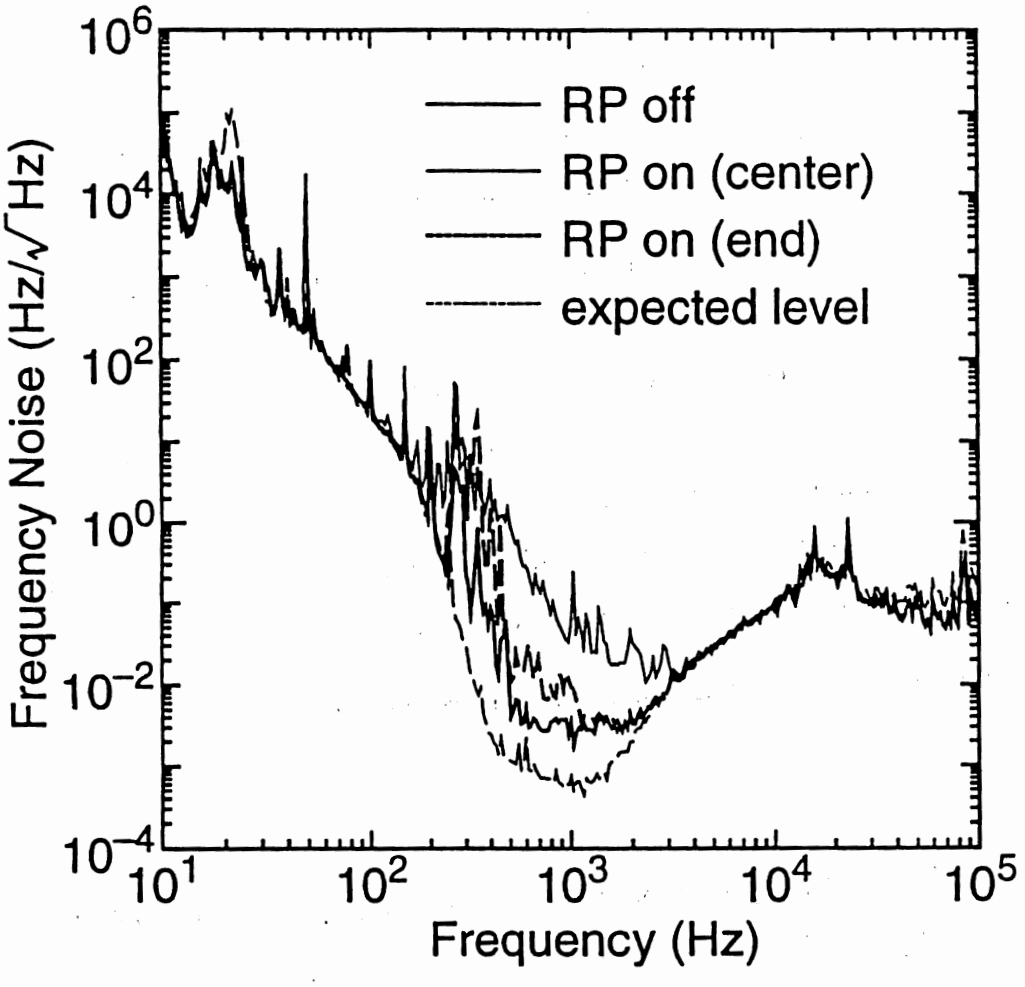

Fig.6.21 Noise level with external vibration applied.

7. Operation of 20m Fabry-Perot Prototype with 1-m Mode Cleaner

§7.1 20m Fabry-Perot Prototype

As a conclusion of this experiment, we operated 20m Fabry-Perot prototype detector with Mode Cleaner [27, 29] in order to confirm the improved performance as well as the stability of operation. Concerning the 20m Fabry-Perot prototype without Mode Cleaner at National Astronomical Observatory (NAO, Mitaka, Tokyo), see references [6, 26]. Remarkable characteristics of the prototype are

- Schnupp method (pre-modulation) is applied to realize recombined scheme which is compatible with recycling.
- Laser Diode pumped Nd:YAG laser (λ=1064nm) has been used as a light source, because it is considered as one of the promising lasers which will be developed to high-power laser with stability.
- Vacuum chamber for prototype is made of aluminum alloy, which can attain vacuum pressure of below 10^{-5}Pa without baking.

In the following subsection, schematic features are described.

7.1.1 Apparatus

The 20m Fabry-Perot prototype detector is located in the middle of Mitaka campus of NAO (Fig.7.1). The L-shaped prefab was specially built to house the interfeormeter; each arm is directed to notheast and northwest respectively. Since the building is independent from other buildings, enviroment in ground vibration is relatively good for interferometer. Moreover the base plate to fix vacuum chamber is isolated from the floor in order to reduce the effect of vibration of the building.

Figure 7.2 is the schematics of vacuum chamber used for 20m Fabry-Perot prototype; diameter and height of center tank are 1.4m and 2.0m and those of

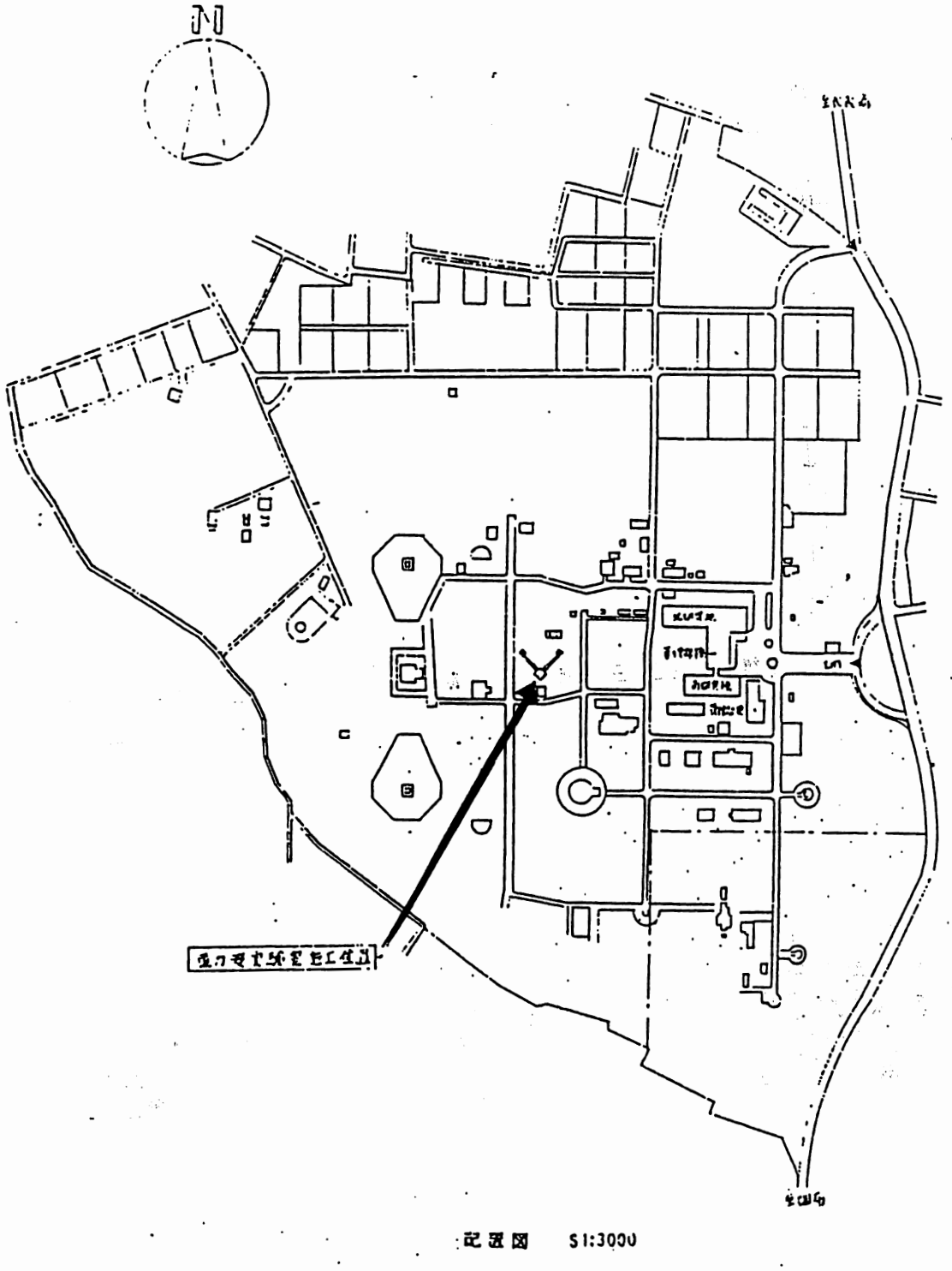

Fig.7.1 Location 20m Fabry-Perot prototype in Mitaka campus of NAO.

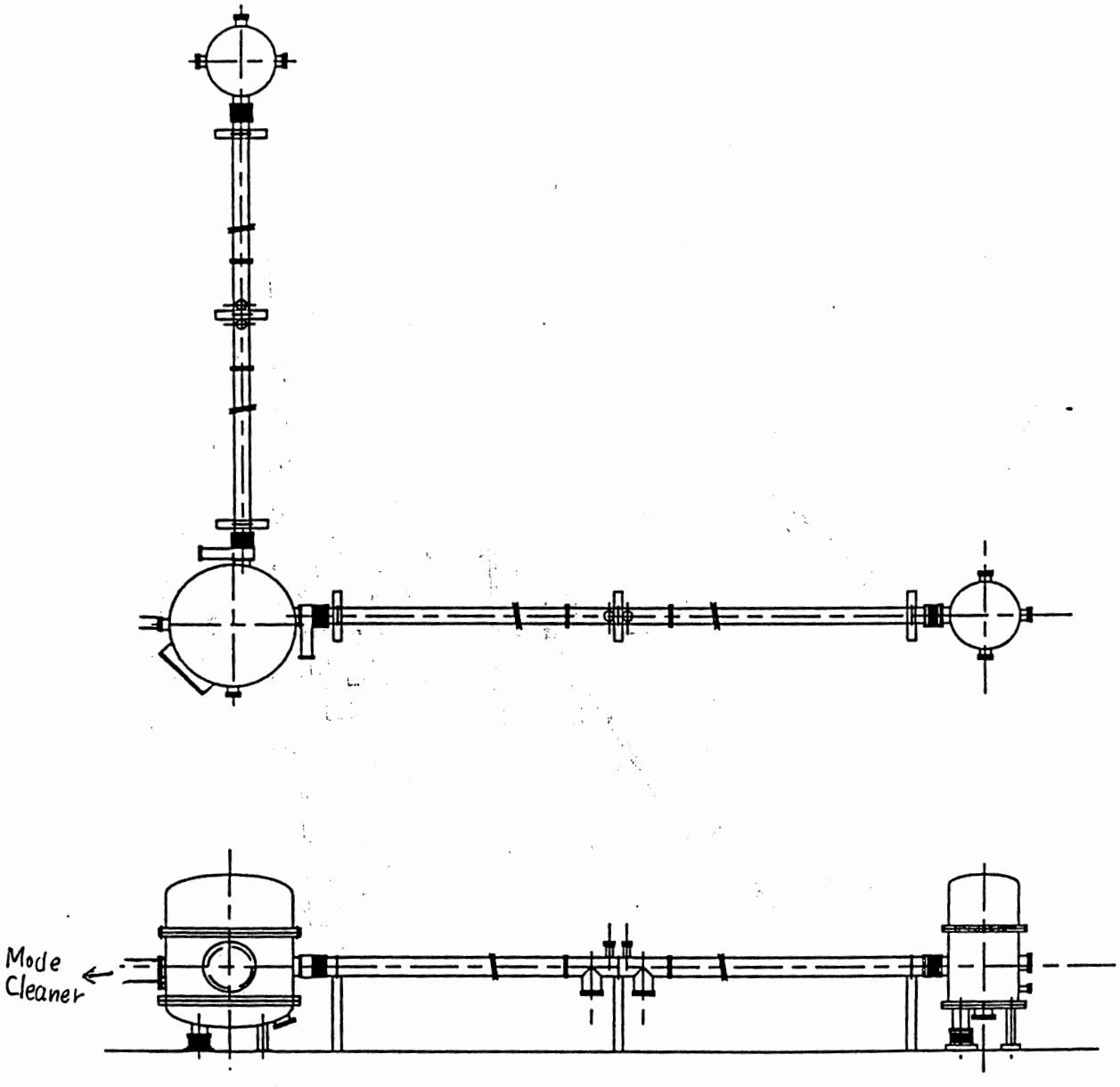

Fig.7.2 Vacuum chamber for 20m Fabry-Perot prototype detector.

each end tank are 0.8m and 2.0m, respectively. Inner surface of these tanks was treated with EX-GBB (Glass Bead Blast) to remove impurities. Electric signal can be supplied by the feedthrough located at the bottom of each tank, and the laser beam can be extracted through the optical window. Mode Cleaner vacuum chamber is connected with center tank as shown in Fig.7.2. Optical bench in the tank is fixed directly to the ground while tank itself is isolated from the ground with bellows; this mechanism serves to reduce deformation of optical bench affected by vacuum tank in evacuation. Optical bench is made of 3cm-thick bulk aluminum, which we were obliged to apply due to poor vacuum performance of honeycomb breadboard. Vibration resonance of the bench seems to affect the noise level (Section 6.2.2, 7.2).

Vacuum pumps are located as Fig.7.3. In operation of prototype, all the pumps are turned off or only turbo pumps located in the middle of the pipes evacuate; diameter of the pipes is 0.2m and they connect tanks with bellows which works vibration isolation from the vacuum pump. In operation when evacuated with middle-pipe vacuum pumps, pressure of less than 4×10^{-4}Pa could be kept including Mode Cleaner chamber. Vacuum status of all chambers are obtained by date acquisition system and can be remotely monitored by workstation through network.

7.1.2 Optical Design

Optical design for 20m Fabry-Perot prototype is shown in Fig.7.4. Transmitted light from Mode Cleaner is modulated in phase with 40MHz using EOM because phase modulation with 18MHz before the Mode Cleaner cannot transmit with this cavity length 1m. The modulated beam is lead to the main interferometer through two lenses for mode matching (Fig.7.5) and steered by two mirrors. Phase modulator with 2mmϕ aperture is inserted near the beam waist. Incident beam is separated by beam splitter; transmitted beam illuminates the 20m Fabry-Perot of east arm (henceforth we call east arm because this arm is directed to notheast),

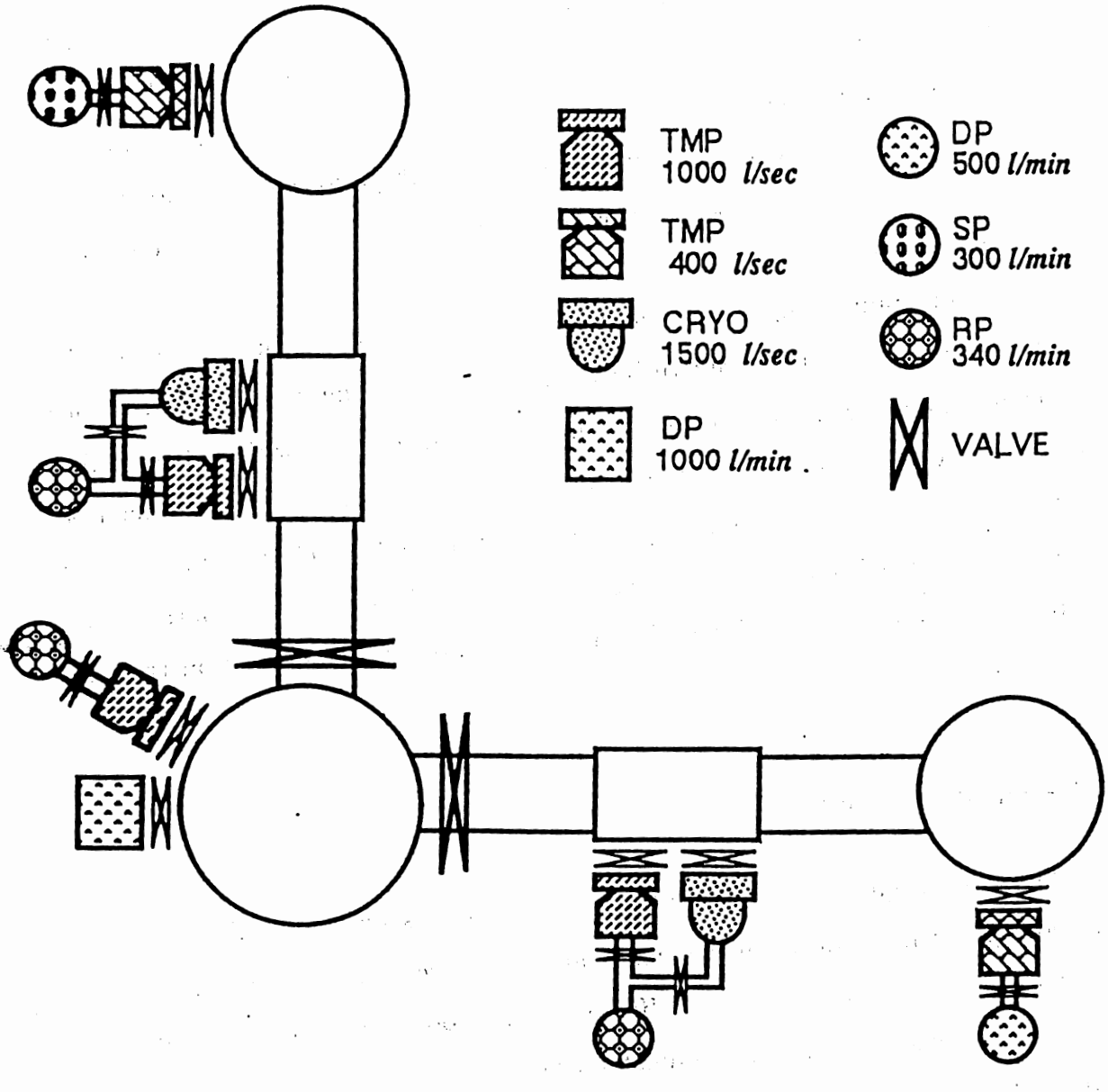

Fig.7.3 Vacuum pump system for 20m Fabry-Perot.

while reflected light illuminates west arm Fabry-Perot (we call west in the same reason). Front mirrors are flat mirror with diameter of 50mm and 100mm long and end mirrors are concave mirror with curvature radius of 30m; they are made of monolithic fused silica. All the mirrors comprising Fabry-Perot are suspended with the same pendulums as Mode Cleaner (Piture). Only beamsplitter is suspended by different system without vertical vibration isolation (Picture).

Reflected light from each Fabry-Perot is picked up partially ($\lesssim 1\%$) on the anti-reflection surface of beamsplitter and extracted as a signal to lock arm Fabry-Perot on resonance. The main beam is recombined at the beamsplitter and detected as a main signal which contains signal of gravitational waves as well as signal to controll beamsplitter at dark fringe. The other beam going back to Mode Cleaner is extracted from optical isolator in order both to avoid excess noise of scattered light and to monitor status of the beam in the chamber. Location of optical components and beam lines in the center tank is shown in Fig.7.6. Distance between each front mirror and beamsplitter is purposely made different in order to obtain main signal by Schnupp method. Degradation of contrast due to this path difference is 2×10^{-4} for the ideal TEM_{00} mode.

7.1.3 Servo Design

Block diagram of servo system to lock Fabry-Perot or beamsplitter is also shown in Fig.7.4. Beam from the interferometer is detected outside the chamber with resonant type detectors. They are the same performance each other and have resonant frequency of 40MHz and quality factor of about 5 (Fig.7.7). Equivalent noise photocurrent is about 100μA.

Detected signal from each arm is demodulated and fed back to the end mass in order to keep the arm Fabry-Perot on resonance. Main signal from beamsplitter is also demodulated and fed back to the beamsplitter to keep dark fringe. Open loop gain of these servo is shown in Fig.7.8. Servo for each arm (east or west) is made the same property in order to maximize Common Mode Rejection Ratio

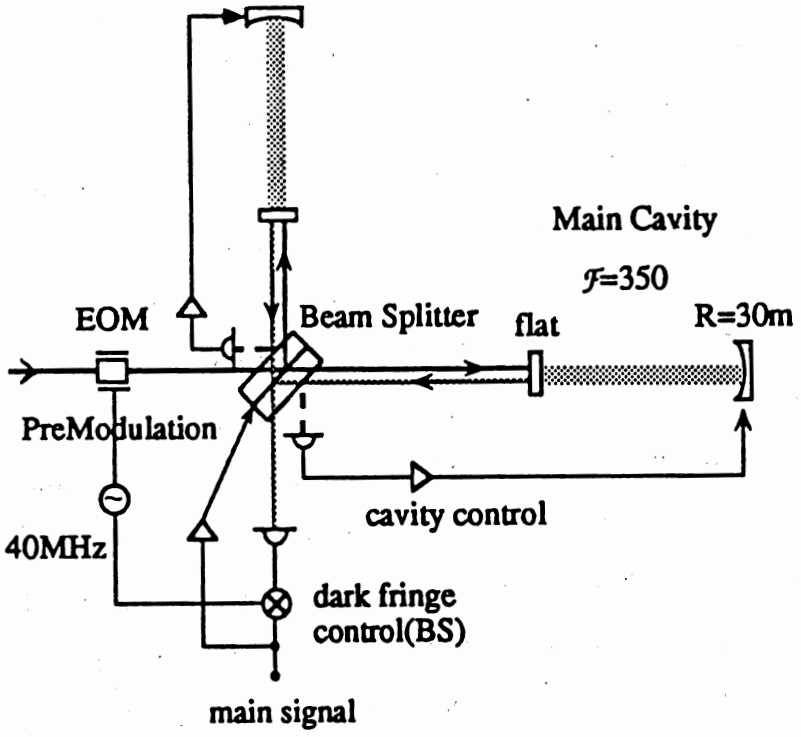

Fig.7.4 Optical design for 20m Fabry-Perot.

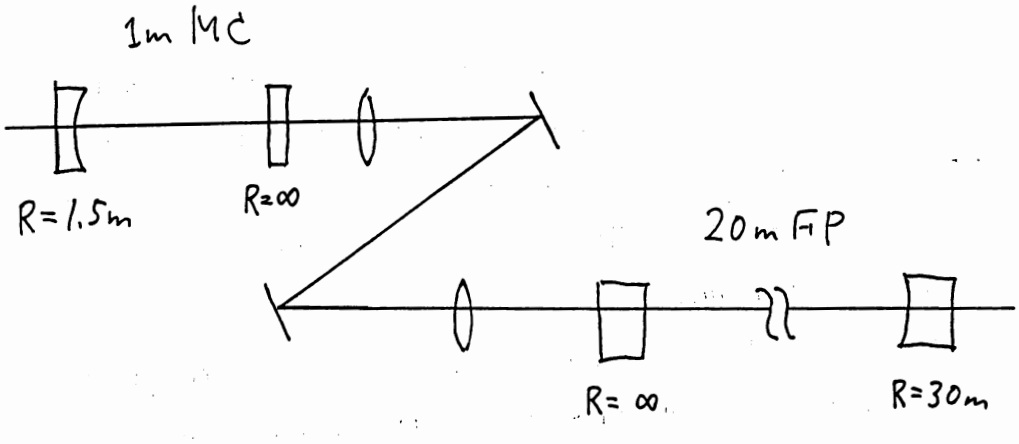

Fig.7.5 Mode matching for 20m Fabry-Perot.

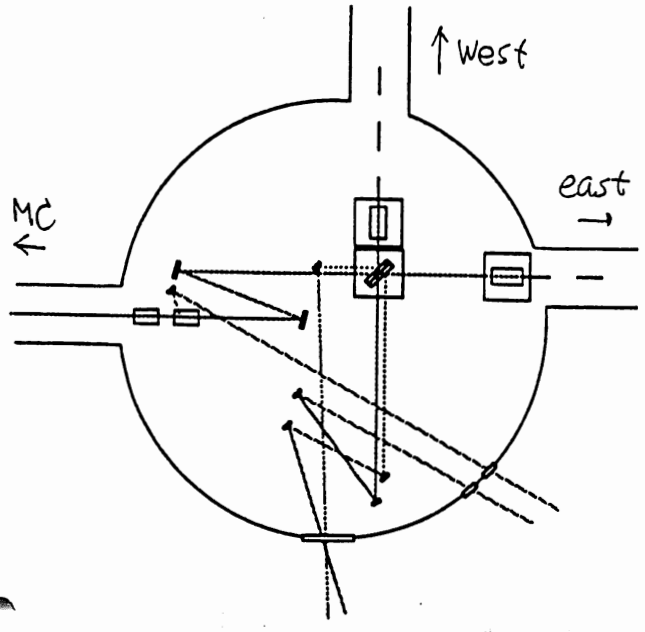

Fig.7.6 Location of components of center tank.

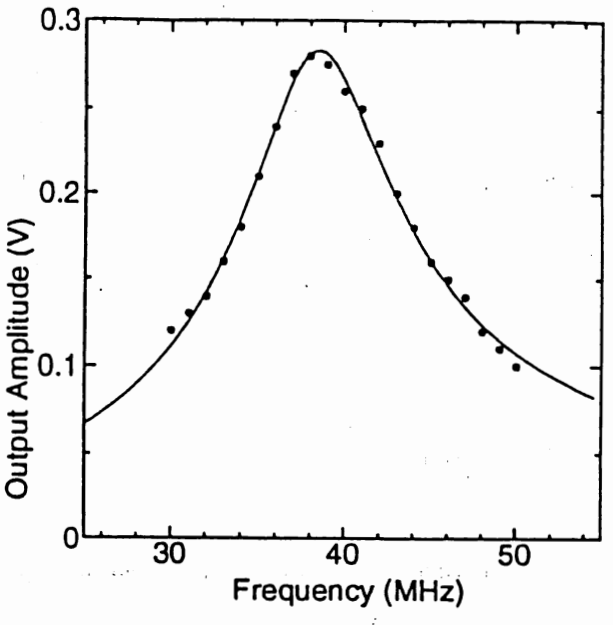

Fig.7.7 Resonant curve of the detector.

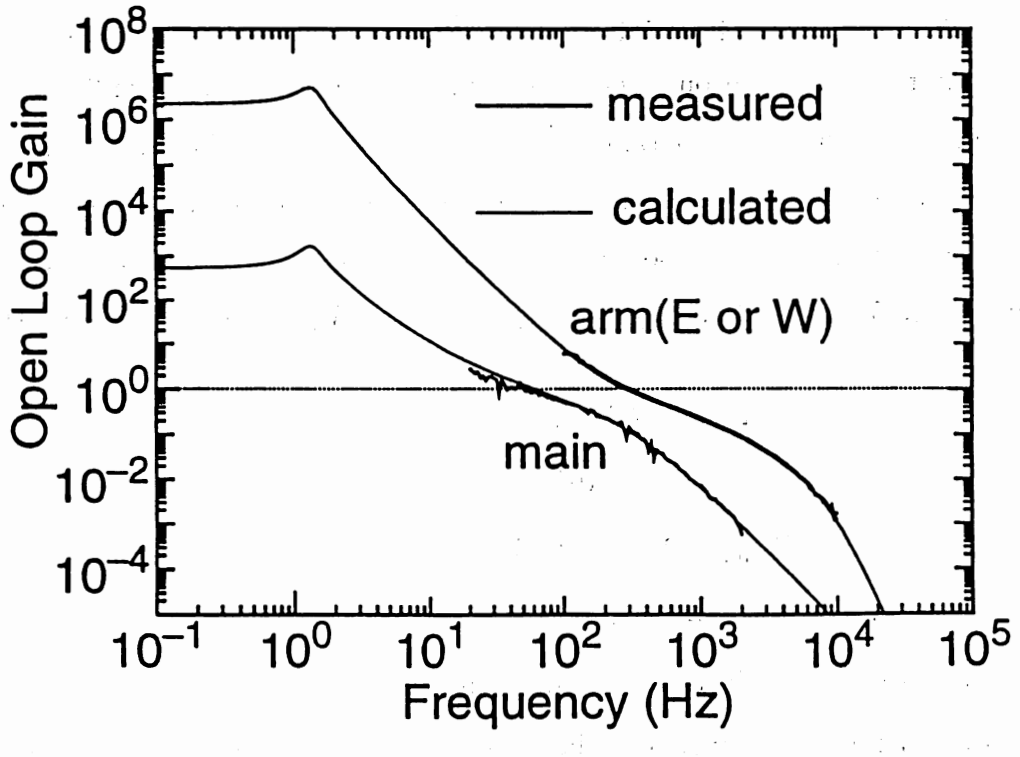

Fig.7.8 Open loop servo gain for 20m prototype.

(CMRR).

Servo gain in the observation band is designed to be below unity to avoid compensation of effect of gravitational waves by the servo loop; unity gain frequency of each loop is about 300Hz which satisfies the above situation. Unity gain frequency of the main loop is about 50Hz because of the mechanical resonance of beamsplitter near 250Hz; servo gain of main loop is not enough to supress external noise at low frequencies.

7.1.4 Calibration

Calibration to obtain displacement noise from the output was performed in the similar way as Mode Cleaner; instead of forming another Michelson interferometer, Michelson interferometer formed with each front mirror was utilized.

Figure 7.9 shows calibration for 20m Fabry-Perot prototype. After calibrating vibration amplitude of front mirror of east arm using Michelson interferometer of front mirrors, output of the prototype for the vibration was obtained. Figure 7.10 is the output for the vibration of east front mirror; tendency like Fig.6.12 can be seen. From the figure we obtain the relation of $V_{\mathrm{east}} = 14V_{\mathrm{M}}$ and $V_{\mathrm{main}} = 2.0 \times 10^2 V_{\mathrm{M}}$, where V_{east}, V_{main}, and V_{M} are the output error signal of east arm, main interferometer, and Michelson interferometer formed with each front mirror, respectively. Referred to (6.9) using V_{max}=6.3V and V_{min}=0.05V we have the relation

$$\begin{aligned} V_{\mathrm{east}} &= 14k(V_{\mathrm{max}} - V_{\mathrm{min}})\delta x \\ &= 5.1 \times 10^8 \delta x \\ V_{\mathrm{main}} &= 2.0 \times 10^2 k(V_{\mathrm{max}} - V_{\mathrm{min}})\delta x \\ &= 7.3 \times 10^9 \delta x \end{aligned} \tag{7.1}$$

where δx is vibration amplitude of east front mirror.

Calibration for west arm is calculated from the ratio of gain of servo filter between east and west, considering the same setup of each arm; the ratio comes

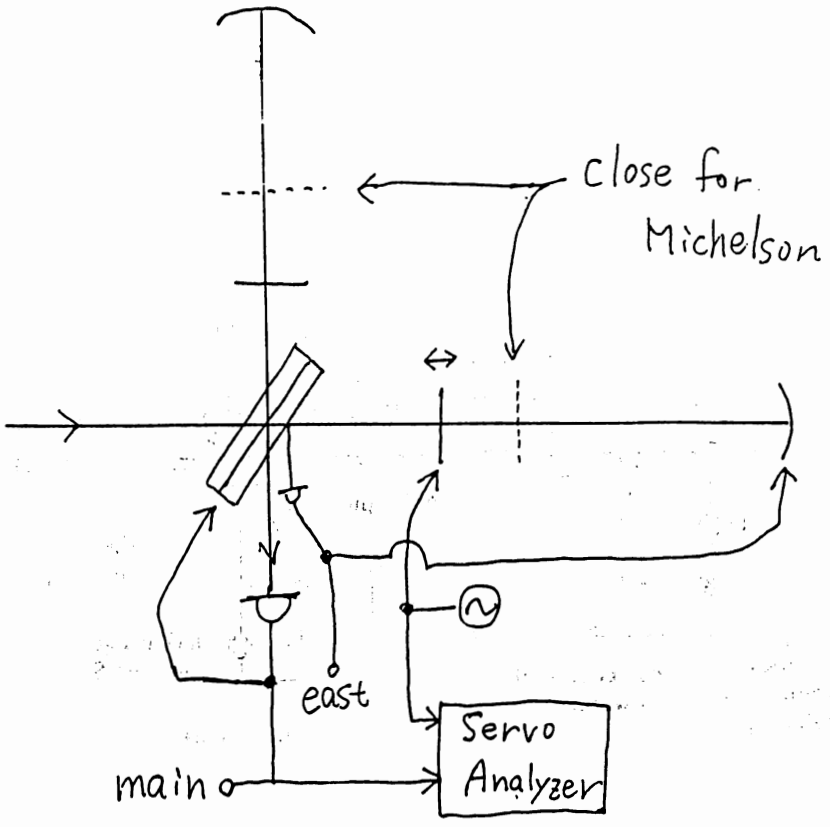

Fig.7.9 Calibration of 20m Fabry-Perot prototype.

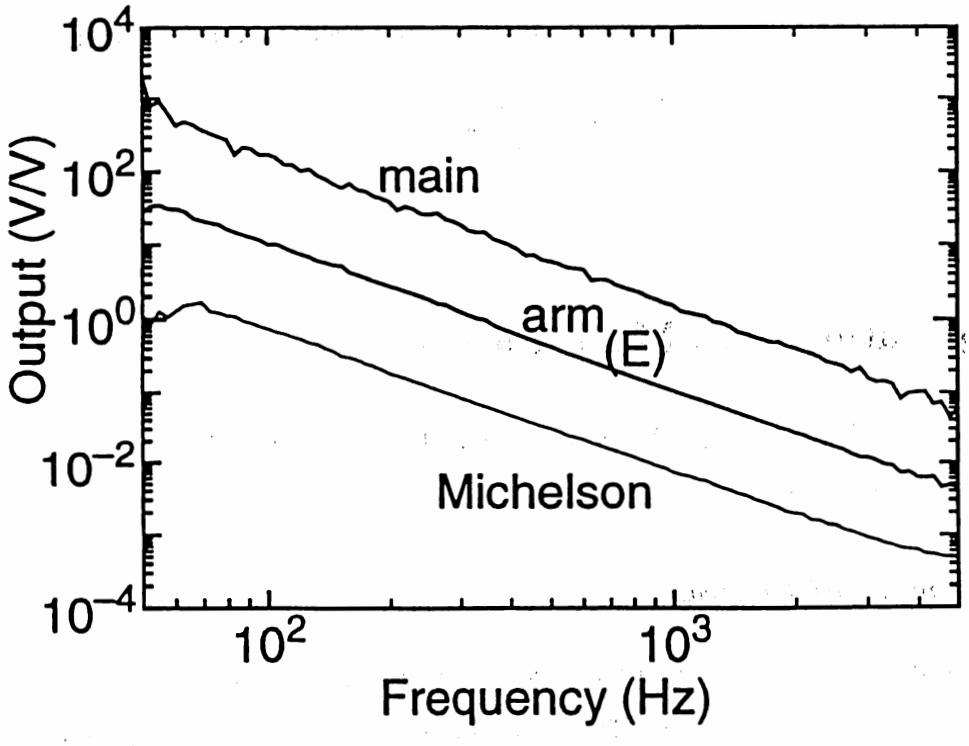

Fig.7.10 Calibration curve for 20m prototype.

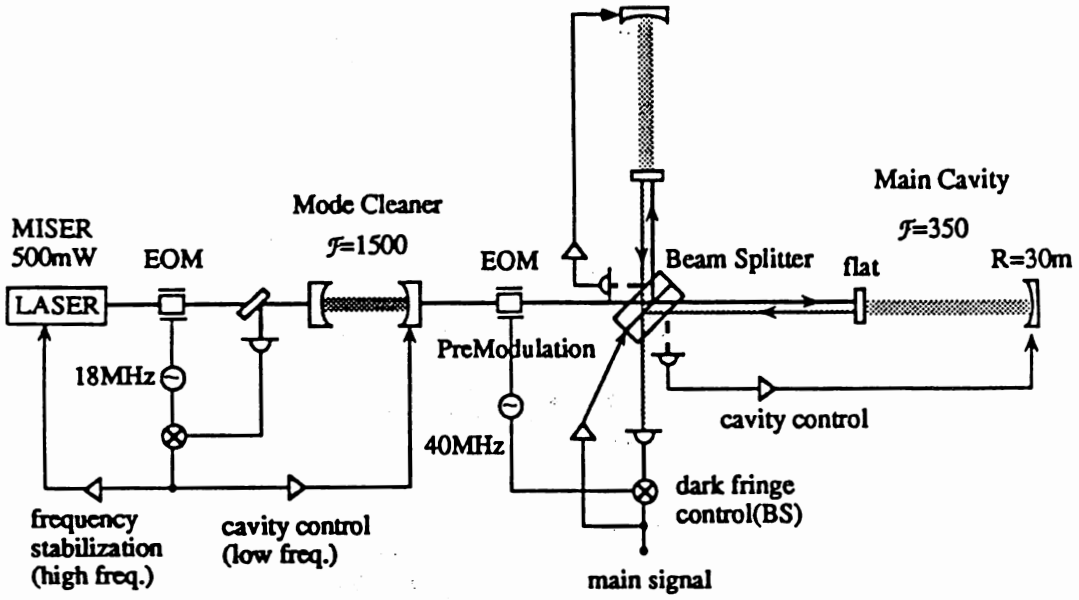

Fig.7.11 20m Fabry-Perot prototype with Mode Cleaner.

from the difference of detected power. We have the relation for west arm,

$$V_{\text{west}} = \frac{4}{11} V_{\text{east}} = 1.9 \times 10^8 \delta x \tag{7.2}$$

§7.2 Operation with Mode Cleaner

We operated 20m Fabry-Perot prototype detector with Mode Cleaner (Fig. 7.11) and improvement owing to Mode Clener was estimated.

· ***Improvement of Contrast***

One remarkable improvement was contrast of main interferometer recombining reflected light from each arm. Deformed beam containing spurious higer mode degrades contrast especially for an asymmetric interferometer, say in our case with

different arm lenghs, because phase shift of higher mode against optical path differs from that of fundamental mode. Without Mode Cleaner the contrast of the main interferometer with Fabry-Perot arms was up to 95%. With Mode Cleaner, in our experiment, the contrast improves up to 99.2%. Although these value cannot compare quantitatively considering detail change of setup in both case, it can be said that interferometer with 0.2m different arm lengths can attain such contrast, maybe more, with Mode Cleaner.

· ***Reduction of Frequency Noise***

Another improvement was reduction of frequency noise owing to frequency stabilization of Mode Cleaner. Figure 7.12 is the obtained noise spectra of main recombined signal as well as each arm. Spectrum of each arm has the same shape as the one obtained in the one-arm estimation in Section 6.2 (Fig.6.18); it consists of residual frequency noise over almost frequency range and unidentified noise, probably phase noise of the steering mirror and seismic noise, near 1kHz. Such common mode noise as residual frequency noise and phase noise will be reduced by recombining light from each arm.

Main spectrum in Fig.7.12 cirtainly shows CMRR of up to 20dB above ~50Hz except for 200–600Hz. Therefore excess noise in Fig.6.18 can be divided into common mode noise and others. One such un-common noise for 200–600Hz can be regarded as vibration due to resonance of breadboard (Section 7.1.1) considering its resonant frequency. Noise floor of $1.0\times10^{-16}\mathrm{m}/\sqrt{\mathrm{Hz}}$ at 2kHz is possibly limited by such un-common noise judging from the following measurement of CMRR.

· ***Estimation of CMRR***

In order to estimate CMRR, noise spectrum without frequency stabilization using Cavity Lock Servo of Mode Cleaner was obtained (Fig.7.13). Although the shown spectra indicate CMRR of about 20dB which is consistent with the data obtained without Mode Cleaner, the ratio is sensitive to the alignment of each arm. We found that the good alignment to maximize CMRR does *not* necessarily

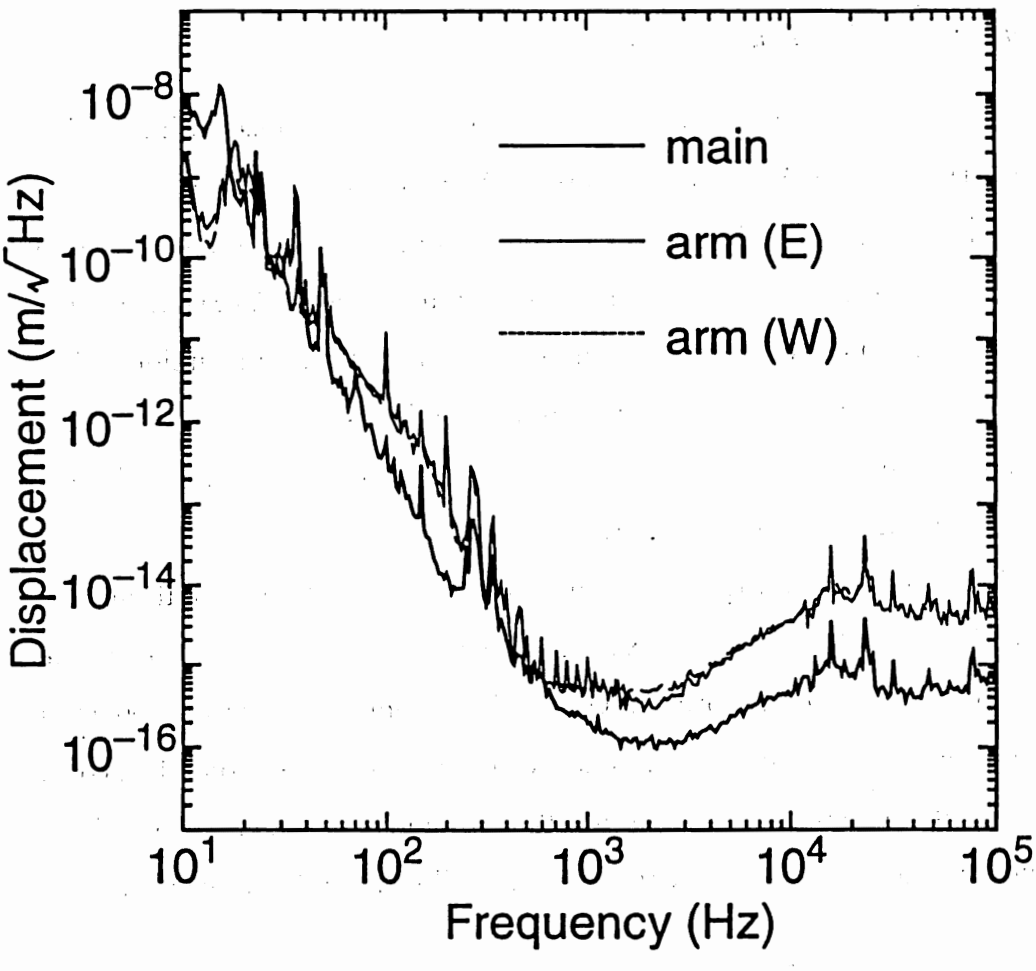

Fig.7.12 Output spectra of 20m Fabry-Perot prototype.

means the good aligment for contrast.

The contrast depends on the power reflected from each arm; if equal power is recombined at beamsplitter, the interfered light is cancelled out, resulting in high contrast. On the other hand, phase change due to frequency noise from each arm depends on

$$\begin{aligned} \delta\phi &= \frac{2\mathcal{F}}{\pi} k \frac{\ell}{\nu} \delta\nu \\ &= \frac{4}{c} \mathcal{F} \ell \delta\nu \quad \propto \mathcal{F}\ell, \end{aligned} \tag{7.3}$$

which has little to do with the reflected power. Considering the difference of each arm length

$$\begin{aligned} \frac{\Delta\ell}{\ell} &\sim \frac{2.5\text{cm}}{20\text{m}} \\ &\sim 10^{-3}, \end{aligned} \tag{7.4}$$

the discrepancy mainly comes from the difference of finesse of each arm

$$\begin{aligned} \frac{\Delta\mathcal{F}}{\mathcal{F}} &\sim \frac{370 - 350}{370} \\ &\sim 5 \times 10^{-2} \end{aligned} \tag{7.5}$$

If the optical performance of each arm cavity can be matched better than now using high quality mirrors, larger CMRR, more than 40dB, will be expected.

· ***Noise Source at Low Frequencies***

As Fig.7.12 and Fig.7.13 are sensitivity converted into vibration amplitude of cavity mirror using servo gain of each arm, they does not reflect seismic noise of beamsplitter. In both figures, noise level is enhanced at low frequencies when recombined; this is probably due to the vibration noise of beamsplitter. In order to estimate the vibration of beamsplitter, we compare the main spectrum converted into vibration amplitude of beamsplitter with that of Michelson interferometer which is formed with each front mirrors.

Figure 7.14 indicates that the major noise source of the main signal below 200Hz originates not from Fabry-Perot cavity but from the main Michelson interferometer. Although there still exists the possibility of noise due to different arm lengths of the Michelson interferometer, it is possibly due to vibration of

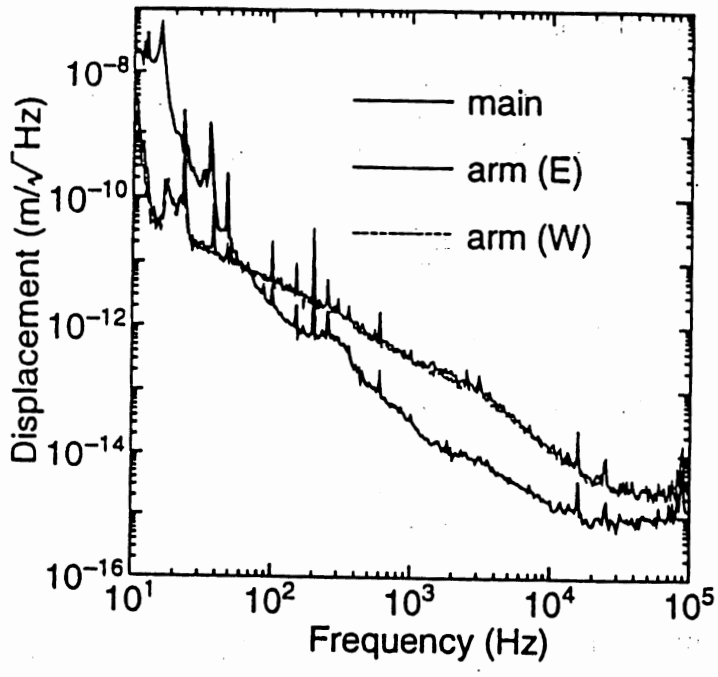

Fig.7.13 Estimation of CMRR without frequecy stabilization.

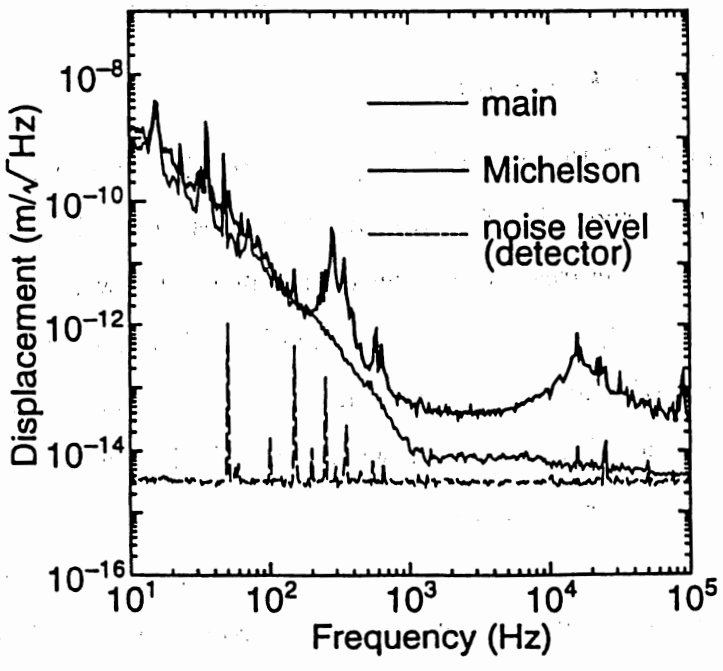

Fig.7.14 Estimation of noise from the main Michelson interferometer.

beamsplitter considering poor vibration isolation of beamsplitter. By applying the suspension used for arm mirrors with vertical vibration isolation to the beamsplitter, low frequency performance will be improved.

§7.3 Long Term Operation of the System

Finally we estimated long-term stability of the system. Status of 20m Fabry-Perot prototype as well as that of Mode Cleaner was remotely monitored; laboratory was unmanned during operation (25 hours). We confirmed continuous operation more than 3 hours. Major factors to fail the system were external vibration (e.g. sound) applied to Mode Cleaner and drift of alignment of Mode Cleaner. These factor will be removed in a degree by replacing current base table of the Mode Cleaner with such robust one as used in 20m prototype.

8. Conclusion

§8.1 Summary

We have developed Mode Cleaner with independently suspended Fabry-Perot cavity (ℓ=1m), and succeeded in operating 20m Fabry-Perot prototype detector with Mode Cleaner, which works as frequency stabilization system as well as mode selector. No significant problem has been observed, and noise source limiting sensitivity has been identified to some extent. In this section, results of this experiment are summarized and resolution of current problems to attain expected sensitivity is described.

8.1.1 Results

· ***Mode Cleaner as a mode selector***

- Measurement of beam jitter using 20m arm indicated that Mode Cleaner reduces beam jitter originating from fluctuation of air below 100Hz. The reduced jitter is limited by vibration of the cavity mirrors.
- Contrast of 20m Fabry-Perot prototype was improved more than 99% with Mode Cleaner; it can be interpreted as reduction of higher mode contribution.

· ***Mode Cleaner as a frequency stabilization system***

- Frequency stabilization with servo gain of 80dB near 1kHz was realized referred to suspended Fabry-Perot cavity. Estimation of frequency stability using 20m Fabry-Perot shows 60dB reduction of frequency noise. Discrepancy of 20dB seems vibrational origin.

· ***Performance of 20m Fabry-Perot prototype***

- Sensitivity of prototype was remarkably improved by frequency stabilization (Fig.8.1). Major noise source limiting sensitivity is vibration of beamsplitter below 100Hz, and also other vibration noise, such as vibration of steering mirror, seems to decide sensitivity above 100Hz.
- Common mode rejection ratio of main signal is up to 20dB in spite of high contrast (~99%). It can be interpreted as difference of finesse between each arm cavity.

8.1.2 Improvement of current system

· ***Improvement of Mode Cleaner as a mode selector***

As for Mode Cleaner as a mode selector, we found no problem except for beam jitter at low frequencies due to vibration of the cavity. Since such jitter is out of the observation band, it will not affect the sensitivity of the prototype. However, for the future large-scale detector, too much jitter at low frequencies may degrade dark fringe locking or common mode rejection (Section 8.2.1).

· ***Improvement of Mode Cleaner as a frequency stabilization system***

Figure 6.18 and 7.12 indicates that excess noise in Fig.6.18 contains both common mode noise (200~500Hz) and differential noise (500~2.5kHz). Common mode noise originates from steering mirrors fixed on the breadboard and/or vibration of Mode Cleaner cavity. Suspension of steering mirrors and further vibration isolation of Mode Cleaner cavity will reduce such common mode noise. As for the differential noise, one possibility is vibration of main mirrors excited by resonance of breadboard. This can be also reduced by isolating the mirrors.

· ***Improvement of 20m Fabry-Perot prototype***

As mentioned above, noise due to vibration frequency of 200~2kHz will be reduced by further vibration isolation. Another vibration noise of prototype was

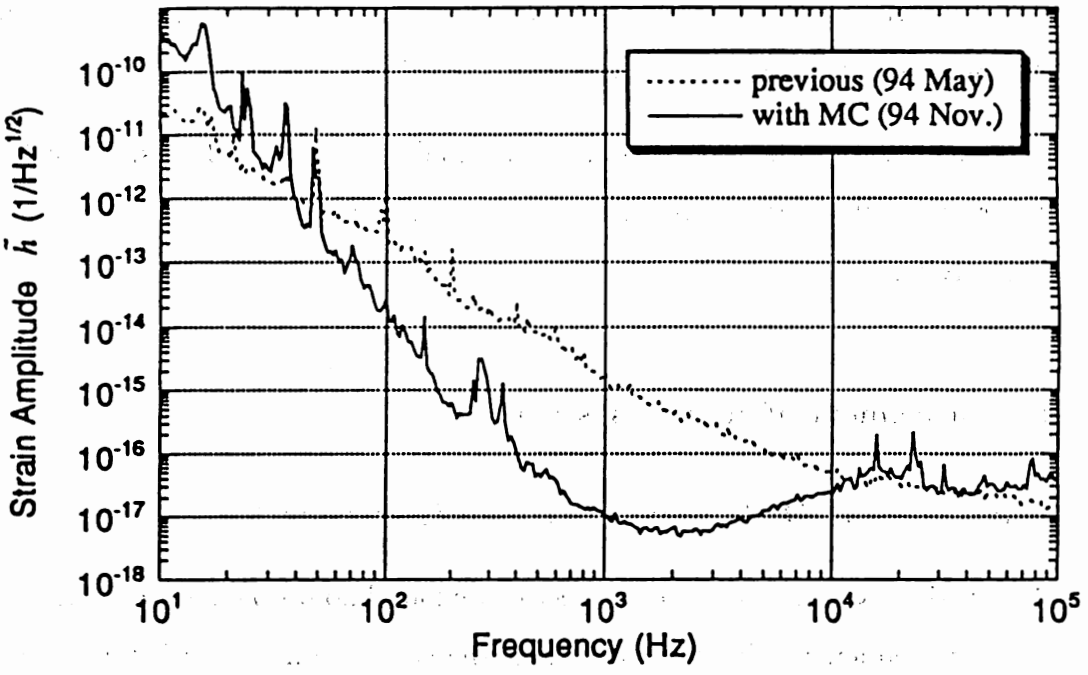

Fig.8.1 Improved sensitivity compared with previous experiment without Mode Cleaner.

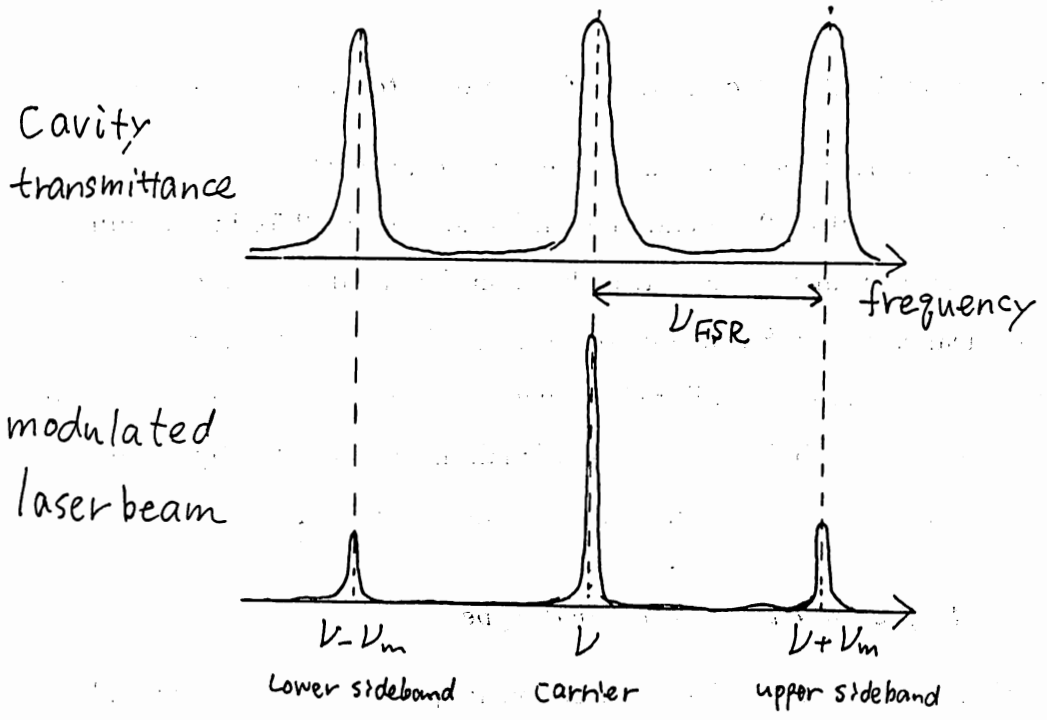

Fig.8.2 Modulation sideband and FSR of the cavity.

vibration of beam splitter below 100Hz. By applying vertical vibration isolation to beamsplitter, noise floor of Fig.7.12 and 7.14 will be reduced. For the future vibration isolation, see the following Section 8.2.2.

Another lack of common mode rejection ratio will be improved by applying high quality mirrors which can form the Fabry-Perot cavities with almost same finesse of each arm. If finesse of each cavity matches 1% precision, CMRR of 40dB can be expected (Equation (7.4)). Since it is really possible for small mirror cavities [30], it will be realized by large mirror cavity used for prototype or full scale detector.

Roughly speaking, we can attain the expected level in Fig.6.18 by applying further vibration isolation, which means one order noise reduction of Fig.7.12 ($\sim 10^{-17}\mathrm{m}/\sqrt{\mathrm{Hz}}$). Moreover by applying high quality mirrors for prototype, which realizes 40dB CMRR, further noise reduction of 20dB ($\sim 10^{-18}\mathrm{m}/\sqrt{\mathrm{Hz}}$) is expected, resulting in shot noise sensitivity.

§8.2 Possible Future Configuration

As an extent of this experiment, possible configuration for full scale gravitational wave detector as well as future Mode Cleaner for such detector is considered.

8.2.1 Future Mode Cleaner System and Interferometric Detector

Although improvement of current system mentioned above would be sufficient for the current prototype detector, more improvement including optical design and servo system will be necessary for the full-scale gravitational wave detector. In this subsection, possible design of Mode Cleaner for the future detector is discussed.

· ***Removal of Phase Modulator***

Ideally no optical components should be inserted between Mode Cleaner and main interferometer (in our case one EOM, a pair of isolator, lens and steering

mirrors are inserted), because they may distort the mode-cleaned beam. Although our result of 99% visibility shows it does not significant problem, at least EOM can be removed by the following configuration.

If we choose the modulation frequency as integer times of free spectral range of Mode Cleaner cavity,

$$\omega_m = N\frac{2\pi c}{2\ell} \tag{8.1}$$

where N is an integer, the modulated beam before Mode Cleaner can transmit cavity without any effect (in our case, at least ℓ=3.75m for 40MHz modulation). That is because any sideband of phase modulation is resonant when equation is satisfied (Fig.8.2). In this way, we can simply move EOM before Mode Cleaner cavity without significant configuration change.

· ***Wideband Phase Modulator for Frequency Control***

For the future detector, further frequency stabilization is needed. As we want to attain sensitivity of $h \sim 10^{-21}$, which corresponds to $3 \times 10^{-23}/\sqrt{\text{Hz}}$. In expectation of 40dB CMRR, frequency stability of $\delta\nu \sim 10^{-6}\text{Hz}/\sqrt{\text{Hz}}$ at 1kHz should be attained. This means the servo gain of 140dB is needed.

In our current design, unity gain frequency of the frequency stabilization servo is limited by resonance of PZT of MISER. Since more gain of 60dB from current gain (80dB) with keeping current unity gain frequency seems very difficult, fast frequency control system should be installed for the future frequency stabilization system. One possibility is wideband EOM modulator. Although modulation index of EOM is small compared with PZT and frequency control by phase modulator is ineffective at low frequencies, properly designed servo loop would realize three loop frequency stabilization with unity gain frequency of ~1MHz.

· ***Servo Design***

In order to obtain sufficient frequency stabilization gain at low frequencies, servo should be designed with lower cross over frequency between pendulum lock loop and frequency stabilization loop. But it means frequency instability due to

pendulum vibration will be enhanced. We can avoid this situation to some degree by the following vibration reduction of the Mode Cleaner cavity.

· ***Vibration reduction at Low Frequencies***

In Section 6.1, we found the beam jitter limited by vibration of the cavity below ~100Hz. Main signal of 20m prototype is also dominated by vibration of beamsplitter. For the full scale detector, cavity length of Mode Cleaner will be elongated about 100m. Although vibration, in this case, will be relaxed both for jitter and for sensitivity of gravitational waves, it will be very hard for further vibration isolation at low frequency, especially below 10Hz.

Promising solution for it seems construction of full-scale system underground. In the underground, seismic noise is one or two orders lower than the ground level (Fig.8.3) [31].

· ***Vibration Isolation at High Frequencies***

Sensitivity of detector seems to be limited by the vibration at several hundred Hz. Figure 8.3 shows that in the even underground site seismic noise is the same level as ground above ~100Hz, because in this frequency range major noise source is an artistic one, e.g. sound noise. Vibration isolation in these frequencies is relatively easy by using stack or multi-stage pendulum.

· ***Loose Lock Servo Scheme***

In our current design, all the pendulum masses are loosely locked, and signals are read out from the error signal. The advantage of such design is independence for the excess noise applied to the mass from feedback signal. Such noise includes electronic noise and seismic noise from actuator. Our prototype detector, however, has limited unity gain frequency, about 300Hz, due to loose lock scheme, because large seismic noise unlocks the servo with more loose one.

Two order reduction of seismic noise in the underground site will permit more loose lock scheme. Even our current servo design gives unity gain frequency of

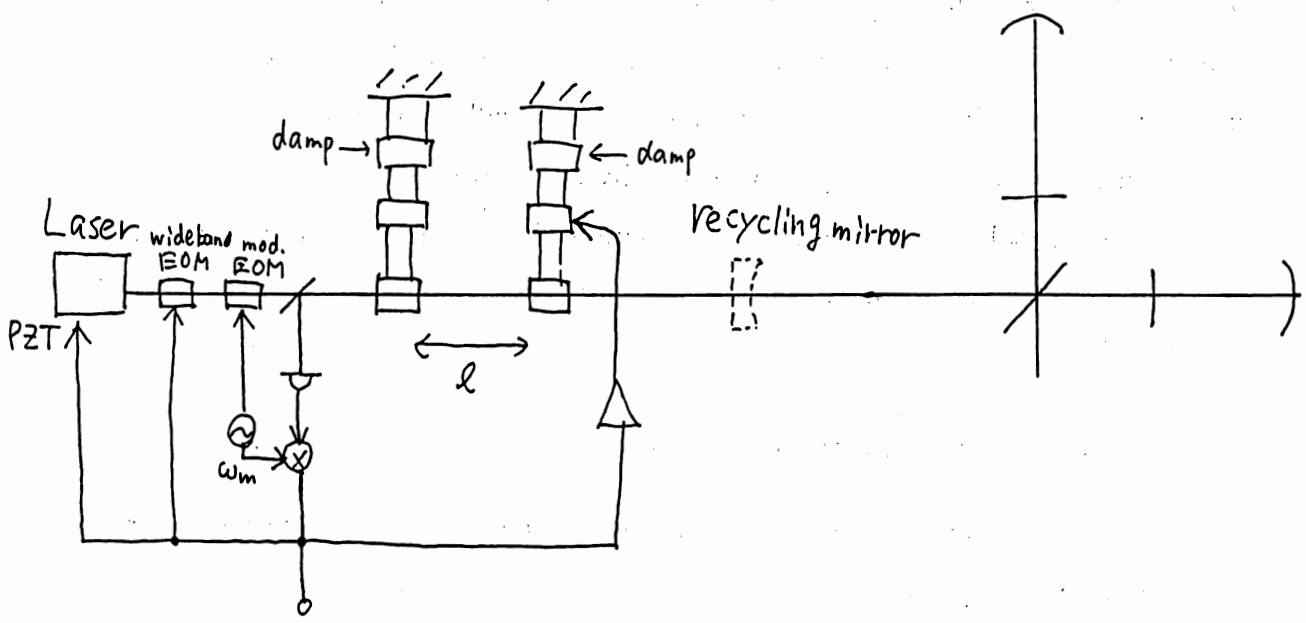

$$\omega_m = N \frac{\pi c}{\ell}$$

Fig.8.4 Design of possible future detector.

above 40Hz, considering Fig.7.8. For such low unity gain frequency, servo control may be realized by applying force only upper mass without any force applied to the final mass [32].

8.2.2 Full Scale Detector

Finally, considering the discussion mentioned above, full scale detector is designed as an extension of our experiment.

Figure 8.4 shows the full-scale detector with Mode Cleaner. Fundamental design is similar to current system. The detector is constructed underground where seismic noise level below ~100Hz is two order lower than the ground level, like Fig.8.3. Owing to the lower seismic noise level, all the mirrors are suspended as three-stage pendulums with feedback force applied only second (middle) mass. Final mass is not applied any force and is not attached any magnets, which avoids both excess noise from actuator and internal thermal noise due to degradation of mechanical Q of the mass. Damping force is applied the first (top) mass using eddy current; effect of ground vibration applied by the damping magnet is isolated by next two stage suspension.

In order to attain sensitivity of $h \sim 10^{-21}$, effective laser power of ~2kW is needed. By applying recycling scheme, original laser power can be down to ~100W if recycling gain of ~20 is attained. The incident laser is stabilized in frequency referred to Mode Cleaner cavity using both PZT and EOM. If we attain stabilization level of $\sim 1\mu\mathrm{Hz}/\sqrt{\mathrm{Hz}}$ and CMRR of main interferometer 40dB, designed sensitivity can be realized.

References

[1] J. H. Taylor and J. M. Weisberg, Astrophys. J. **345**, 434 (1989).

[2] B. F. Schutz, Nature **323**, 310 (1986).

[3] J. Weber, Phys. Rev. Lett. **22**, 1320 (1969).

[4] W. Johnson and S. Merkowitz, Phys. Rev. Lett. **70**, 2367 (1993).

[5] K. Danzmann *et al.*, *Proposal for a Laser-Interferometric Gravitational Wave Detector in Space.*

[6] M. Ohashi, M. -K. Fujimoto, T. Yamazaki, M. Fukushima, A. Araya, and S. Telada, in *Proc. of Seventh Marcel Grossmann Meeting on General Relativity, Stanford, U.S.A.*, July 1994.

[7] R. W. P. Drever, *Gravitation Radiation*, ed. N. Deruelle and T. Piran, (North-Holland, Amsterdam, 1983).

[8] C. N. Man, D. Shoemaker, M. Pham Tu, and D. Dewey, Phys. Lett. A **148**,8 (1990).

[9] L. Schnupp, talk at 'European Collaboration Meeting on Interferometric Detection of Gravitational Waves' (Sorrento, 1988).

[10] A. Giazotto, Phys. Rep. **182**, 365 (1989).

[11] P. R. Saulson, Phys. Rev. D **42**, 2437 (1990).

[12] R. Del Fabbro *et al.*, Rev. Sci. Instrum. **59**, 292 (1988).

[13] N. Mio, private communication.

[14] A. Rudiger, R. Schilling, L. Schnupp, W. Winkler, H. Billing, and K. Maischberger, Optica Acta 28, 641 (1981).

[15] A. Yariv, *Introduction to Optical Electronics*, 3rd edition (Holt, Rinehart, and Winston, Inc., 1985).

[16] D. A. Anderson, Appl. Opt. **23**, 2944 (1984).

[17] R. W. P. Drever, J. L. Hall, F. V. Kowalski, J. Hough, G. M. Ford, A. J. Munleyand, and H. Ward, Appl. Phys. **B31**, 97 (1983).

[18] T. J. Kane, A. C. Nilsson, and R. L. Byer, Opt. Lett. **12**, 175 (1987).

[19] D. Shoemaker, A. Brillet, C. N. Man, O. Cregut, and G. Kerr, Opt. Lett. **14**, 609 (1989).

[20] D. Shoemaker, R. Schilling, L. Schnupp, W. Winkler, K. Maischberger, and A. Rudiger, Phys. Rev. D **38**, 423 (1988).

[21] M. Stephens, P. Saulson, and J. Kovalik, Rev. Sci. Instrum. **62**, 924 (1991).

[22] K. Tsubono, A. Araya, K. Kawabe, S. Moriwaki, and N. Mio, Rev. Sci. Instrum. **64**, 2237 (1993).

[23] K. Nakagawa *et al.*, Optics Communication, in press.

[24] S. Kawamura, ISAS Report No.637 (1989).

[25] N. Uehara and K. Ueda, Opt. Lett. **19**, 728 (1994).

[26] M. Ohashi, doctor thesis (1994).

[27] M. Ohashi and M.-K. Fujimoto, in *Proc. of Sixth Marcel Grossmann Meeting on General Relativity, Kyoto, Japan*, 1511 (World Scientific 1992).

[28] M.-K. Fujimoto *et al.*, *Proc. of Elizabeth & Frederick White Res. Conf.*, Canberra, 1990.

[29] M.-K. Fujimoto, in *Proc. of Sixth Marcel Grossmann Meeting on General Relativity, Kyoto, Japan*, 1182 (World Scientific 1992).

[30] K. Kawabe, private communication.

[31] A. Araya, K. Kawabe, T. Sato, N. Mio, and K. Tsubono, Rev. Sci. Instrum. **64**, 1337 (1993).

[32] S. Telada, private communication.